DURBAN UNIVERSITY OF TECHNOLOGY
INYUVESI YASETHEKWINI YEZOBUCHWEPHESHE

DEVELOPMENT OF ELECTROCHEMICAL IMMUNOSENSORS FOR DETECTION OF INSULIN ANTIBODIES USING INDOLE-PYRAZOLE NANOPARTICLES

By

Senzekile Majola
(Student. No: 21512348)

Submitted in fulfillment of the requirements for the degree of Doctor of Philosophy in Chemistry, Faculty of Applied Sciences, Durban University of Technology

March 2025

DECLARATION

I, **Senzekile Majola**, declare that the thesis submitted for a Doctor of Philosophy in Chemistry at the Faculty of Applied Science at the Durban University of Technology is the outcome of my research, has not received substantive approval for any degree, and is not being concurrently submitted for any other degree. The author completed all the work, with the exception of incorporating it into jointly authored publications. Furthermore the author certifies that the work of others in the thesis have been appropriately acknowledged.

Student: Senzekile Majola

Signature: Date: **02 August 2025**

Supervisor: Dr M. Sabela

Signature: Date: **02 August 2025**

Co-Supervisor 1: Dr T.R. Makhanya

Signature: Date: **02 August 2025**

Co-Supervisor 2: Professor R.M. Gengan

Signature **02 August 2025**

DEDICATION

To my beloved **nieces** and **nephews**,

Life is filled with challenges, but through education, we can rise above them. No matter what obstacles you face, always remember that you are strong, capable, and never alone. Learning is not just about books it is about growth, resilience, and discovering the power within yourselves.

I hope this work serves as a reminder that knowledge is a tool for change, and with it, you can shape your own futures. Even in the hardest moments, you have the strength to move forward. I have walked a difficult path too, but education became my light it gave me purpose, strength, and hope.

Dream boldly, work hard, and embrace the strength that comes with learning.

You are deeply loved, and I will always be here for you, cheering you on every step of the way. Keep believing in yourselves, because I believe in you.

ACKNOWLEDGEMENTS

First and foremost, I give all glory and thanks to **God** for His unwavering guidance, strength, and grace throughout this journey. His presence has been my anchor, and without Him, none of this would have been possible.

To my **parents**, now resting in light, and to the ancestors of the **Cwele**, **Majola**, and **Makhaye** families. I carry you with me every step of the way. Your love, your wisdom, and your sacrifices are woven into the fabric of who I am. Even from beyond, you continue to shoulder me, to shield me, and to pave the path before me just as you always have. I honour you. You have held me through every silence and guided me through every storm. All that I am becoming is because of your presence, your prayers, and your protection. May you continue to walk with me, fight for me, and cover me still.

I extend my deepest gratitude to my **supervisor, Dr M. Sabela**, who has supported and mentored me since 2018. Your guidance, patience, and encouragement have been invaluable, and I truly appreciate the freedom you have given me to be myself in my research. To my **co-supervisors, Dr T.R Makhanya and Prof R.M Gengan**, thank you for your dedication, expertise, and unwavering support. Your contributions have played a crucial role in shaping this work.

I am also sincerely grateful to the **National Research Foundation (NRF)** for their financial support, which made this research possible. Your investment in education and research is deeply appreciated.

I extend my heartfelt thanks to **my family and friends** for their continuous love, belief, and encouragement. Your support has been my greatest source of strength, and I am forever grateful for your presence during both the challenging and joyous moments of this journey.

A special thank you to **Ma Mavis** and the **lab staff**, whose assistance in the laboratory has been instrumental in my research. Your kindness, patience, and willingness to help have not gone unnoticed.

I would like to dedicate a special acknowledgment to **Ma Mpume**. She was a light in my life and a listening ear when I needed it the most. Her support went beyond just the lab, she was there for me in my personal struggles and offered comfort and guidance. Although she is no longer with us, her memory and kindness will forever remain in my heart. May her soul rest in beautiful and eternal peace.

Finally, to everyone who has contributed to this journey in any way your support, encouragement, and guidance have meant the world to me.

ABSTRACT

Insulin antibodies have shown to be a strong predictor of diabetes development in genetically susceptible individuals and the development of type 1 diabetes is strongly associated to the presence of antibodies that attack beta cells (islet cells), such as insulin. The development of a sensitive, selective, efficient, and economical insulin detection system is crucial for the diagnosis and management of diabetes. The existing methods can produce results that are very specific, highly sensitive, and dependable. They include notable disadvantages, including high costs, extensive time requirements, the necessity for substantial sample preparation, and the emission of hazardous radiation. Electrochemical assays, characterised by their high sensitivity and selectivity, rapid reaction time, straightforward automation, dependable results, and relatively low cost, can address the drawbacks of conventional approaches. Furthermore, electrochemical sensors utilising biosensor technology provide the most efficacious approach for the detection of antibodies to antigens.

Electrochemical immunosensors have emerged as powerful tools for the rapid and sensitive detection of biomarkers. The detection of insulin antibodies is critical for the management of autoimmune responses in diabetic patients. This study aimed to develop and optimise an electrochemical immunosensors for the detection of insulin antibodies using indole-pyrazole capped cobalt or gold nanoparticles. Nanoparticles (cobalt or gold) capped with novel indole-pyrazole derivatives (bis indole-pyrazole or chromone indole-pyrazole) were synthesised

and immobilised onto the surface of a bare platinum electrode. Indole-pyrazole derivatives were selected due to their electron-rich, conjugated structures and potential to enhance charge transfer and sensor sensitivity. This modification enhanced the specific surface area and stability of the sensor platform. Insulin antigen was then introduced to promote antibody binding, followed by blocking with bovine serum albumin (BSA) to prevent non-specific binding and improve the accuracy, sensitivity, and reliability of the immunosensor. Each metal nanoparticle had two sensors: one capped with bis indole-pyrazole and the other with chromone-indole-pyrazole. All sensors demonstrated high detection ability for insulin antibodies, with a low detection limit, good selectivity, sufficient stability, and excellent recovery rates. This demonstrates the potential of the developed immunosensors for quantifying insulin antibodies. However, sensors incorporating the chromone-indole-pyrazole derivative outperformed those with the bis indole-pyrazole derivative, exhibiting lower limits of detection (LODs) and higher recovery rates for both metals.

The green synthesis of cobalt and gold nanoparticles (CoNPs and AuNPs) using lemon peel extract was successfully achieved, with indole-pyrazole derivatives (BIP and CIP) acting as additional capping agents. Phytochemical screening was conducted to identify the compounds in the lemon peel extract, such as phenols, flavonoids, tannins, and alkaloids, which played a role in nanoparticle stabilisation and reduction. Characterisation techniques such as UV-Vis, FTIR, SEM, and EDS confirmed the successful formation of CoNPs and AuNPs with well-defined morphological and elemental properties. The UV-Vis spectra displayed characteristic surface plasmon resonance peaks, indicating nanoparticle formation. SEM analysis showed that the nanoparticles were predominantly spherical, with some aggregation due to phytochemical interactions. EDS data further confirmed the elemental composition, demonstrating the presence of cobalt and gold within the nanoparticles

The fused indole-pyrazole derivatives viz bis indole-pyrazole **4a** (BIP) and chromone indole-pyrazole **4b** (CIP) were synthesised by reacting aldehyde derivatives, thiosemicarbizide and an indole through a one-pot synthesis via 2+3 annulation. Then, characterised using fourier transform infrared (FTIR), nuclear magnetic resonance (NMR), and time-of-flight mass spectrometry (TOF-MS). To better understand their properties since they are newly synthesised compounds, biological evaluations were performed. Initially, a mutagenicity test was performed, and the compounds showed no significant increase in revertant colonies against *S. typhimurium* TA 98 and TA 100 strains. In the MTT assay for cytotoxicity against two human cancer cell lines, A549 and HepG-2; and one normal, HEK 293. Compound **4b** showed high potency against the cancer cell lines, with IC_{50} values of 18.70 and 50.07 µg/mL, respectively. Whilst, both compounds showed low inhibition level against HEK 293 at 100 µg/mL. The in vitro inhibition of α-amylase and α-glucosidase, compound **4a** demonstrated excellent in vitro inhibition of α-amylase and α-glucosidase, with the IC_{50} values of 3.9 µg/mL and 12.1 µg/mL, respectively. Compound **4a** exhibited strong inhibitory activity against α-amylase and α-glucosidase, for the anticancer activity only compound **4b** showed promising results.

TABLE OF CONTENTS

LIST OF FIGURES

LIST OF TABLES

LIST OF SCHEMES

LIST OF ACRONYMS AND SYMBOLS

A549: Lung adenocarcinoma

ACV: Amperometry current voltammetry

AdsSV: Adsorptive stripping voltammetry

APT: Attached Proton Test

AuNPs: Gold Nanoparticles

BIP-AuNPs: Bis Indole-pyrazole gold nanoparticles

BIP-CoNPs: Bis indole-pyrazole cobalt nanoparticles

BSA: Bovine serum albumins

BSE: Back-Scattering Electrons

CIP-AuNPs: Chromone indole-pyrazole gold nanoparticles

CIP-CoNPs: Chromone- indole-pyrazole cobalt nanoparticles

CoNPs: Cobalt nanoparticles

$Co(NO_3)_2 \cdot 6H_2O$: Cobalt nitrate

COSY: Correlation Spectroscopy

CV: Cyclic Voltammetry

DMSO: Dimethyl sulfoxide

DPV: Differential pulse voltammetry

EDS: Energy Dispersive X-ray Spectroscopy

EI: Electron impact

EIS: Electrochemical impedance spectroscopy

ELISAs: Enzyme immunoassays

EOCV: Open-circuit voltage

FCR: Folin-Ciocalteu Reagent

FTIR: Fourier transform infrared spectroscopy

GAD: Glutamic acid decarboxylase

GCE: Glassy carbon electrode

GSH: L-glutathione

HbA1c: Hemoglobin A1c

HEK 293: Human embryonic kidney

Hep-G2: Hepatocellular carcinoma

$HAuCl_4.3H_2O$: Gold(III) chloride trihydrate

HMBC: Heteronuclear Multiple Bond Correlation

HSA: Human serum albumin

HSQC: Heteronuclear Single Quantum Coherence

K_2HPO_4: Dipotassium hydrogen phosphate

$K_3Fe(CN)_6$: Potassium hexacyanoferrate

KH_2PO_4: Potassium dihydrogen

LOD: Limit of detection

MCRs: Multicomponent reactions

MS: Mass spectrometry

MTT: 3-(4,5-dimethylthiazol-2-yl)-2,5-diphenyltetrazolium bromide

NMR: Nuclear magnetic resonance

OECT: Organic electrochemical transistor

OPSS: One-pot stepwise synthesis

PBS: Phosphate-buffered saline ....

PtE: Platinum electrode...

QE: Quercetin...

RIAs: Radioimmunoassay ....

SEM: Scanning electron microscope..

SPR: Surface Plasmon Resonance...

SWV: Square wave voltammetry...

TEM: transmission electron microscopy ....

TLC: Thin layer chromatography ....

TOF-MS: Time-of-flight mass spectrometry..

UV: Ultraviolet ....

UV-Vis: Ultraviolet Visible Spectrometry ....

LIST OF PUBLICATIONS AND CONFERENCES

PUBLICATIONS

Research articles

- Majola, S., Sabela, M., Gengan, R. and Makhanya, T., 2024. A Facile One-Pot Synthesis of New Fused Indole Pyrazole Derivatives and Their Anticancer and Antidiabetic Activities. ChemistrySelect, 9(48), p.e202404759. https://doi.org/10.1002/slct.202404759 .
- Majola, S., Gengan, R.M., Makhanya T.R and Sabela, M. Chromone Indole-pyrazole Cobalt Nanoparticle Electrochemical Immunosensor for the Detection Insulin antibodies. Journal of ChemNanoMat. **Submitted**

Book chapters

- Majola, S. and Sabela, M., 2024. Bionanomaterials in Electrochemical Biosensing Applications. In Bionanomaterials for Industrial Applications (pp. 289-300). CRC Press. https://doi.org/10.1201/9781003432791.
- Majola, S., Ndaba T and Makhanya T.R. Fused Indole-Pyrazole: An Emerging Moiety in Combinatorial Chemistry with Promising Medicinal Properties. In Heterocycles - Exploring the Realm of Ring Structures and Biological Potentials. IntechOpen. ISBN 978-1-83635-196-2. **Accepted.**

CONFERENCES

- S. Majola, R.M Gengan T.R Makhanya and M Sabela. Electrochemical Immunosensor for Insulin Antibody Detection Using Green Synthesized Gold Nanoparticles Functionalized with Indole-Pyrazole. At 7th International Symposium on Electrochemistry, at Southern Sun Maharani Hotel in Durban, KwaZulu-Natal, from 13 -16 April 2025. 3 minutes Flash Talk Poster Presentation.
- S. Majola, M. Sabela, R.M Gengan and T.R Makhanya. “Design and Synthesis of Indole-Pyrazole Derivative with Potential Anticancer and Antidiabetic activity” World Congress on organic chemistry and international conference on optical and laser technology, at Millennium Hotel Paris Charles De Gaulle, Zone Hoteliere 2 Allee Du Verger Roissy En France, 95700 Paris, France, October 24-25, 2024. Poster Presentation
- S. Majola, M. Sabela, R.M Gengan and T.R Makhanya. “Design and Synthesis of Chromone Indole-Pyrazole Derivative with Potential Anticancer and Antidiabetic activity” Research, Innovation and Entrepreneurship Day, Durban ICC, 29 October 2024. Poster Presentation
- S. Majola, M. Sabela, R.M Gengan and T.R Makhanya, “Synthesis and Characterization of novel Fused Indole pyrazole as capping agent “SACI-KZN 2022 PG Colloquium 2022 held in UKZN Pietermaritzburg, South Africa on the 28th of October 2022, Poster Presentation.

- S. Majola, M. Sabela, R.M Gengan and T.R Makhanya, “Synthesis and Characterisation of novel Fused Indole pyrazole as capping agent “faculty of Applied Sciences Research Day” held in Coastlands Musgrave Durban, South Africa on the 17 of November 2022, Poster Presentation.

1 CHAPTER 1: INTRODUCTION

This chapter gives a brief overview of insulin as a biomarker for diabetes and explains the importance of insulin antibodies as predictors of diabetes development. This chapter also highlights the significant role of electrochemical immunosensors in the detection of insulin antibodies. We also discussed the significance of nanomaterials in enhancing the sensitivity of electrochemical immunosensors and how indole pyrazole moieties can be combined with various substituted and unsubstituted aromatic compounds to generate novel molecules, thereby offering a vast realm for exploration. This chapter also serves as a guide, explaining the aims and objectives of the study and offering an overview of the overall framework of the thesis.

1.1 Insulin: Diabetes Biomarker

Diabetes is a chronic disease that occurs when the pancreas does not produce enough insulin or when the body does not utilise the insulin effectively. There are two types of diabetes, both associated with insulin. Type 1 diabetes is defined by a lack of insulin production, whereas Type 2 diabetes is characterised by incorrect insulin utilisation in the body and cell resistance; an increase in the level of circulating blood glucose stimulates the release of insulin into the blood. (Arya *et al.* 2021; Shepa *et al.* 2021). Insulin is the main hormone that regulates the glucose level in blood (Vasiljevic *et al.* 2020; Arya *et al.* 2021; Shepa *et al.* 2021) and ensures a normal glucose level in blood (Shepa *et al.* 2021; Farrokhnia *et* *al.* 2022). Insulin antibodies have shown to be a strong predictor of diabetes development in genetically susceptible individuals. As, the development of type 1 diabetes is strongly associated to the presence of antibodies that attack beta cells (islet cells), such as insulin (Farrokhnia *et al.* 2022). This research project focuses on insulin antibodies as biomarker for diabetes. Biomarkers offer a dynamic and powerful approach to understanding the disease spectrum, with applications in prognosis, epidemiology, screening diagnosis, and randomised clinical trials (Mojsoska *et al.* 2021; Rahmati *et al.* 2021). They make it possible to categorise diseases and risk factors uniformly, increase our understanding of the underlying pathophysiology of diseases, and map the entire disease spectrum from the first signs to the end stage.

Detecting insulin antibody levels is of great importance, as a results, approximately over two-thirds of individuals with type 1 diabetes have insulin antibodies (Farrokhnia *et al.* 2022; Wardani *et al.* 2023). Radioimmunoassay (RIAs) (Asadpour *et al.* 2021), enzyme immunoassays (ELISAs) (Vargas *et al.* 2023), and Surface Plasmon Resonance (SPR) (Drozd *et al.* 2024) are some of the methods used to detect diabetes antibodies. These methods offer reliable, specific, and sensitive results; however, they also come with notable limitations: they are time-consuming, labor-intensive, costly and difficult method. That requires a large sample volume and emits harmful radiation, making them unsuitable for regular marker testing (Farrokhnia *et al.* 2022). Due to these disadvantages, the development of a sensor to detect insulin would be of great benefit in improving the diagnosis of diabetes. Therefore, in this study, we present the development of an electrochemical immunosensor for the detection of insulin antibodies as a biomarker of diabetes.

1.2 Electrochemical biosensors

Electrochemical sensors are analytical devices that convert chemical information into an electrical signal. They typically consist of a reference electrode and a working electrode separated by an electrolyte. These sensors work by generating electrical signals proportional to the analyte concentration, often in the presence of a chemical or biological solution. Techniques used in electrochemical sensing include amperometry, potentiometry, and voltammetry, among others. Voltammetric approaches, in particular, are frequently used to detect biological entities due to their simplicity and selectivity (Asadpour *et al.* 2021). Electrochemical biosensors are essential in today's laboratory and clinical examination of various chemical and biological targets. The recent development of functional bionanomaterials opens new avenues for improving electrochemical biosensor performance. Hence, they have been proposed for the detection of several disease biomarkers (Wang *et al.* 2017; Cruz *et al.* 2020; Li *et al.* 2021).. These sensors offer several benefits that make them desirable diagnostic tools in medicinal applications.

They utilise low-cost electrodes that can be quickly and easily integrated with basic electronics for quantitative measurements in the environmental and health sector. When, the analyte is in a complex sample (Asadpour *et al.* 2021; Anusha *et al.* 2022; Chupradit *et al.* 2022). Amperometry current voltammetry (ACV), open-circuit voltage (EOCV), adsorptive stripping voltammetry (AdsSV), square wave voltammetry (SWV), differential pulse voltammetry (DPV), cyclic voltammetry (CV), electrochemical impedance spectroscopy (EIS) and organic electrochemical transistor (OECT). Are among the diagnostic techniques used in electrochemical biosensing (Negahdary and Angnes 2022). Different types of biosensors are used to detect disease biomarkers, including enzyme-based biosensors, which are a good example of essential biosensors (Geetha Bai *et al.* 2021). Immunosensors based on antigen-antibody binding reactions and aptasensor based on a DNA or RNA aptamer are the biological recognition element (Mazloum-Ardakani, Barazesh and Moshtaghioun 2019; Rahmati *et al.* 2021).

1.2.1 Electrochemical Immunosensors

Electrochemical immunosensors have been proposed to detect various disease markers (Liu *et al.* 2021). They have inherent advantages such as fast detection time, unique sensitivity, cost-effectiveness, and excellent compatibility with miniaturisation technologies (Anusha *et al.* 2022). There are a few reports in the literature on immunosensors based on the detection and quantification of insulin antibodies through an antigen-antibody binding reaction. However, electrochemical immunosensors have been considered as new alternatives for identifying biomarkers (Jozghorbani *et al.* 2021). As an example Anusha et al 2022, developed an electrochemical immunosensor based on the GCN-b-CD/Au nanocomposite to monitor vitamin D deficiency (Anusha *et al.* 2022). Chen and co-workers detect prostate-specific antigens using an electrochemical immunosensor (Chen *et al.* 2021).

To assemble a high-performance electrochemical immunosensor, the reasonable design of an advanced nanomaterial for electrode modification is one of the critical factors (Chen *et al.* 2021; Wang, Liu and Hua 2021). Due to the absence of a crosslinking agent, the demand for nanomaterial-based amplification in electrochemical immunosensors is more rigorous. To efficiently enhance the analytical behaviour of the immunosensor. The employed nanomaterial needs to possess excellent electrical conductivity to accelerate electron transfer and enlarge the specific surface area to immobilise more biomolecules (Chen *et al.* 2021). Immobilising nanomaterials can significantly enhance the analytical properties of bare electrodes, including lower detection limits, increased sensitivity, and broader linear ranges (Shepa *et al.* 2021).

1.3 Bionanomaterials

Bionanomaterials are all nanomaterials created from biological molecules that can be employed for medicinal applications with minimal or no medical adverse effects, excluding medications (Jeevanandam *et al.* 2022; Shojaei, Soltani and Derakhshani 2022). Furthermore, they are an ideal substitute for typical nanomaterials in biomedical applications (Jeevanandam *et al.* 2022). Biomolecules (proteins, amino acids, enzymes, and metabolites) can be extracted from sources such as microbes (Khalil *et al.* 2022), plants (Sharma *et al.* 2022), agricultural waste (Zamani, Marjani and Mousavi 2019), or marine organisms (Jeong *et al.* 2022) and then coated, or immobilised with metallic ions (Jeevanandam *et al.* 2022). Figure 1.1 illustrates an experimental technique for employing plant extract to synthesise metallic nanomaterials. They have received great attention from researchers due to their unique applications in various fields such as antimicrobial activity (Zaib *et al.* 2020), electrochemical sensing (Šišoláková *et al.* 2020) and photocatalytic (Vinayagam *et al.* 2023). As a result, several research studies using microorganisms, protein, and plant extract-based green synthesis approaches have been published recently.

The plant extract-based green route is regarded as a valuable alternative due to its biocompatibility and cost-effectiveness. Plant extracts comprise several significant phytochemicals, including alkaloids, terpenoids, phenols, tannins, and flavonoids (Otitolaiye *et al.* 2023). Phytochemicals function as reducing and capping agents in the synthesis of metal nanoparticles from their precursors (Alzahrani and Alkhudidy 2021; Singh 2022). Thanks to the distinctive qualities of phytochemicals, nanomaterials could be successfully prepared through environmentally friendly synthesis methods using extracts from various parts of the plant. The focus on bionanomaterials to improve human health has been proven to be essential, and it continues to receive attention from researchers. In this project, we synthesised gold, and cobalt nanoparticles using lemon peel extract as a reducing agent and indole-pyrazoles compounds as capping agents for immobilisation onto a bare electrode to enhance the sensitivity.

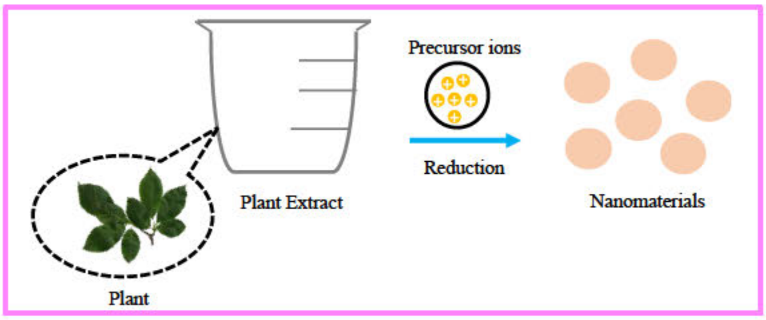

Figure 1.1: A schematic diagram describing green synthesis of nanomaterials using plant extract.

1.4 Lemons

Citrus represents a significant category of tree crops cultivated globally, with oranges, limes, and lemons recognised as prominent species (Sharma and Kukreja 2022). Citrus fruits have been utilised in traditional Asian medicine for decades. Recognised for their abundance of secondary metabolites that exhibit diverse biological activities (Verma, Gupta and Singh 2021). Lemons represent a widely cultivated and commercially significant variety of citrus fruit globally. This is a perennial yellow (Figure 1.2) subtropical plant belonging to the citrus genus within the *Rutaceae* family. It serves as a significant source of vitamin C and possesses uniquely aromatic peels. The peel extracts contain high levels of bioactive compounds and exhibit potential antioxidant properties. Lemon leaves and seeds have been utilised in various regions globally for the treatment of diseases including bronchitis, diarrhoea, and asthma (Abbasi *et al.* 2021) Commercially, 34 % of lemons produced yearly are consumed for juice production, leaving approximately 44 % peel as waste (Jahan and Isildak 2021). These lemon peels, which are generally discarded as waste, can be of good use. Lemon peels can give an eco-friendly and low-cost platform for synthesising novel nanoparticles.

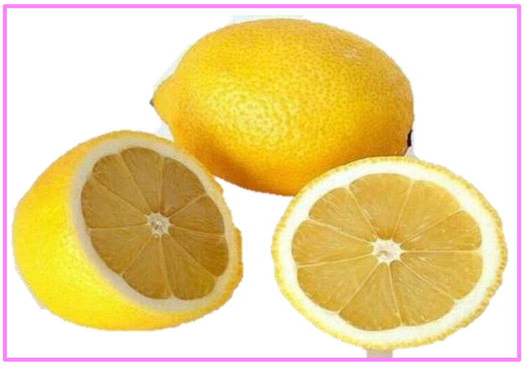

Figure 1.2: lemons fruit.

1.5 Pyrazoles and Indoles

Typical heterocyclic scaffolds, such as indole, pyrazole (Figure 1.3) and their derivatives, have demonstrated immense potential for use in the development of new pharmacological activities with distinct chemical structures and exceptional bioactivities (Fan *et al.* 2023; Mushtaq and Ahmed 2023; Nitulescu *et al.* 2023; Zaki *et al.* 2023; Zhang *et al.* 2023b). Indole scaffolds, found in many synthetic medicine molecules, can build effective targets and bind to many receptors. With high affinity, enabling the synthesis of new biologically active chemicals (Mushtaq and Ahmed 2023; Song *et al.* 2023) and its ability to mimic protein structures. Makes it a valuable tool for developing new therapeutic medicines (Nigam *et al.* 2024). On the other hand pyrazoles are also known to be pharmacophores in various molecular entities and dominate the pharmaceutical industry due to high yield and purity obtained from the basic substrate (Dadiboyena and Nefzi 2011). They are a suitable scaffold for designing and developing diverse pyrazole compounds with enhanced biological potency. They have the potential to bind with enzymes and proteins (Makhanya, Gengan and Kasumbwe 2020). The pyrazole scaffold can be combined with various substituted and unsubstituted aromatic compounds to generate novel molecules, offering a vast realm for exploration in synthesis research.

However, indole-pyrazole hybrids are interesting because they have the potential to produce synergistic effects compared to molecules with only one of the separate pharmacophores (pyrazole or indole). These hybrids are an attractive field of study for future medicinal chemistry applications since numerous types of indole-pyrazole hybrids exhibit a variety of potential biological functions (Hawash *et al.* 2023; Man *et al.* 2023). In this study, we designed and synthesised two indole-pyrazole derivatives using a one-pot synthesis via a 3+2 annulation reaction. Their potential as capping agents for nanoparticle synthesis is evaluated, with the objective of improving the sensitivity of electrochemical immunosensors for the detection of insulin antibodies. The fused indole-pyrazole scaffold exhibits several key chemical properties that make it highly valuable not only in medicinal chemistry but also in electrochemical sensor applications. Its aromaticity, arising from the conjugated π-electron systems of both the indole and pyrazole rings, can enhance charge delocalisation and improve electron transfer at the sensor interface (Moscoso *et al.* 2023).

These same π-systems also support strong π-π stacking and non-covalent interactions with biomolecules such as proteins particularly important in immunosensing, where antibodies (being proteins) must be captured and recognised efficiently at the electrode surface (Moscoso *et al.* 2023). The nitrogen atoms present in both rings provide lone pairs that coordinate well with metal nanoparticles, supporting stable capping and surface functionalisation (Serpell, Cookson and Beer 2020). In addition, the scaffold's hydrogen bonding capabilities with the indole NH acting as a donor and pyrazole nitrogens as acceptors can further support specific binding interactions, potentially improving antibody capture, sensitivity, and overall sensor response (Fabitha *et al.* 2022). These features support the use of indole-pyrazole ligands not only for biological activity but also as functional components in electrochemical immunosensor design. The fusion of indole and pyrazole units is hypothesised to enhance the electronic properties of the resulting compound, thereby potentially improving sensor performance through more efficient electron transfer.

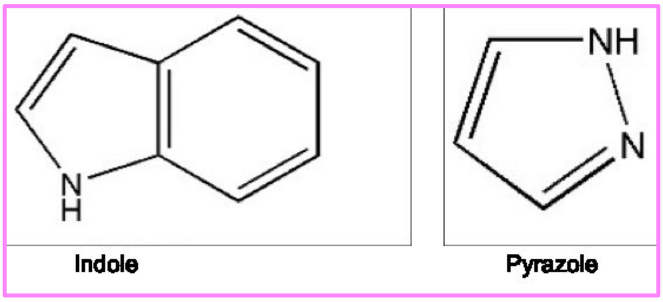

Indole **Pyrazole**

Figure 1.3: Heterocyclic structures of Indole and pyrazole.

1.5.1 One pot synthesis

A one-pot synthesis method is a unique technique that allows α, β-unsaturated aldehydes and acetophenones to react directly with hydrazines (Farooq and Ngaini 2020). It integrate simple precursors into formation of a complex molecules in a single step (Qi et al. 2021). The benefits of one pot synthesis, it includes reduced purification times compared to conventional multistep synthesis. As well as bond-formation efficiency, atom economy, product diversity, and complexity (Wang *et al.* 2021b; Wang *et al.* 2021c). This approach has also reduced waste output by decreasing the number of purification stages, due to the creation of new bonds in a single-pot system. Thus, the desired product includes all the substrates utilised as starting materials. They have revolutionised heterocyclic synthesis and provided an efficient technique in combinatorial chemistry. Playing as a significant tool into accessing novel bioactive molecules. The one-pot synthesis can be conducted in three distinct methods: one-pot stepwise synthesis (OPSS) and cascade reactions, multicomponent reactions (MCRs) (Ma and Zhang 2022) and in this study MCRs is employed. Figure 1.4 shows a systematic representation of all three methods.

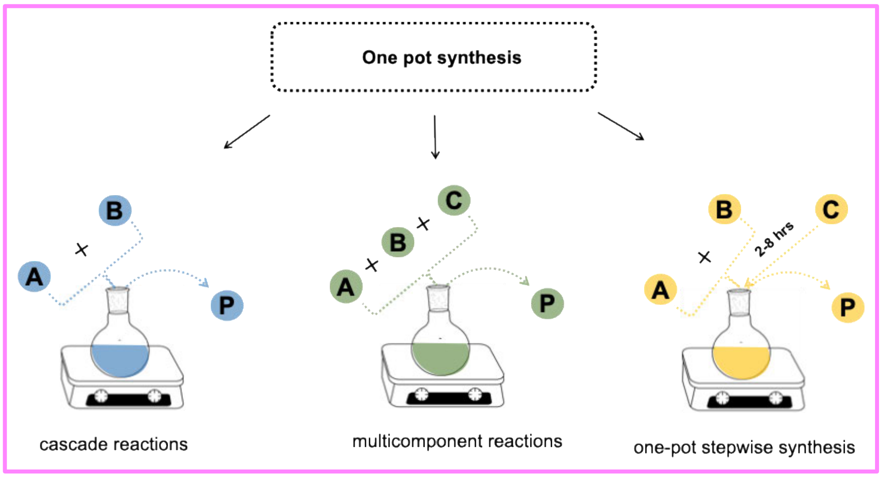

Figure 1.4: Conceptual representation of the three one-pot reactions.

1.5.2 3+2 annulation reaction.

A 3+2 annulation reaction, also called a [3+2] cycloaddition, is a chemical reaction that produces five-membered rings. It includes a three-atom component (1,3-dipole): Examples of a 1,3-dipole are nitrile oxides and nitrone, which have extra electrons to share. And a two-atom component (dipolarophile), which is typically a double bond (alkene) or triple bond (alkyne) that can accept an extra electron.

The chemical process frequently follows a coordinated pathway, in which bonding interactions between the 1,3-dipole and the dipolarophile occur concurrently. This produces a cyclic intermediate, which rearranges to form the final five-membered ring product (Scheme 1.1). In some situations, a stepwise procedure may occur, depending on the electronic and steric characteristics of the reactants. Common 1,3-dipoles include nitrile oxides, nitrones, azides, and diazo compounds. The reaction is a flexible method for constructing heterocyclic compounds, with numerous applications in medical chemistry, material science, and natural product synthesis (Clayden, Greeves and Warren 2012).

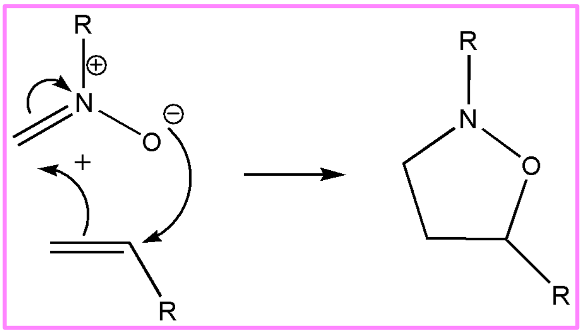

Scheme 1.1: A simple mechanism of a 2+3 annulation reaction

1.6 Problem statement

Insulin is the primary hormone that regulates blood glucose levels and malfunction in its production or action causes a serious disease called diabetes. Diabetes is a chronic metabolic illness that affects several systems in the body, resulting in a variety of health issues and it has a significant influence on both physical and mental health (Abel *et al.* 2024; Yameny 2024). The secretion of insulin into the bloodstream is prompted by an elevation in circulating blood glucose levels (Vargas et al. 2020). The creation of a sensor for insulin detection would be highly advantageous, as insulin concentration can be used to assess the severity of diabetes, based on insulin production and glucose metabolism (Asadpour et al. 2021). Thus, the creation of a sensitive, selective, straightforward and cost-effective insulin detection technology is essential for the diagnosis and monitoring of diabetes.

Research indicate that the presence of insulin antibodies is a strong predictor of diabetes development in individuals with a genetic predisposition. The methods employed yield results that are highly specific, sensitive, and reliable. Nonetheless, these methods present notable disadvantages, including high costs, extensive time requirements, the necessity for substantial sample preparation, and the emission of harmful radiation. Electrochemical assays, known for their high sensitivity and selectivity, offer quick response times, easy automation, dependable results, and relatively low costs, making them capable of overcoming the limitations of these methods.

Moreover, electrochemical immunosensors, which employ biosensor technology, are the most effective method for detecting antibodies to antigens. Indole, pyrazole and their derivatives, have demonstrated immense potential for use in the development of new pharmacological activities with distinct chemical structures and exceptional bioactivities. In this study, an alternative approach is examined, different from the therapeutic approach. Indole-pyrazole derivatives will be incorporated to enhance the sensitivity of the electrochemical immunosensors for the detection of insulin antibodies. According to existing literature, there are very few reports that have utilised indole- pyrazole derivatives to enhance the sensor's sensitivity. Therefore, we identified an opportunity to investigate and additional design new novel derivatives.

1.7 Aim and Objectives

Aim

To detect insulin antibodies using an electrochemical immunosensor modified with indole-pyrazole capped nanoparticles

The objectives are to:

- Synthesise indole pyrazole ligands (indole and chromone) using one pot synthesis, characterise them by Fourier transform infrared spectroscopy (FTIR), Nuclear magnetic resonance (NMR), and Time-of-flight mass spectrometry (TOF-MS) and evaluate their biologicals activities (Mutagenicity, Inhibition of α-amylase and α-glucosidase and Cytotoxicity)
- Prepare lemon peel extract and perform phytochemical screening.

- Synthesise capped indole-pyrazole Gold and Cobalt nanoparticles using their salt precursors, lemon peels extract and indole-pyrazole derivatives.
- Characterise the nanoparticles by Ultraviolet Visible Spectrometry (UV-Vis), Scanning electron microscope (SEM) and FTIR.
- Prepare and fabricate electrochemical immunosensor for detection of insulin antibodies
- Characterise the proposed immunosensor's fabrication steps using CV and EIS techniques
- Optimise the experimental conditions (concentration of antibody & incubation time and temperature) and electrochemical parameters such as pH, scan rate, and deposition time by CV
- Investigate the immunosensor's response to insulin and the immunosensor's selectivity, sensitivity, reproducibility, and stability by SWV

1.8 Structure of the Thesis

- **Chapter 1: Introduction**

Presents the introduction, background, problem statement, objectives of the study, and thesis outline

- **Chapter 2: Literature Review**

Provides a comprehensive review of existing research and scholarly work on electrochemical immunosensors, plant extract-based nanomaterials, and indole-pyrazole derivatives

- **Chapter 3:Theoretical Principles**

The fundamental theoretical principles supporting the applied methods for experimental research are discussed in this chapter.

- **Chapter 4: Methodology**

Describes the synthesis and characterisation techniques used for indole-pyrazole derivatives and nanomaterials, their biological studies, and the fabrication of electrochemical immunosensors for the detection of insulin antibodies.

- **Chapter 5: Results and Discussion**

A discussion of the results obtained from the experimental methods for the synthesis of indole-pyrazole derivatives and indole-pyrazole cappednanoparticles. Study their application in the development of electrochemical immunosensors for the detection of insulin antibodies.

- **Chapter 6: Concluding Remarks and Future Recommendations**

This chapter highlights significant findings from experiments and presents concluding observations and proposes directions for future research, for electrochemical detection of insulin antibodies.

2 CHAPTER 2: LITERATURE REVIEW

This chapter provides a comprehensive summary of the current research and academic work on the detection of diabetes biomarkers, including but not limited to insulin. The chapter also discusses electrochemical immunosensors, plant extract-based nanomaterials, and indole-pyrazole derivatives

2.1 Diabetes Biomarkers

Biomarkers make it possible to categorise diseases and risk factors uniformly. They can increase our understanding of the underlying pathophysiology of diseases. And, map the full disease spectrum from the first signs to the end stage. Hemoglobin A1c (HbA1c) is the most common biomarker for the diagnosis of prediabetes and diabetes. HbA1c is formed when glucose binds to the amino terminus of the β-subunit of hemoglobin (El Malahi *et al.* 2022). Followed by glucose, which is an important clinical biomarker in diabetes patients. That detected through blood (Liu, Yue and Cui 2023) and insulin antibodies, which are indicators of the development of diabetes in people who are genetically prone to the disease (Farrokhnia *et al.* 2022).

Electrochemical sensors play a key role in the current laboratory and clinical analysis of a variety of chemical and biological targets . The recent development of sensor has offers new opportunities to improve the performance of electrochemical sensor (Wang *et al.* 2017; Cruz *et al.* 2020). Thapa and Heo created an electrochemical sensor to test blood glucose and HbA1c concentrations. Using a single sample drop (Blood), on a single strip biosensor employing screen-printed carbon electrode (Thapa and Heo 2023). Mandali *et al.,* 2023 detected HbA1c using electrochemical and point-of-care analysers (Mandali *et al.* 2023). Singh and co-works detected glucose in blood sample as diabetes biomarker by a highly sensitive electrochemical sensor employing quantum dots (Singh *et al.* 2023).

Insulin biomarker has demonstrated potential for quantification in human serum from type 1 diabetes by electrochemical techniques (Wardani *et al.* 2023). Wardani *et al.* 2023*,* detected insulin from blood serum samples using an electrochemical sensor. The latter was developed using a gold electrode modified with carboxylate multiwalled carbon nanotubes and molecularly imprinted polymer (Wardani *et al.* 2023). Wang *et al*. 2023a, also detected an insulin antibodies and the glutamate decarboxylase antibody for early detection of diabetes type 1 (Wang *et al.* 2023a). Glutamic acid decarboxylase (GAD) catalyses the conversion of glutamic acid to gamma-aminobutyric acid in pancreatic islet cells. Autoantibodies against GAD are found in patients with type 1 diabetes mellitus (Wang *et al.* 2023a). Apart from electrochemical techniques, there are several techniques applied for detection other significant diabetes biomarkers (Table 2.1).

Table 2.1: Analytical procedures for the determination of Diabetes biomarker

Biomarker	Technique	LOD	Reference
Glucose and insulin	fluorescence sandwich immunoassay	-	(Poudineh *et al.* 2021)
Insulin	liquid chromatography-mass spectrometry	10 pg/mL	(Judák *et al.* 2020)
Diabetic nephropathy	mimetic immunoassay	20 nmol/L	(Wang *et al.* 2023b)
Insulin	Electrochemical Lateral-Flow Immunoassay	12 pM	(Nandhakumar *et al.* 2023)
Anti-glutamic acid decarboxylase	Enzyme-linked immunosorbent assay	-	(Cecchin *et al.* 2023)
Glutamic acid decarboxylas	Autoantibody radiobinding assays	-	(Lind *et al.* 2024)
MicroRNAs	Fluorescence biosensor	9.5 pM	(Mei *et al.* 2025)
α-glucosidase	Colorimetric-fluorescence dual-mode biosensor	0.03 U/L,	(Chen *et al.* 2025)
Glucose	Non-enzymatic fluorescence nanosensor	36.13 μg/dL	(Kansay *et al.* 2024)
α-hydroxybutyrate	Liquid chromatography-mass spectrometry	-	(Steiner *et al.* 2024)
Insulin glargine	Liquid chromatography coupled to high-resolution mass spectrometry	1.06 mg/L	(Arbouche *et al.* 2023)
Insulin	Electropolymerized, molecularly imprinted polymer (MIP) sensor	1.9 pM	(Arbouche *et al.* 2023)
HbA1c	Electrochemiluminescence device	2 μM	(Zhou *et al.* 2023)
HbA1c	Electrochemical-optical immunosensor	-	(Lakhera *et al.* 2023)
HbA1c	Surface plasmon resonance sensor	-	(Singh *et al.* 2021)
Insulin	Surface plasmon resonance biosensor	-	(Calcagno *et al.* 2024)

2.2 Electrochemical biosensors

Biosensors are analytical devices that combine a biological recognition element (enzyme, antibody, or DNA) with a transducer to detect specific analytes (Jessy Mercy, Girigoswami and Girigoswami 2024) . They are commonly categorised based on the type of signal generated, including optical (Shrikrishna *et al.* 2024), thermal (Kröger and Danielsson 2024) and electrochemical biosensors. Among these, electrochemical biosensors are widely used due to their high sensitivity, rapid response, low cost, and suitability for miniaturisation (Cruz *et al.* 2020). Unlike optical sensors, which rely on changes in light signals, or thermal sensors, which measure heat changes, electrochemical sensors convert a biochemical reaction into an electrical signal (Kröger and Danielsson 2024; Shrikrishna *et al.* 2024).

This makes them especially suitable for real-time monitoring and point-of-care diagnostics. In this study, the focus is placed on the electrochemical category, specifically voltammetric immunosensors, due to their compatibility with nanoparticle-based platforms and their strong performance in detecting disease biomarkers like insulin antibodies. Asadpour *et al* and Liu *et al* developed an electrochemical aptasensor for determination of insulin (Asadpour *et al.* 2021; Liu *et al.* 2021). Farrokhnia and co-works created a ultrasensitive novel electrochemical biosensor for rapid detection of insulin (Farrokhnia *et al.* 2022). Electrochemical immunosensors have inherent merits such as fast detection time, unique sensitivity, cost-viability, and outstanding compatibility with miniaturisation technologies (Anusha *et al.* 2022).

Limited literature exists on the detection and quantification of insulin antibodies using electrochemical immunosensors; however, they are regarded as novel alternatives for identifying biomarkers. (Jozghorbani et al. 2021). There is quite considerable amount of electrochemical immunosensors in detection of biomarkers for different diseases, which shows they can be employed in biological fluids to detect disease biomarkers. For an example Anusha *et al* in 2022, created electrochemical immunosensor based on GCN-b-CD/Au nanocomposite for the monitoring of vitamin D deficiency (Anusha *et al.* 2022). Chen *et al* 2021, did a electrochemical immunosensor prostate specific antigen detection (Chen *et al.* 2021). Jozghorbani *et al* 2021, created electrochemical immunosensor for determination of carcinoembryonic antigen (Jozghorbani *et al.* 2021). Electrochemical immunosensors have also been used to find other biomarkers, like acute myocardial infarction, (Karaman *et al.* 2021), coronavirus (Mojsoska *et al.* 2021; Rahmati *et al.* 2021), microcystin-LR (MCLR) toxin (Yao *et al.* 2021) and cardiac troponin I (Zhao *et al.* 2021a).

2.3 Bionanomaterials

2.3.1 Plant extract-based nanomaterials

Plant extracts typically contain macromolecules, phytochemicals, and compounds that serve as an important source of bioactive compounds for a variety of applications. Including the synthesis of nanomaterials (Alzahrani and Alkhudidy 2021; Hacke, Lima and Kuss 2022) and have attracted considerable interest for the synthesis of bionanomaterials. Due to the abundance of plant sources in nature. Recent research demonstrates that extracts derived from diverse plant tissues (leaves, foliage, seeds, fruits, roots, and tubers) can be utilised effectively, to create stable nanomaterials with intriguing physicochemical and biological properties (Ahmad *et al.* 2019). Phytochemicals present in plants, such as amino acids, tannins, flavonoids, proteins, carbonyls, alkaloids, vitamins, polysaccharides, phenols, and ketones, are used as a source of reducing agents to convert the metal ions into atoms. Thereby facilitating the biosynthesis of metal nanoparticles (Hosny *et al.* 2022; Singh 2022).

Diabetes is a chronic disease that affects the entire world and one of the most rapidly expanding global health crises of the 21st century. As a result, many scientists are concentrating on developing inexpensive alternatives utilising bionanomaterials to detect their biomarker for early diagnosis. It is another disease that has received attention in the plant-based biosensor research. Using the *Zingiber officinale* root, Dönmez *et al* 2020. developed an amperometric glucose biosensor based on the green synthesis of spherical zinc oxide nanoparticles (ZnONPs) in the range of approximately 17-40 nm. The incorporation of ZnONPs increased the electrocatalytic activity of the immobilised enzyme and enhanced its efficacy. In the presence of interfering substances such as uric acid and ascorbic acid, the biosensor exhibited adequate anti-interference properties (Dönmez 2020). Table 2.2 displays additional bionanomaterials derived from various plant extracts used in the development of electrochemical biosensors for disease biomarkers, including but not limited to diabetes.

Table 2.2: Bionanomaterials from different plant extracts and their biomarker**.**

Extract	Nanomaterials	Biomarker	Reference
Allium sativum	rGO-AgNPs	Cancer	(Moussa *et al.* 2022)
E. tereticornis	AuNPs	Lung cancer	(Nazarpour, Hajian and Sabzvari 2020)
S. mukorossi	rGO/Au	Liver disease	(Kasturi *et al.* 2021)
Crocus sativus L	AgNPs	Maple syrup urine disease	(Karastogianni, Paraschi and Girousi 2022)
Prunus persica	ZnONPs	Diabetes	(Muthuchamy *et al.* 2018)
Fragaria× ananassa	ZnONPs	Tuberculosis	(Mgwili 2017)
Pyrus	AgNPs	Tuberculosis	(Mgwili 2017)
Bambusa	AgNPs	Diabetes	(Jayarambabu *et al.* 2023)
Camellia Sinensis	PtNPs	Diabetes	(Hu *et al.* 2022)
Amaranthus spinosus	AgNPs	Diabetes	(Mamuru *et al.* 2022)
Aconitum heterophyllum	rGO	Diabetes	(Sahu, Chatterjee and Chakraborty 2022)
Citrus × aurantiifolia	rGO/TiO_2	Diabetes	(Gijare *et al.* 2023)

rGO-AgNPs: reduced graphene oxide decorated with silver nanoparticles, rGO/Au: reduced graphene oxide gold nanocomposite, AuNPs: Gold nanoparticles, AgNPs: Silver nanoparticles, ZnONPs: Zinc oxide nanoparticles. rGO/TiO_2: reduced graphene oxide titanium oxide nanocomposite .

2.3.2 Microorganisms-based nanomaterials

Microorganisms (fungi , bacteria, microalgae, and yeast) are everywhere for an example in air, soil, and water, and they are too small to be seen with the naked eye. In addition, certain microorganisms are harmful to humans and can cause infections, while others are important in maintaining human health (Gomaa 2022; Jeevanandam *et al.* 2022). The synthesis of bionanomaterials utilizing microorganisms have strike a great spark, especially for anticancer, medical diagnosis, antimicrobial, and biosensor. The microbially mediated synthesis of bionanomaterials is broadly divided into intracellular and extracellular approaches (Figure 2.1). The microbial synthesis mechanism of metal nanoparticles it generally initiated through the internalisation of metal ions, which are deposited on the cell surface (extracellular approach) or occurs inside the microbial cells (intracellular approach) (Mohd Yusof *et al.* 2020).

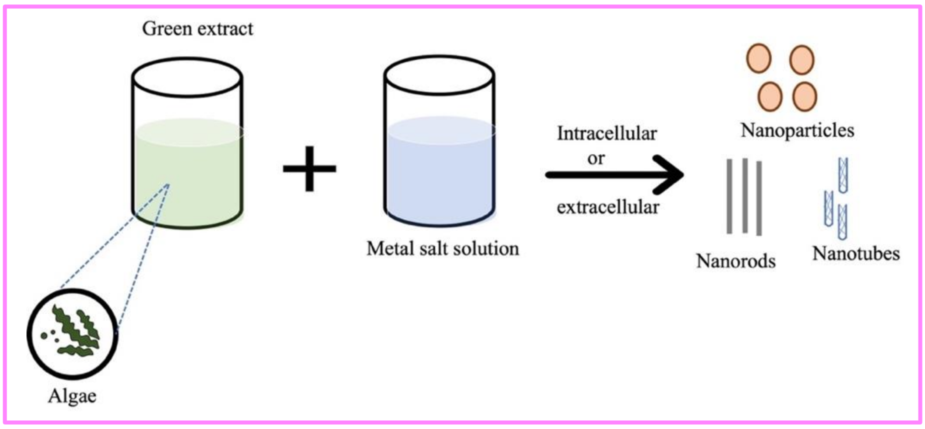

Figure 2.1: Schematic representation of the synthesis of different bionanomaterials from algae.

The synthesis has several important advantages and properties, such as: The obtained nanomaterials have specific, morphology, dimensions and chemical composition. They are easy to handle and cultivate microbiological cells, can be propagated and have great adaptability to different environmental conditions (Mazloum-Ardakani, Barazesh and Moshtaghioun 2019; Jeevanandam *et al.* 2022). Great progression has been made in electrochemical sensing utilising microbial-based nanomaterial. For example, Mazloum-Ardakani *et al* 2018*,* produced gold nanoparticles using saccharomyces cerevisiae yeast, paired them with graphene oxide (GO) nanosheet to development electrochemical biosensor (Mazloum-Ardakani *et al.* 2018). Mazloum-Ardakani also synthesised Cu_2O-carbon dots and gold nanoparticles nanocomposite using the same saccharomyces cerevisiae yeast strains creating an aptasensor based on electro-synthesised conducting nanocomposite (Mazloum-Ardakani, Barazesh and Moshtaghioun 2019). Green algae have higher biological activity and availability and grow much faster, Elgamouz and co-works reported the synthesis of silver nanoparticles capped using the green algae (*Noctiluca scintillans*) extract for biosensing of hydrogen peroxide (Elgamouz *et al.* 2020).

2.3.3 Protein-based nanomaterial

Proteins are an essential part of all biological systems and can come from plant or animal sources such as elastin, silk, resilin, keratin and collagen. These proteins have chemically distinct amino acid side chains, making them excellent building blocks with defined binding properties(Jeevanandam *et al.* 2022). Protein-based nanomaterials are commonly classified into nanoparticles and nanofibers, which have a wide range of biomedical applications, including drug delivery, biosensing, and diagnostics (Aljabali *et al.* 2022). The nanomaterials can be synthesised using proteins such as whey protein, milk protein, soy protein, legumin, gelatin, albumin, gliadin, elastin, and zein. Ultrasonication, desolvation, emulsification, complex coacervation, and electrospray are the techniques used for the synthesis of protein-based nanomaterials (Verma *et al.* 2018). Figure 2.2 shows a schematic representation of biosynthesis protein-based nanoparticle. Shamsipur *et al.*2020*,* synthesised stable graphene nanosheets from graphite powder through sonication. In the hemoglobin-capped gold nanoclusters (Hb@AuNCs) solution and, formed a nanocomposite for biosensing using an electrochemical technique (Shamsipur *et al.* 2020).

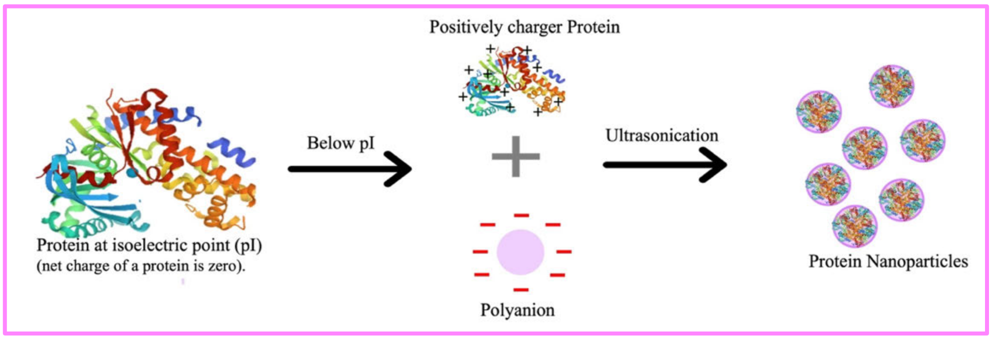

Figure 2.2: Schematic representation of biosynthesis protein based nanoparticles via ultrasonication**.**

Tavakkol and colleagues reported the development of a nanobiocomposite consisting of multiwalled carbon nanotubes (MWCNTs) and zein nanoparticles, dispersed in a water/ethanol mixture and deposited onto a glassy carbon electrode. Electrochemical studies revealed that zein nanoparticles improve the conductivity and catalytic activity of MWCNTs, leading to more sensitive and selective measurements (Tavakkoli *et al.* 2020). Benvidi *et al.* 2018, reported Impedimetric prostate cancer aptasensor based on the use of a glassy carbon electrode modified with titanium oxide nanoparticles and silk fibroin nanofibers. The glassy carbon electrode (GCE) was modified with titanium oxide nanoparticles (TiO_2) and silk fibroin nanofiber (SF) composite (Benvidi *et al.* 2018). Rasitanon *et al.* 2023, synthesised AuNPs from egg white, a food-based substance rich in protein, to develop an electrochemical biosensor. The AuNPs enhanced the transfer of electrons between the electrode and the redox centre, exhibited high sensitivity and were able to increase the stability by more than 85 % (Rasitanon *et al.* 2023).

2.4 Gold Nanoparticles (AuNPs)

Because of their often stated biocompatibility, gold nanoparticles have drawn the most interest among metallic nanoparticles. Gold is one of the metals with lowest chemical reactivity and high electron content (Kesharwani *et al.* 2023). It is simple to produce stable and inert nanoparticles, which are resistant to bacteria (Al-Radadi 2021). AuNPs are used in fields like sensory probes (Tajik, Beitollahi and Torkzadeh-Mahani 2022), medicine (Zhao *et al.* 2021b; Shirzadi-Ahodashti *et al.* 2023) and many other diagnostic tools (Sadique *et al.* 2022). Due to their biocompatibility, stability, oxidation resistance, surface plasmon resonance (Catanzaro *et al.* 2023), and low toxic activities (Rey-Méndez, Rodríguez-Argüelles and González-Ballesteros 2022; Shirzadi-Ahodashti *et al.* 2023). Techniques such as physical, chemical and biological; are used to produce them.

However; the physical and chemical approaches have been reported to have negative effects on human health and the environment (Pechyen *et al.* 2021; Rey-Méndez, Rodríguez-Argüelles and González-Ballesteros 2022).

The biosynthesis of nanoparticles by many biological agents, including plants (Hosny *et al.* 2021; Li *et al.* 2021; Zhao *et al.* 2021b) is taken into consideration as greener syntheses (Hassanisaadi *et al.* 2021; Li *et al.* 2021; Zhao *et al.* 2021b). Due to the non-safe and detrimental consequences of the physical and chemical methods. In electrochemical immunoassay the nanomaterials integration has established the foundation for ultra-sensitive biomarker detection. Because of their unique properties, such as large surface area, impressive catalytic activity, admirable biocompatibility, and electrical conductivity. AuNPs can function as a biological platform for binding sulfhydryl or amino groups of antibody molecules through S-Au or N-Au interactions (Tajik, Beitollahi and Torkzadeh-Mahani 2022).

2.5 Cobalt Nanoparticles (CoNPs)

Cobalt nanoparticles (CoNPs) have received great attention from researchers due to their unique applications in various fields such as antimicrobial activity (Zaib *et al.* 2020), electrochemical sensing (Šišoláková *et al.* 2020) and photocatalytic (Vinayagam *et al.* 2023). And have attracted considerable attention because they are much more economical than the noble metal nanoparticles (Kharade Suvarta *et al.* 2020). They show a variety properties such as magnetic, catalytic and electrical because of their large surface area (Ahmed, Tariq and Mudassir 2021). There are several physical and chemical methods (Kytsya *et al.* 2022; Zhang *et al.* 2022; Khan *et al.* 2024) for the synthesis of

CoNPs that may pose a risk to the environment due to the presence of toxic chemicals. Therefore, adopting environmentally friendly production methods for CoNPs is necessary.

2.6 Lemon peel extract

Lemon peels are a rich source of various active phytochemicals such as polyphenols, flavonoids, alkaloids, terpenoids, tannins,carotenoids, essential oils, amino acids, dietary fibre, minerals and vitamins, with very high functional properties. These phytochemical are natural alternative reducing agents for nanomaterial synthesis (Jahan and Isildak 2021; Verma, Gupta and Singh 2021). Phytochemicals are certain non-nutritive plant chemicals with some disease-preventive properties, and there are different ways in which they can work (Mathew, Jatawa and Tiwari 2012). Phytochemicals serve as reducing and capping agents in synthesising metal nanoparticles using plant extract (Alzahrani and Alkhudidy 2021; Singh 2022). All these factors help to make lemons peels as an excellent source of reducing and stabilising agents for green synthesis of nanoparticles.

The usage of these bioactive lemon peel waste can give an eco-friendly and low-cost platform for the synthesis of novel nanoparticle. There are reports on the green synthesis of various nanoparticles such as AuNPs (Alzahrani and Alkhudidy 2021), zinc oxide nanoparticles, titanium oxide nanoparticles (Meydanju, Pirsa and Farzi 2022), nanoparticles (Alvi *et al.* 2021), zirconium nanoparticle (Salih *et al.* 2021), silver nanoparticles (Jahan and Isildak 2021; Nahar *et al.* 2021), calcium carbonate nanoparticles (Garg *et al.* 2021) and copper oxide nanoparticles (Tshireletso, Ateba and Fayemi 2021), from lemon peel extract have been published. In addition to lemon peels, various parts of the lemon have been utilised in the synthesis of nanomaterials. Table 2.3 presents the parts of the lemon, including the lemon juice, seeds, and leaves.

Table 2.3: Nanomaterials synthesised using lemon extract

Lemon Extract	Nanomaterial	Application	Size/nm	Reference
Juice	MgONPs	Photocatalytic activity	5 - 99	(Alam *et al.* 2024)
Leaves	AgNPs	Antibacterial Efficacy	9.4 - 36	(Nassar *et al.* 2024)
Peels	AuNPs	Antimicrobial Properties	-	(Bratovcic and Dautovic 2024)
Leaves	CuONPs	-	69 - 77	(Oudah Mezan and Khalaf Jabbar 2024)
Juice	Cr_2O_3NPs	Antibacterial activities	44 - 72	(Adnan and Mohammed 2024)
Juice	NiONPs	Optical properties	27	(Salvi *et al.* 2024)
Seeds	CuNPs	Biodiesel production.	50	(Chia *et al.* 2022)
Whole fruit	ZnONPs	Optical properties	62 - 77	(Kem *et al.* 2022)
Seeds	ZnONPs	Antibacterial activity	53	(Sakthivel *et al.* 2022)
Leaves	AgNPs	Antibacterial Activity	-	(Costa *et al.* 2021)
Leaves	Carbon quantum dots	Fluorescent probe	-	(Venugopalan and Vidya 2023)
Juice	BiNPs	Catalytic activity	50-100	(Mahiuddin and Ochiai 2022)
Peel	SeNPs	Antifungal agent	65 -1 00	(Desouky *et al.* 2025)
Juice	CuONPs	Thermal conductivity	42	(Jebali, Gómez-Merino and Colangelo 2025)

2.7 Pyrazoles and Indoles derivatives

The electrochemistry of indole and pyrazole derivatives has been studied previously, where they were either detected using electrochemical sensors or incorporated into nanocomposites for novel electrode platforms (Majola *et al.* 2023; Shao *et al.* 2023; Dey *et al.* 2024; Joshi *et al.* 2024). However, their application in biosensing remains limited. The use of indole and pyrazole derivatives in electrochemical sensors is still emerging, their chemical structures offer distinct advantages for surface functionalisation. Both compounds contain nitrogen-rich heterocycles that are known for their ability to coordinate with metal surfaces, which can promote stable nanoparticle capping. The presence of lone pairs on the nitrogen atoms allows for strong metal - ligand interactions, supporting the structural stability of the nanomaterial (Serpell, Cookson and Beer 2020) . Furthermore, their conjugated π-electron systems contribute to enhanced electron delocalisation, which is favourable for electron transfer processes in electrochemical detection. Given the favourable electronic properties of indole and pyrazole individually, their fusion into a single hybrid scaffold may further enhance π-electron delocalisation and provide an extended conjugated system.

This structural integration is expected to facilitate more efficient charge transfer at the sensor interface, potentially improving the electrochemical response. These properties suggest that indole-pyrazole derivatives may serve as effective molecular bridges between the biological recognition element like antibodies and the sensor surface, enhancing the sensitivity and signal response of the sensor (Fabitha *et al.* 2022; Moscoso *et al.* 2023) . Because they can interact noncovalently with various enzymes and receptors in live organisms, providing them a diverse spectrum of functions and biological applications (Coy-Barrera and Quiroga 2024). Shao and co-workers also demonstrated the utility of indole-based systems in biosensing, presenting a wireless electrochemical sensor for detecting the phytoregulator indole-3-acetic acid using gold nanoparticles and a 3D reduced graphene oxide-modified carbon electrode(Shao *et al.* 2023). While they have not yet been widely applied in this specific context, their potential can be supported by both their coordination chemistry and electronic behaviour.

2.7.1 Multicomponent reactions

In a single process, multicomponent reactions can convert three or more basic precursors into complex molecules (Qi *et al.* 2021). Their benefits include the avoidance of the long purification procedures that are associated with traditional stepwise syntheses, and the efficiency of bond formation, atom economy, product diversity and complexity (Wang *et al.* 2021b; Wang *et al.* 2021c). The synthesis of new indole-pyrazole will employ multicomponent reactions through the 3 + 2 annulation approach. Makhanya et al. 2020 employed multicomponent processes to synthesise fused indole-pyrazole through 3 + 2 annulation (Makhanya, Gengan and Kasumbwe 2020). In addition to Makhanya et al. 2020, several studies have explored the use of multicomponent process 3 + 2 annulation to synthesise target compounds.

Wang *et al*. 2021b conducted a synthesis of tetracyclic tetrahydroquinoline derivatives using a multicomponent reaction including isocyanide, allenoate, and 2-aminochalcone (Wang *et al.* 2021c). In 2021, Qua and colleagues synthesised α-quaternary chiral β-lactams by a synergistic copper/palladium-catalysed multicomponent process (Qi *et al.* 2021)Wang *et al.* 2021a also employed a multicomponent process for the synthesis of secondary amines (Wang *et al.* 2021b). Zhang *et al.* 2021 synthesised hydrobenzoimidazoles from para-quinamines and 1,3,5-triazinanes by a formal [3+2] annulation process (Zhang *et al.* 2021). BabuáGudise, conducted a [3+2] regioselective annulation reaction of 2-arylidene-1,3-indandiones for the synthesis of spirocyclopentenes (BabuáGudise 2021).

3 CHAPTER3: THEORETICAL PRINCIPLES

The chapter concentrates on the fundamental theoretical principles that guided the techniques employed in the experimental studies. This includes the characterisation techniques used for structural confirmation of the indole-pyrazole derivatives, the characterisation of nanoparticles, and the characterisation and testing of the electrochemical immunosensors.

3.1 Nuclear magnetic resonance

Nuclear magnetic resonance (NMR) is a type of spectroscopy used for identifying functional groups and determining atomic interactions inside molecules (Solomons and Fryhle 2012; Solomons, Fryhle and Snyder 2016). It employs radiofrequencies, generally between 10-1000 MHz, to examine magnetic properties and related energy of nuclei. The absorption of radiofrequency energy occurs when nuclei are situated in a strong external magnetic field (De Graaf 2019). There are two techniques, 1D NMR, which generates a single spectrum that displays the chemical shift, intensity, and coupling of nuclei in a molecule. 2D NMR enhances the capabilities of 1D by integrating information from two dimensions, frequently utilising two distinct nuclei or spin interactions (Solomons, Fryhle and Snyder 2016).

1D and 2D NMR were used for confirming the structure of the recently synthesised indole-pyrazole derivatives. For 1D NMR, proton NMR and APT (Attached Proton Test) were used. Proton NMR gives insights on hydrogen (proton) atoms within a molecule. APT is a carbon-13 NMR technique used to confirm the carbon atoms (CH, CH_2, CH_3, and quaternary carbons). For 2D, COSY (Correlation Spectroscopy), HSQC (Heteronuclear Single Quantum Coherence), and HMBC (Heteronuclear Multiple Bond Correlation) were used. COSY assists in determining the coupling between adjacent protons in a molecule. HSQC confirms hydrogen coupling with the single carbon bond attachment (CH, CH_2, and CH_3). HMBC helps confirm the coupling between hydrogens and the quaternary carbons.

3.2 Time-of-flight -mass spectrometry

Mass spectrometry (MS) is used to identify unknown compounds by determining their molecular weight. It involves the formation of ions in a mass spectrometer, followed by separation and detection of the ions based on mass and charge. And generates a mass spectrum, which is a graph with the x-axis representing the formula weights of the detected ions and the y-axis representing the abundance of each detected ion. The x-axis is labelled m/z, where m is mass and z is charge (Appendix 7 and 13). The sample is subjected to high vacuum and irradiated with a beam of high-energy electrons (approximately 70 eV, or approximately 6.7×10^3 kJ mol^{-1}), resulting in the ionisation of molecules. This technique is referred to as electron impact (EI) ionisation mass spectrometry.

The electron beam's effect displaces a valence electron from gas phase molecules, resulting in a +1 charge and an unpaired electron. Which is referred to as the molecular ion (m+·) (Solomons, Fryhle and Snyder 2016). In mass spectrometry, there are various kinds of mass analysers, including quadrupole, Fourier transform, ion trap, and time-of-flight (TOF) analysers. TOF-MS is used in this study, which separates ions based on their flight times over known distances. The m/z ratio is calculated by measuring the time it takes an ion to travel a specific distance with a specific kinetic energy. The separation of ions is based on their velocity and kinetic energy. Ions with lower m/z ratios move faster than those with higher m/z ratios (Brais *et al.* 2021).

3.3 Ultraviolet Visible Spectrometry

Visible spectroscopy serves as an effective analytical method, employing light in the Ultraviolet (UV) or visible spectrum with wavelengths between 200 and 800 nm. This technique is versatile, capable of analysing both colourless compounds in the UV range (400-200 nm) and coloured compounds in the visible range (800-400 nm). It measures the specific wavelengths of UV or visible light that are absorbed or transmitted by a sample relative to a reference or blank (Ríos-Reina and Azcarate 2022; Mandru, Mane and Mandapati 2023). Different molecules absorb different amounts of energy, which can be represented by an absorption spectrum: a graph with absorbance on the y-axis and wavelength on the x-axis. The absorption spectrum can be used to determine the sample's λmax (maximum absorbance wavelength) and concentration. This is based on Beer-Lambert's Law, which states that "the absorbance is proportional to the path length through the sample and the concentration of the absorbing species". Equation 3.1 displays the mathematical representation of the Beer-Lambert law (Mandru, Mane and Mandapati 2023; Kiteto and Mecha 2024).

$$A\ \lambda = \varepsilon c b \qquad \textbf{Equation 3.1}$$

Where A is the absorbance, ε the molar extinction coefficient, c the concentration of the absorbing species and b the path length. UV absorption spectra result from the transition of electrons in a molecule or ion from a lower to a higher energy level. UV emission spectra are produced by the reverse transition. UV radiation possesses adequate energy to promote or excite the valence electrons in a molecule or ion from a ground state orbital to a higher energy level, excited state orbital, or anti-bonding orbital, which can be observed as absorption (Picollo, Aceto and Vitorino 2019). The maxima and intensities of absorption bands vary by sample or substance due to the molecular structure of compounds. Interacting molecules' light absorption also depends on sample concentration. This creates a unique relationship between the substance and its UV-Vis spectrum. Full spectrum can be used for quantitative or qualitative (Ríos-Reina and Azcarate 2022). Herein the UV-Vis spectrum is used to preliminarily evidence the synthesis of the nanoparticles at their corresponding maxima based on literature.

3.4 Fourier transform infrared spectrometry

Spectroscopic techniques, such Fourier transform infrared (FTIR), allow rapid, direct, and cost-effective analysis with minimal sample preparation. Multiple studies provide FTIR spectra results that identify functional groups, thus confirming the structural characterisation of molecules. It emits bands and spectra that serve as a distinctive identifier of a particular molecular structure and chemical bonding (Lago *et al.* 2021; Theakstone *et al.* 2021). The infrared spectrum is divided into three regions: near-infrared (NIR) from 12,500 to 4,000 cm^{-1}, mid-infrared (MIR) from 4,000 to 400 cm^{-1} and far-infrared from 400 to 10 cm^{-1}(Nandiyanto, Ragadhita and Fiandini 2023).There are two main sampling techniques for FTIR spectroscopy: reflection and transmission: The reflection method is widely used to obtain infrared spectra without sample preparation and without causing damage. It contains both internal and external reflections. The transmission technique is a straightforward method that involves passing an infrared beam straight through a sample, measuring the energy transmitted, and creating a spectrum. Sample preparation is necessary because the sample must be sufficiently thin to prevent saturation of the absorption signal (Wang and Wang 2021).

When a molecule is exposed to infrared light, it absorbs a specific amount of the incident radiation at a particular energy or frequency, resulting in vibrational excitation from the ground state to a higher vibrational energy state. The distinct pattern of infrared absorption by a specific molecule or functional group generates characteristic bands in their FTIR spectra. The band position is influenced by the following: the mass of vibration, the nature of molecular bonds, the intra- and inter-molecular environment, the coupling with other vibrations and the band height correlates with the concentration of relevant chemical moieties. The band width offers an indication of intermolecular interactions, which can be analysed qualitatively and/or quantitatively based on their position, shape, and intensity (Theakstone *et al.* 2021; Wang and Wang 2021). Herein, the FTIR was used to verify the functional groups or structural characteristics of the indole-pyrazole derivatives. Additionally, to verify the phytochemicals involved in the synthesis of the nanoparticles and determine whether the indole-pyrazole derivatives were successfully incorporated in the synthesis of the nanoparticles.

3.5 Scanning electron microscope

The scanning electron microscope (SEM) is an instrument that provides a high-resolution electronic image of the exteriors of a variety of substances; it emits a beam of rays that enables the creation of the images. It is typically used to investigate the structures and interactions of materials (Dery and Zaixiang 2023). SEM can function in two modes: secondary electron detection and transmission electron microscopy (TEM). Scanning electron (SE) images possess a significant depth of field, making them particularly effective for displaying surface details. They provide a pseudo-three-dimensional representation of surface topography and help with the extraction of quantitative data regarding particle size distributions and shapes. TEM images provide enhanced spatial resolution and offer a two-dimensional depiction of particles. (Bals and Epple 2023; Khursheed 2024).

SEM comprises an electron source, electromagnetic lenses, detectors, sample chambers, and a computer for displaying results. The electrons generated by the electron gun are accelerated through a series of lenses and apertures to produce an optimal electron beam. The materials are impacted by electrons from the electron gun. The coils generating the electron beams is rotate to scan the sample surface. Signals are generated and identified by the detector solely when the emitted electron beams interact with the sample. Secondary electrons play a significant role in the formation of high-quality images. As, the rays emitted from the electron gun hit the surface of any material. They are reflected and are called the Back-Scattering Electrons (BSE) which helps us to comprehend how a particular element is distributed in a sample. Thereafter, a three-dimensional picture is processed (Ali, Zhang and Santos 2023; Dery and Zaixiang 2023). The SEM utilized to analyse Indole-Pyrazole capped nanoparticles provides high-resolution imaging and compositional insights for understanding their morphology, size, and surface features.

3.6 Energy dispersive X-ray spectrometer

Energy-dispersive X-ray spectroscopy (EDS) is an analytical technique utilised for determining the chemical composition of a material. The technique captures and analyses the characteristic X-rays emitted from a sample subjected to electron irradiation, using either SEM or TEM. The characteristic X-rays arise from inelastic electron scattering within the sample, successive ionisation of certain atoms. The relaxation of outer-shell bound electrons into the vacant states created in the lower shells of ionized atoms follows. This de-excitation can occur either radiatively, producing characteristic X-rays, or nonradiatively, resulting in the emission of Auger electrons. Both processes generate element-specific signals (Hodoroaba 2020; Forte *et al.* 2024; Walther 2024).The elemental composition of the successfully synthesised indole-pyrazole capped nanoparticles is confirmed using EDS.

3.7 Electrochemical Techniques

Electrochemical techniques are analytical methods used to investigate chemical reactions that involves electron transfer. These techniques assess electrical properties like voltage, current, or charge to better understand the redox behaviour, reaction kinetics, and material characteristics of a system. The techniques are classified into two categories: static and dynamic. Static techniques encompass direct potentiometry and potentiometric titration, while dynamic techniques comprise potentiation and galvanostatic methods (Huang, Zhu and Kianfar 2021). Electrochemical techniques, such as CV, square wave SWV and EIS, which are categorised as dynamic methods were chosen in this study due to their simplicity, sensitivity, cost-effectiveness, and rapidity (Santos *et al.* 2022). And, have resulted in the development of sensors exhibiting higher sensitivity and decomposition capabilities (Wang *et al.* 2021a). Measurements are conducted using a three-electrode system that includes a working electrode: (WE) where the reaction of interest takes place; a reference electrode (RE) that ensures a stable potential for accurate measurement; and a counter electrode (CE) that completes the circuit by balancing the current at the working electrode, as illustrated in Figure 3.1 (Wang *et al.* 2021a; Sharma and Chand 2023).

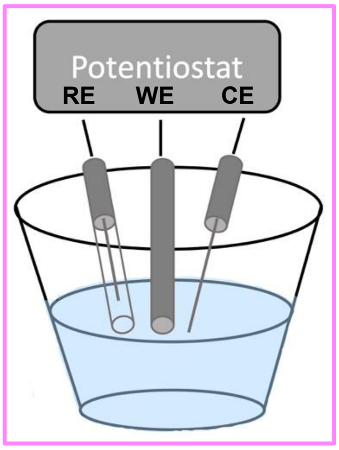

Figure 3.1: Schematics illustrating the three-electrode setup employed in electrochemical measurements.

3.7.1 Cyclic Voltammetry (CV)

Cyclic voltammetry, a method involving potential sweeps, is likely the most frequently employed electrochemical technique due to its straightforward measurement process. The CV offers significant insights into the reactions occurring at the electrode surface and the behaviour of electrochemically or chemically active species. It has been used to gain insights into the preliminary electrochemical investigations of frontier systems, characterise electrodes, and observe reactions. It works by applying a linearly varying voltage to a working electrode and measuring the resultant current response. The potential is scanned from an initial value to a predetermined limit and subsequently reversed, generating a cyclic waveform. As potential changes occur, oxidation and reduction reactions transpire at the working electrode, producing distinctive peaks in the current (Figure 3.2) (Wang *et al.* 2021a; Yamada *et al.* 2022).

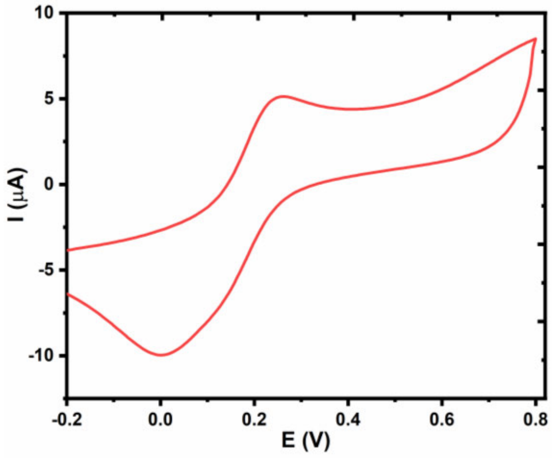

Figure 3.2: A CV voltammogram produced during electrochemical measurements**.**

3.7.2 Square Wave Voltammetry (SWV)

SWV combines both the advantages of cyclic and pulse voltammetry, delivering superior analytical performance and the capacity to yield both mechanistic and kinetic insights into electrochemical processes compared to other electroanalytical methods (Guziejewski, Smarzewska and Mirceski 2023; Kokoskarova *et al.* 2023; Megale and De Souza 2023). In SWV, a sequence of equal amplitude pulses is applied under a staircase potential; during each forward pulse, the chemical species diffuses to the electrode surface and is promptly reduced or oxidised. In a backward pulse, the chemical species that was recently oxidised or reduced reverts to its original state in a reversible reaction, or no reaction transpires in an irreversible system. The present values are recorded immediately prior to and at the conclusion of each pulse, with the net currents plotted against the corresponding potentials of the staircase waveform, yielding a Gaussian signal(Figure 3.3) (Guziejewski, Smarzewska and Mirceski 2023; Kokoskarova *et al.* 2023; Megale and De Souza 2023).

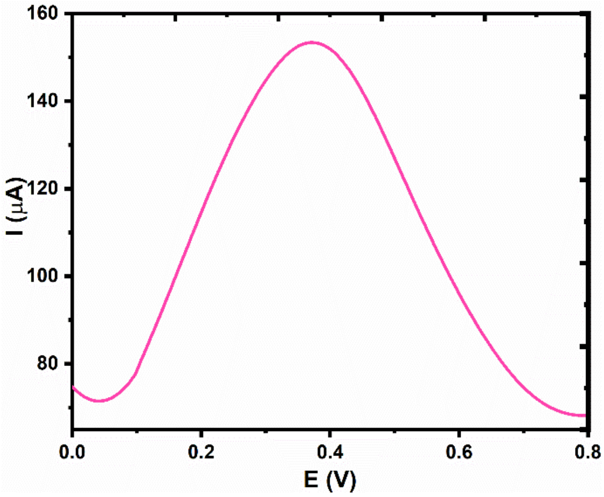

Figure 3.3 A SWV Voltammogram produced during electrochemical measurements**.**

3.7.3 Electrochemical Impedance Spectroscopy (EIS)

EIS is an effective electrochemical method used to investigate the resistance and capacitance of materials by applying a small AC voltage across a spectrum of frequencies and assessing the system’s response. This method is extensively applied in the investigation of reaction kinetics, battery performance, electrode/electrolyte interfaces, and biosensors. In contrast to other electrochemical techniques, EIS offers valuable insights into the different processes that take place across various time scales, including charge transfer, diffusion, and double-layer formation. The results are generally illustrated in Nyquist plots (Figure 3.4a), which facilitate the interpretation of impedance behaviour through equivalent electrical circuits. A Nyquist plot illustrates the real and imaginary parts of impedance, typically creating a semicircular shape that indicates charge transfer resistance. By fitting experimental data to an equivalent circuit model (Figure 3.4b), one can extract parameters such as solution resistance, charge transfer resistance, and capacitance, facilitating a more profound comprehension of electrochemical systems (Hallemans *et al.* 2023; Lazanas and Prodromidis 2023; Zhang *et al.* 2023a; Li *et al.* 2024).

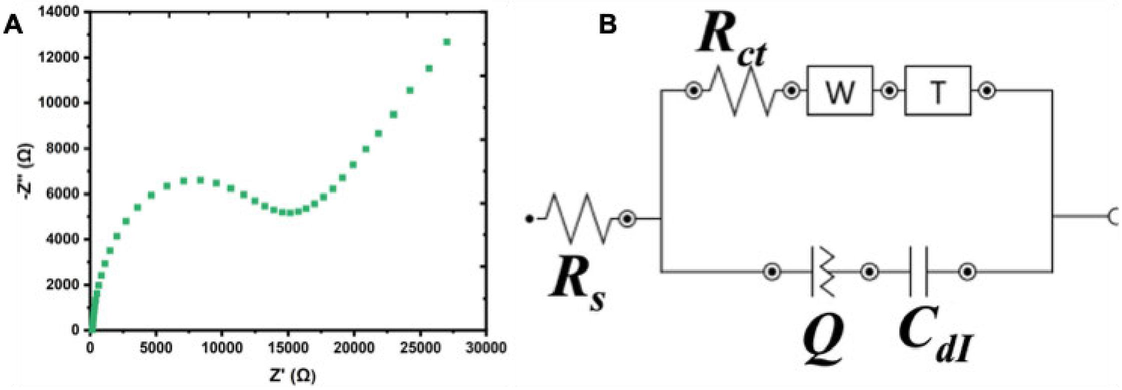

Figure 3.4: (**A**) Nyquist plots and (**B**) Equivalent circuit model.

4 CHAPTER 4: RESEARCH METHODOLOGY

This chapter highlights the key methodologies used in this study, including the synthesis of indole-pyrazole and metal nanoparticles fused with indole-pyrazole derivatives. It also covers in vitro testing for cancer and diabetes, as well as the application of nanoparticles in developing electrochemical immunosensors for detecting insulin antibodies.

4.1 Reagents and materials

Lemons purchased from a local supermarket in Durban, South Africa (SA). Ferric chloride ($FeCl_3$), 25 % Ammonia solution (NH_4OH) (2), Sulphuric acid (H_2SO_4), Lead (II) acetate [$Pb(C_2H_3O_2)_2$], Mercuric chloride ($HgCl_2$), Potassium iodide (KI), Cobalt nitrate $Co(NO_3)_2{\cdot}6H_2O$, Dimethyl sulfoxide (DMSO), Gold(III) chloride trihydrate ($HAuCl_4.3H_2O$), Recombinant insulin protein (antigen), Monoclonal Insulin antibody (K36AC10), Phosphate-buffered saline (PBS), Bovine serum albumins (BSA), Human serum albumin (HSA), Immunoglobulins (IgG), *N*, *N*, dimethyl formamide, L-glutathione (GH), Glucose, Uric acid, Dopamine, Cholesterol, Potassium dihydrogen phosphate (KH_2PO_4), Indole-3-carboxaldehyde, Chromene-carbaldehyde, Thiosemicarbizide, Indole, Silica gel-coated aluminium plates, hexane, ethyl acetate, Acetonitrile, Indium chloride Ampicillin, Lung adenocarcinoma (A549) and Hepatocellular carcinoma (Hep-G2), Human embryonic kidney (HEK 293), MTT (3-(4,5-dimethylthiazol-2-yl)-2,5-diphenyltetrazolium bromide), Doxorubicin, Sodium Azide, Acarbose, α-amylase, α-glucosidase, Dipotassium hydrogen phosphate (K_2HPO_4), Potassium ferrocyanide ($K_4Fe(CN)_6$), Potassium hexacyanoferrate($K_3Fe(CN)_6$), Folin-Ciocalteu Reagent (FCR), Tannic acid, Bromocresol green, Atropine, Chloroform and Quercetin were purchased from Sigma Aldrich. *Salmonella typhimurium* strains TA 98 and TA 100 were supplied as slice cultures by the Medical Research Council of Durban (MRC). Platinum electrode (PtE) was supplied by Metrohm (South Africa). Insulin antigen and antibody were reconstituted in phosphate buffer (7.4) and stored at 20 ℃. BSA, and GSH were dissolved in phosphate buffer (7.4) at 0.2 (%m/v) and 10 mM concentrations, respectively, and stored at 4 ℃ in the fridge. Electrolyte solution for electrochemical readings was prepared by dissolving $K_3[Fe(CN)_6]$ and $K_4[Fe(CN)_6]$ in deionized water at 5.0 mM concentration and stored away from sunlight. The solvents used were of synthetic quality.

4.2 Characterization Techniques

The Stuart SMP10 apparatus was used to determine the melting point of the synthesised compounds. Fourier Transform Infrared (FTIR) spectroscopy, recorded using Attenuated Total Reflectance (ATR), was employed to identify functional groups and confirm the presence of characteristic bonds. Nuclear Magnetic Resonance (NMR) spectroscopy was used to elucidate the molecular structure, with chemical shift values reported on the δ scale and coupling constants (*J*) in hertz. Time-of-Flight Mass Spectrometry (TOF-MS) provided accurate mass measurements and helped confirm the molecular weight of the compounds. The Agilent Cary 60 UV-Vis spectrophotometer was used to investigate the optical properties of the synthesised materials and to confirm nanoparticle formation through characteristic surface plasmon resonance (SPR) bands. Scanning Electron Microscopy (SEM) was used to examine the surface morphology of the nanoparticles, while Energy Dispersive X-ray Spectroscopy (EDS), conducted with a Tescan MIRA3 RISE SEM, provided elemental composition data to confirm the presence of expected elements within the nanomaterials.

4.3 Chemistry of indole-pyrazoles

4.3.1 Synthesis of 2,3-dihyro-3-(1*H*-indol-3-yl)pyrazolo[3.4-*b*]indole-1(8*H*)-carbothioamide (4a)

Scheme 4.1 shows the synthetic route for bis indole-pyrazole **4a** which was accomplished through a one-pot synthesis. Equimolar (1 mmol) of the following substances was added to a 100 mL round bottom flask: Indole-3-carboxaldehyde **1**, and thiosemicarbizide **2**, then made up with 25 mL acetonitrile. The mixture was refluxed between 95 and 100 °C for 4 hours with magnetic stirring in the presence of indium chloride catalyst (1 mmol). After 4 hours, 1 mmol of indole **3** also purchased from Sigma Aldrich was added, then the mixture was refluxed for 12 hours. Thin layer chromatography (TLC) was used to monitor reaction progress using silica gel-coated aluminium plates with an eluent of 3:2 hexane/ethyl acetate, which showed the appearance of a new spot. After cooling, the crude product was poured into ice water to precipitate and then filtered to collect the solid products (orange) remaining after filtering. It was then purified by column chromatography using a solvent system of hexane and ethyl acetate (86:14) to obtain compound **4a** in good yield of 85 %.

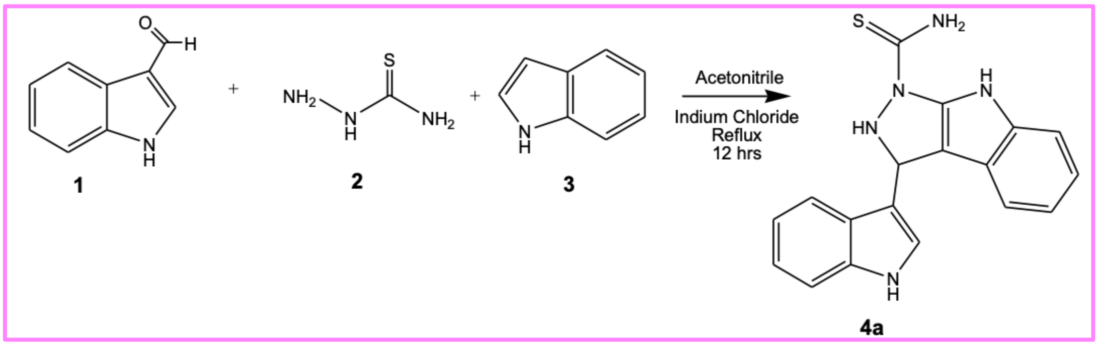

Scheme 4.1: Synthetic route for bis indole-pyrazole via one pot synthesis.

4.3.2 Synthesis of 2,3-dihydro-3-(4-oxo-4*H*-chromen-3-yl)pyrazolo[3,4*b*]indole-1(8*H*)-carbothiamide (4b).

Equimolar (1 mmol) of 3-formylchromone **1b** and thiosemicarbizide **2** were added to a 100 mL round bottom flask, then made up with 25 mL acetonitrile. The mixture was refluxed between 95 and 100 °C for 4 hours with magnetic stirring in the presence of indium chloride catalyst (1 mmol). After 4 hours, 1 mmol of indole **3** was added, then the mixture was refluxed for 12 hours. TLC was used to monitor reaction progress using silica gel-coated aluminium plates with an eluent of 3:2 hexane/ethyl acetate, which showed the appearance of a new spot. After cooling, the crude product was poured into ice water to precipitate and then filtered to collect the solid products (brick-red) remaining after filtering. It was then purified by column chromatography using a solvent system of hexane and ethyl acetate (86:14) to obtain compound **4b** in good yield (80 %). Scheme 4.2 illustrates synthetic route for chromone indole-pyrazole **4b.**

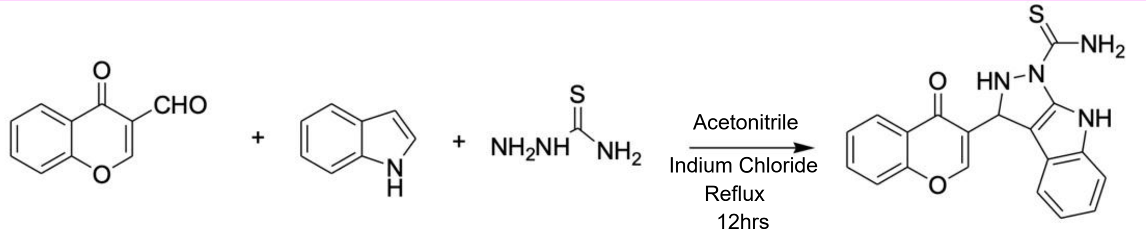

1b **3** **2** **4b**

Scheme 4.2: Synthetic route for chromone indole-pyrazole via one pot synthesis.

4.4 Biology of indole-pyrazoles

4.4.1 Mutagenicity

The Salmonella mutagenicity experiment was performed using a modified version of the protocol of Maron and Ames (1983). *Salmonella typhimurium* strains TA 98 and TA 100 were supplied as slice cultures by the Medical Research Council of Durban (MRC). Both strains were obtained from broth cultures after initially being supplied as frozen disc cultures. Using a flamed bacteriological needle, culture discs were removed aseptically and then inoculated into a sterile 250 mL flask containing 25 mL of nutrient broth (Oxoid) and 78 µL of ampicillin (8.0 mg/mL). The flask was placed in a shaking incubator at 150 rpm at 37 °C for 16 hours. This resulted in an optical density at 660 nm between 1.2 and 1.4. Salmonella TA 100 and TA 98 (100 µL) were combined with 2 mL of histidine/biotin top agar (0.05 mM). Thereafter, the mixture was plated on a minimal glucose agar plate and incubated at 37 °C for 48 h, it was vortexed. Well-separated colonies from plates were used as primary broth cultures. The main broth cultures were divided into colonies on separate plates.

Thereafter, the master plate colonies were inoculated with nutrient broth. These cultures were then maintained at 37 °C for 24 hours on a shaker set at 150 rpm. For the anti-mutagenicity tests, the compounds were dissolved in a DMSO solution to give concentrations of 10, 100, and 1000 µg/mL. The active control was sodium azide (NaN_3), a strong mutagenic agent. 5 µg/mL DMSO was used to dissolve the NaN_3. Three plates were used for each concentration of test compound. 100 µL of bacterial culture, 100 µL of test compound and 2.9 mL of soft agar at 45 °C were placed in a sterile test tube. The tube was placed onto minimal glucose agar plates after rapid vortex mixing. The plates were inverted and incubated at 37°C for 48 hours after the agar layer had solidified. The frequency of mutations was then determined and recorded. Mutant frequency was estimated by dividing the number of revertant colonies by the number of colonies in the negative control (Maron and Ames 1983).

$$\textbf{Mutant Frequency} = \frac{\textbf{Revertant number of colonies}}{\textbf{No.of colonies negative control}} \qquad \textbf{Equation 4.1}$$

4.4.2 *In vitro* inhibition of α-amylase and α-glucosidase: Diabetes

To measure the inhibitory activity of α-amylase and α-glucosidase synthesised compounds, the method described by Ashraf et al. is followed. The percentage of inhibitor-free control sample was used to express inhibitory activity (Equation 4.2) (Ashraf *et al.* 2020).

$$\% \ \mathbf{inhibition} = \frac{(\mathbf{A.control} - \mathbf{A\ sample})}{\mathbf{A.control}} \times \mathbf{10} \qquad \textbf{Equation 4.2}$$

Acarbose (250 µL) at various concentrations (6.25-100 µg/mL) was added separately for 20 minutes at 37 °C with 500 µL of porcine pancreatic amylase and 500 µL of 1.0 U/mL α-glucosidase solution in 100 mM Phosphate buffer incubated (pH 6.8). The reaction mixture was added to 250 µL of 1% starch and 250 µL of pNPG (4-nitrophenyl-β-D-glucopyranoside) solution, each dissolved in 100 mM phosphate buffer (pH 6.8). The mixture was then incubated at 37 °C for 1 hour. Then, 10.0 mL of DNA (3,5-dinitrosalicylic acid) colour reagent was added and boiled for 10 minutes. The absorbance of the resulting mixture for α-amylase and α-glucosidase was measured at 540 nm and 405 nm, respectively. A blank value was created to adjust the extinction. Acarbose solution was used as a positive control.

4.4.3 Cytotoxicity: Cancer

The cytotoxicity of the synthesised compounds toward lung adenocarcinoma (A549) and hepatocellular carcinoma (Hep-G2) was evaluated using the MTT (3-(4,5-dimethylthiazol-2-yl)-2,5-diphenyltetrazolium bromide) assay and was purchased from Sigma Aldrich. A 90 µL cell volume of 1 x 105 was added to each well of 96-well microtiter plates, with the surrounding wells filled with phosphate-buffered saline to prevent the medium from evaporating during incubation. The plates were then incubated at 37 °C for 24 hours. This gave the cells enough time to attach to the wells of the plate. The stock solution (1000 µg/mL) was diluted with a growth medium to ensure that all sample solutions were prepared consistently.

Each well of the plate was then treated with 10 µL of different concentrations (100, 50, 25, 20, 15, 10 and 5 µg/mL) of the sample solution. The cell-containing microtiter plates were then incubated for two days at 37 °C in a humidified incubator with a 5 % CO_2 atmosphere. The MTT reagent (5 mg/mL) was added to each well. The plates were then incubated at 37 °C for another four hours. After incubation, the medium was removed and 100 µL aliquot of DMSO (dimethyl sulfoxide) was added to each well to dissolve the formazan crystals formed in metabolically active cells. A microplate reader (BioTek Instruments, Inc. USA) was used to measure absorbance at 570 nm with a reference wavelength of 650 nm (Kasumbwe *et al.* 2017). The inhibitory concentration of the tested compounds (IC_{50}) was determined using the Graph Pad Prism6 software.

4.5 Chemistry of lemon peel extract

4.5.1 Phytochemical screening

Lemon peels possess numerous active phytochemicals that contribute to the synthesis of nanomaterials. To ascertain the phytochemicals potentially involved in nanoparticle synthesis, both qualitative and quantitative screens were conducted on those that are most common in lemons (Rahman *et al.* 2022; Thapa *et al.* 2022; Charmkar, Dubey and Ganeshpurkar 2024; Sitio and Akmal 2024).

For the preparation of the aqueous extract, the lemon peels were rinsed with deionised water and allowed to air dry, they were blended into a fine powder. To prepare the extract, 5.0 g of the powder was added to 100 mL of deionised water, and the mixture was boiled for one hour. Following a muslin cloth filter, the filtrate was then centrifuged for an hour and collected the upper layer, which was then stored for later use at 4 °C in the refrigerator.

4.5.1.1 Qualitative analysis

The content of total soluble phenols, flavonoids, tannins, and alkaloids in the lemon peel extract was determined using procedures reported by Mathew (Mathew, Jatawa and Tiwari 2012) and Rubio-Delgarito (Rubio-Melgarejo *et al.* 2020). The results were expressed with the presence (+) or absence (−) of the phytochemical compound evaluated.

- **Phenols**

Three drops of 10 % ferric chloride were added to 1 ml extract; the formation of a blue colour indicated the presence of phenol.

- **Flavonoid**

Few drops of 10 % ammonia were added to 2 mL of the extract, followed by 1 ml of concentrated sulphuric acid. The disappearance of the yellow colour indicated the presence of Flavonoids.

- **Tannin**

Few drops of 10% lead acetate solution were added to 5 mL of aqueous extract. The formation of white precipitate indicated the presence of tannins.

- **Alkaloids**

1 mL of the lemon peel extract was treated with 1 mL of Mayer's reagent. The appearance of a pale precipitate indicated the presence of alkaloids.

4.5.1.2 Quantitative analysis

Quantitative determination of phytochemical content in lemon peel extract was carried out using Agilent Cary 60 UV-Vis spectrophotometer at different wavelengths corresponding to each phytochemical according to a method described by Otitolaiye (Otitolaiye *et al.* 2023).

- **Phenols**

(Otitolaiye *et al.* 2023)The Folin-Ciocalteu reagent (FCR) technique was used to determine the phenolic content of the extract Otitolaiye *et al.* 2023). phenol in the extracts reduces the FCR, resulting in the formation of a blue colour that becomes darker as the phenol content increases. The solution was covered and left in a dark cupboard at room temperature for 5 minutes. Next, 1.5 mL of 5 % Na_2CO_3 was added and mixed well, then kept at room temperature in a dark area for two hours. The absorbances were measured at 750 nm. Tannic acid was prepared at different concentrations (5, 10, 25, 50, 75, 100, 150 and 200 µg/mL) to draw the standard curve, and the amount of phenolics in the extract was calculated using the milligram (mgTAE/g) equivalents tannic acid. The test was carried out in three repetitions

- **Flavonoid**

The flavonoid concentration was determined using the aluminium chloride colorimetric method (Otitolaiye *et al.* 2023). As a reference standard, quercetin (1 mg/mL) was prepared at different concentrations (10, 50, 75, 100, 150, 200, 250 and 300 µg/mL). A volume of 1 mL of quercetin or extract was combined with 0.3 mL of 5 % sodium nitrite. The solution was then incubated for 5 minutes at room temperature. 0.3 mL of 10% aluminium chloride was then added, and the solution was allowed to stand at room temperature again for 5 minutes. The solution was then combined with 2 mL of 1 M NaOH and allowed to stand at room temperature for an additional 10 minutes. After measuring the absorbance at 510 nm, the flavonoid concentration was expressed in milligrams of quercetin equivalent per gram of extract (mgQE/g). Triplicate experiments were performed.

- **Alkaloid**

A solution of bromocresol green (BCG) was used for this test (Otitolaiye et al. 2023). BCG (23 mg), 0.67 M NaOH (3 mL), and distilled water (5 mL) were combined to produce a fresh bromocresol solution. The resulting solution was then diluted and made up to 300 mL with distilled water. Atropine reference solution (0.05 mg/mL) was prepared with distilled water and diluted to concentrations of 10, 50, 75, 100, 150, 200, 250, and 300 µg/mL. To extract the alkaloids, 1 mL of the extract and 1 mL of standard (at different concentrations) were independently added to 5 mL of the bromocresol green solution and 5 mL of the phosphate buffer (pH 4.7). 4 mL of chloroform were then added and shaken vigorously. In this way, a BCG-chloroform complex was created, and the resulting chloroform fraction was collected and placed in a test tube. Next, the absorbance was measured at 470 nm. The unit of measurement for total alkaloid content was milligrams of atropine equivalent per gram of extract (mgAU/g). Each determination was performed three times.

- **Tannin**

The FCR was used to estimate the tannin content. In this method, the tannin content of the extract reduces the fluorescence conversion ratio (FCR) of molybdate (VI) ions to molybdate (V) ions. Furthermore, a blue colour is created that becomes stronger as the tannin concentration increases. For the reference standard, different concentrations of 1 mg/mL gallic acid were prepared in the range of 10, 50, 100, 200, 300, 400 and 600 µg/mL. Next, 7 mL of distilled water, 0.5 mL of 10% FCR, and 1 mL of 35 % Na_2CO_3 solution were added to a test tube containing 100 µL of extract or standard. The mixture was incubated at room temperature for 10 minutes. The absorbance of the extracts and the gallic acid standard was measured at 725 nm. Tannin concentration was measured as equivalent milligrams (mgTAE/g) of gallic acid per gram of extract (Otitolaiye *et al.* 2023). Each determination was performed in triplicates.

4.6 Chemistry of Indole-Pyrazole capped Nanoparticles

4.6.1 Synthesis of Cobalt Nanoparticles

For the synthesis of these nanoparticles, a method reported by Zaib with minor modification was used (Zaib *et al.* 2020). 10 mL of the lemon peel extract was added dropwise to 20 mL of 0.03 M $Co(NO_3)_2{\cdot}6H_2O$ with constant stirring at 90

°C for 2 hours after that 2 mL of compound **4a** or **4b** solution was added then stirred further at 90 °C for an extra hour. The indole-pyrazole derivatives solutions were prepared by dissolving the compound in 10% DMSO. Reddish pink colour formed which indicated the formation of nanoparticles. After this, the coloured solution was centrifuged at 5000 rpm for 2 hours. Then the separated nanoparticles were washed thoroughly and refrigerated at 4 °C for further use.

4.6.2 Synthesis of Gold Nanoparticles

For the synthesis of AuNPs, 10 mL of lemon peel extract was gradually added to 20 mL of 1 mM $HAuCl_4$ while maintaining steady stirring at 60 °C. After 20 minutes, the light- yellow solution changed to violet, indicating the synthesis of AuNPs. Subsequently, 2 mL of the compound **4a** or **4b** solution was added and stirred at 60 °C for one hour. The nanoparticle solution was centrifuged at 5000 rpm for 20 minutes, and the supernatant was decanted. The separated nanoparticles were thoroughly washed and thereafter stored at 4 °C for future application (Li *et al.* 2021).

4.6.3 Determining the Average Number of Atoms in Nanomaterial

The estimation of the average number of nanomaterials can be conducted through the analysis of SEM images of the nanomaterials. The average core diameters of the particles (D, nm) are computed and presented utilising ImageJ software. Under the assumption of a spherical geometry and a homogeneous composition (Liu *et al.* 2007; Elnoby *et al.* 2018) the average quantity of atoms in nanomaterials (N) for each category of nanosphere is determined using the following Equation 4.3 , where ρ represents the density of nanomaterials (g/cm³) and M denotes the atomic weight of the nanomaterial element.

$$N = \frac{\pi}{6}\frac{\rho D^3}{M}$$ **Equation 4.3**

4.6.4 Determination of Molar Concentrations in Nanomaterial Solutions

The molar concentration of nanosphere solutions (C) was calculated by dividing the total number of the metal atoms (NTotal, which corresponds to the initial quantity of salt introduced into the reaction solution), by the average number of nanomaterial atoms per nanosphere (N), as outlined in Equation 4.4. Where V represents the volume of the reaction solution in litres and NA denotes Avogadro's constant. The reduction of nanomaterial ions to atoms is considered to be entirely complete Liu *et al.* 2007; Elnoby *et al.* 2018).

$$\mathbf{C} = \frac{N_{Total}}{NVN_A}$$ **Equation 4.4**

4.7 Electrochemical analysis

4.7.1 Preparation of the immunosensor

The first step was to clean the Platinum electrode (PtE) manually by polishing with aluminium oxide and electrochemically by cycling 50 times in the potential range of 0.0 to 2.0 V in 5% nitric acid. The electrode was then washed with plenty of deionised water and dried at room temperature. About 5 µL of the nanoparticles (NPs) were dropped onto the electrode surface and then dried at 37 °C for 15 min. This modified electrode was labelled as NPs/PtE. In the next step, 5 µL of GSH solution was dropped onto the NPs/PtE surface, followed by 5 µL of the antigen (50 µg/mL), and incubated at 37 °C for 120 min. The modified electrode was named Anti/NPs/PtE. The L-glutathione (GH) solution was utilised as a spacer to bridge the gap between nanoparticles and protein to address the nonspecific adsorption of the modified electrode and enhance the immobilisation process. GH has carboxylic acid groups and thiol groups with high affinity for metal nanoparticles and proteins (Farrokhnia *et al.* 2022). The thiol group of GH interacts with metal by forming a metal-S bond. The carboxylic acid groups of GH ensure binding to amino groups of proteins such as the insulin antigen. Then, after 3 µL of 1 % BSA was dropped onto the modified electrode to block the nonspecific binding sites and washed thoroughly with the phosphate buffer (pH 7.4). The modified electrode dried with nitrogen and was stored at 4 °C for further use. Figure 4.1 is a typical example of the fabrication of an electrochemical immunosensor

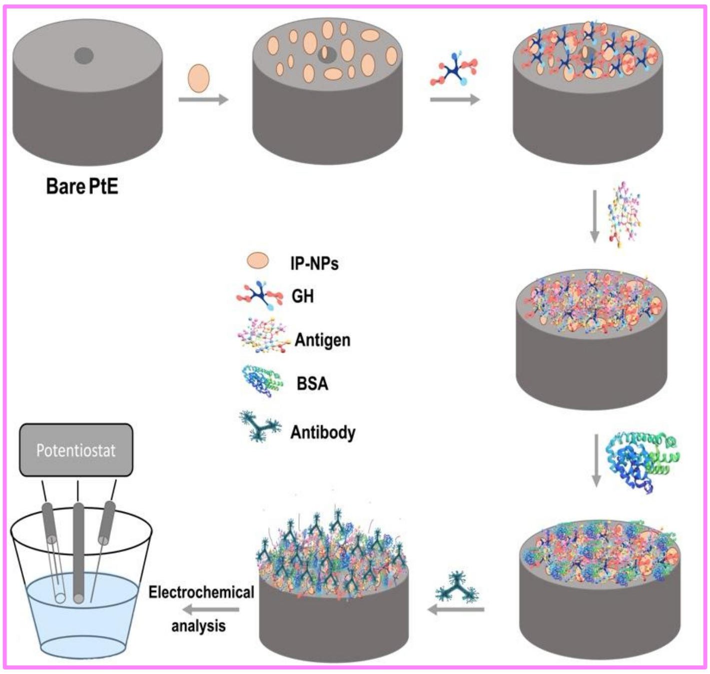

Figure 4.1: Schematic diagram for the fabrication of an electrochemical immunosensor**.**

4.7.2 Immunoassay procedure

The electrochemical measurements CV and SWV were carried out in a phosphate buffer (pH = 6.4) with 5.0 mM $[Fe(CN)_6]^{3-/4}$ solution, with a three-electrode system 797 VA Computrace (Metrohm Herisau, Switzerland). The three-electrode setup consisted of a modified PtE as a working electrode, an Ag/AgCl as a reference electrode, and a carbon rod as a counter electrode. EIS measurements were performed using Metrohm AUTOLAB, PGSTAT 302 with 663A Computrace, in a phosphate buffer (pH = 6.4) with 5.0 mM $[Fe(CN)_6]^{3-/4}$ solution, with a three-electrode system consisting of a modified PtE as a working electrode, an Ag/AgCl as a reference electrode, and a carbon rod as a counter electrode. CV and EIS were performed to confirm surface modification changes, SWV approach was used to quantify target molecule concentration. The CV cycles were performed at a potential of -0.2 V to +0.8 V and a scan rate of 100 mV/s. EIS measurements were performed in the frequency range from 0.1 Hz to 100 kHz. The SWV experiments were performed by scanning the potential from 0 V to 0.80 V with an amplitude of 0.15 V, and a frequency of 50 Hz.

5 CHAPTER 5: RESULTS AND DISCUSSION

This chapter presents the results obtained from the experimental methods for the synthesis of indole-pyrazole derivatives and nanoparticles capped with indole-pyrazole derivatives, and their application in the development of electrochemical immunosensors for the detection of insulin antibodies. This chapter is divided into three parts: Part A: Discuss the design, synthesis, and characterisation of the two novel compounds: bis indole-pyrazole and chromene indole-pyrazole. Although the primary objective of the study is sensor development, these ligands were newly synthesised and therefore subjected to biological assays to preliminarily assess their pharmacological relevance and safety. The aim was to understand their behaviour in biological environments and to explore their multifunctionality as potential bioactive materials. Evaluations included mutagenicity, enzyme inhibition (for diabetes), and cytotoxicity (for anticancer activity). Part B: Discuss the synthesis and characterisation of nanoparticles capped with two aforementioned indole-pyrazole derivatives. Part C presents the outcome of using nanoparticles capped with indole-pyrazole in the fabrication of electrochemical immunosensors to detect insulin antibodies.

PART A: Synthesis and Characterisation of Indole-Pyrazole derivatives

This section discusses the design and synthesis of two indole-pyrazole derivatives using a one-pot synthesis via a 3+2 annulation reaction. Compound **4a** consists of indole and pyrazole scaffolds, while compound **4b** contains indole, pyrazole, and chromone scaffolds. Since these compounds were newly synthesised, their potential pharmacological relevance was preliminarily evaluated through biological assays. These included enzyme inhibition (for diabetes), cytotoxicity (for anticancer activity), and mutagenicity. This provided insight into their bioactivity and behaviour in biological environments, supporting their selection in the later development of the electrochemical immunosensor.

5.1 Chemistry of Indole-pyrazoles

5.1.1 Chemistry of indole-pyrazole 4a

The synthesis of the indole-pyrazole derivatives (Figure 5.1) was accomplished through a one pot approach via 3+2 annulation reaction, with melting points of 150 °C for bis indole-pyrazole **4a** (Orange solid) and 134 °C for chromone indole-pyrazole **4b** (Brick-red solid). Compound **4a** was selected as a template to discuss the plausible mechanism provided in Scheme 5.1, a Schiff base reaction occurred between indole aldehyde **1a** and thiosemicarbizide **2**, yielding an imine product **5a**. Due to the nucleophilicity of enamines, it was attacked by the lone pairs of indole nitrogen **3**, giving an intermediate **6a**. The compound's instability at this point triggered delocalisation of the nitrogen lone pair results in a high electron density on the atom. The latter causes a proton transfer that turns the neighbouring nitrogen atom nucleophilic (**7a**). This triggered the attack of indole's electrophilic carbon while forcing the hydrogen to move away. This hydrogen migrated and attached to the neighbouring nucleophilic nitrogen to stabilise it (**8a**). Aromaticity then occurred, resulting in the stable target compound **4a**. Mechanism for compound **4b** is provided in Appendix 1.

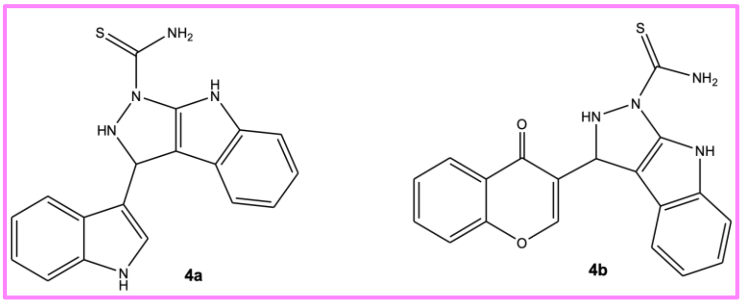

Figure 5.1: The synthesised novel fused indole-pyrazole compounds

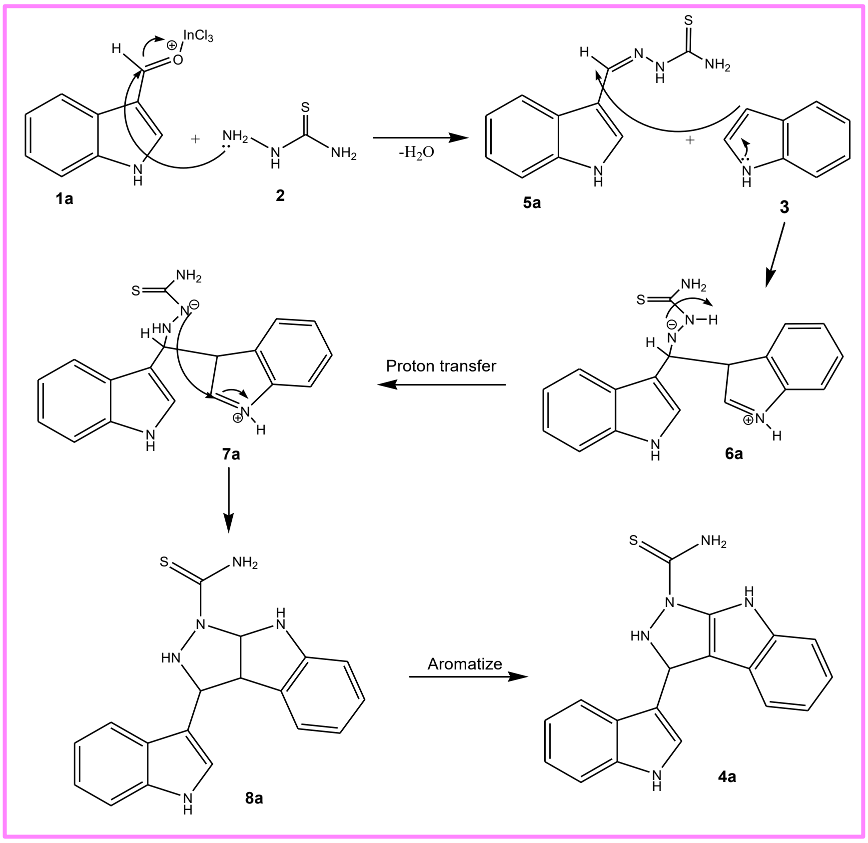

Scheme 5.1: Plausible mechanism for synthesis of compound 4a via 3 + 2 annulation reaction.

5.1.2 Characterisation of Compound 4a

The structural elucidation of compound **4a** utilizing spectroscopic techniques. The characteristic absorption band in the FTIR spectrum (Figure 5.2a) showed absorptions at 3302 cm^{-1} for N-H stretching, 1701 cm^{-1} for C=O stretching, 1617 cm^{-1} due to N-H bending, 1457 cm^{-1} C-N stretching, 1154 cm^{-1} and 744 cm^{-1} due to C=S stretching. The ^{1}H-NMR spectrum showed signals for the nine aromatic protons at ∂ 7.39 (1H, d, *J* = 5.28 Hz, H-4), ∂ 7.38 (1H, d, *J* = 5.28 Hz, H-12), ∂ 7.33 (1H, d, *J* = 5.40 Hz, H-7), ∂ 7.32 (1H, d, *J* = 5.40 Hz, H-15), ∂ 7.02 (1H, t, *J* = 10.08 Hz, H-5), ∂ 7.01 (1H, t, *J* = 10.08 Hz, H-13), ∂ 6.93 (1H, S,*J* = Hz 1.44, H-10), ∂ 6.86 (1H, t, *J* = 9.96 Hz, H-6), and ∂ 6.84 (1H, t, *J* = 9.96 Hz, H-14) in Appendix 2.

APT spectrum (Appendix 3) provided information about carbons present in the **compound 4a.** It showed the presence of ten CH, ∂ 127.4 (C-10), ∂ 126.0 (C-4 and C-12), ∂ 125.8 (C-5 and C-13), ∂ 124.5(C-6 and C-14), ∂ 117.6 (C-7 and C-15), and ∂ 44.3 (C-8). Eight quaternary carbons, ∂ 143.7 (C-2a); ∂ 144.8 (C-3a); ∂ 128. 4 (C-7a); ∂ 190.0 (C-16); ∂ 156.3 (C-15a); ∂ 137.2 (C-11a); ∂ 116.3 (C-8a) and ∂ 124.5 (C-9). ^{1}H-^{1}H-COSY spectrum (Appendix 4) shows the correlation between hydrogens which are coupled to each other. A strong coupling between H-12, H-5 and H-6; and another one between H-13 and H-14. The HSQC spectrum (Appendix 5), illustrates the correlation between ^{1}H and a single carbon bond: H-4 correlate with C-4; H-12 with C-12; H-7 with C-7; H-15 with C-15; H-5 with C-5; H-13 with C-13; H-10 with C-10; H-6 with C-6; H-14 with C-14 and H-8 with C-8. The HMBC spectrum (Appendix 6) which shows the proton and quaternary carbon coupling: H-14 with C-15a; H-8 with C-15a; H-8 with C-9; H-8 with C-8a and H-6 with C-7a. The mass spectrum (Appendix 7), the molecular ion peak at m/z 359.1 [M$^+$ + Na] corresponds to the molecular formula $C_{18}H_{15}N_5S$. Figure 5.2b shows proposed fragments formed by the loss of thioamide and indole.

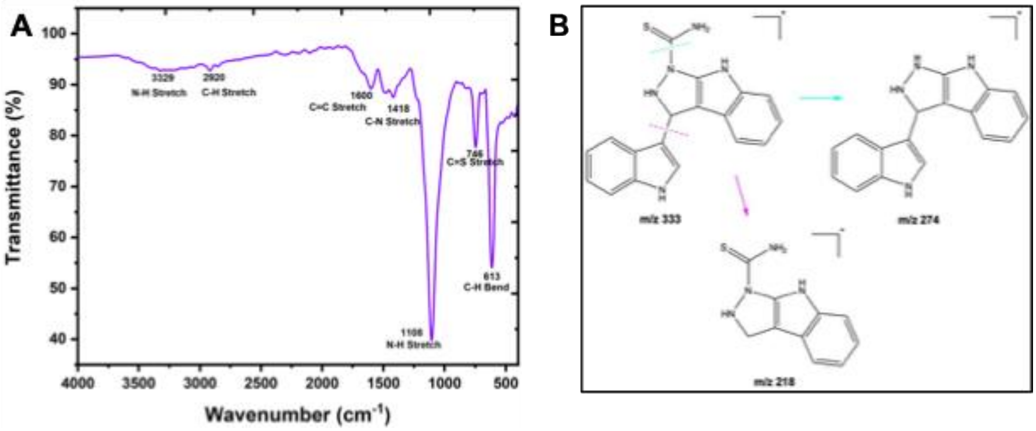

Figure 5.2: (**A**) FTIR spectrum (**B**) Proposed fragmentation of compound **4a.**

5.1.3 Characterization of Compound 4b

FTIR spectrum (Figure 5.3a) showed absorptions at 3302 cm^{-1} for N-H stretching, 1701 cm^{-1} for C=O stretching, 1617 cm^{-1} due to N-H bending, 1457 cm^{-1} C-N stretching, 1154 cm^{-1} and 744 cm^{-1} due to C=S stretching. The ^{1}H NMR spectrum (Appendix 8) showed signals for overlapping NH-3-indole and NH-1-pyrazole at ∂ 6.98 (s, *J* = 1.40 Hz) and aromatic protons at ∂ 8.11 (d, *J* = 6.40 Hz, H-15), ∂ 7.91 (s, H-10), ∂ 7.78 (t, H-14), ∂ 7.59 (d , *J* = 5.60, H-12), ∂ 7.48 (t, H-13), ∂ 7.37 (d, *J* = 7.44, H-4), ∂ 7.37 (d, *J* = 7, 44 Hz, H-7), ∂ 7.08 (t, *J* = 10.12 Hz, H-5), ∂ 6.92(t, *J* = 10.00 Hz, H-6). The APT spectrum (Appendix 9) showed the presence of ten CH, ∂ 155.28 (C-15), ∂ 134.38 (C-14), ∂ 125.69 (C-10), ∂ 124.43 (C-12) , ∂ 121.45 (C-13), ∂ 119.16 (C-

4 and C-7), ∂ 118.85 (C-5 and C-6) and ∂ 112.03 (C-8). Nine quaternary carbons, ∂ 176.16 (C-16 and C-17), ∂ 156.28 (C-9 and C-15a), ∂ 137.18 (C-11a), ∂ 125.75 (C-2a), ∂ 123.84 (C-3a), ∂ 116.28 (C-8a) and ∂ 60.22 (C-7a).

The ^{1}H,^{1}H-COSY spectrum (Appendix 10) showed strong coupling between H-4 and H-6; and between H-7 and H-6. Another strong coupling occurred between H-13 and H-15. The HSQC spectrum (Appendix 11) provided a correlation with proton and a single carbon bond: H-15 with C-15; H-14 with C-14; H-12 with C-112; H-13 with C-13; H-7 with C-7; H-4 with C-4; H-5 with C-5; H-6 with C-6. The HMBC spectrum (Appendix 12) showed the proton and quaternary carbon coupling: H-18 with C-2a; H-15 with C-15a; H-10 with C-9, C-15a and C-16; H-14 with C-15a; H-4, H-7 with C-3a and C-7a; H-5 with C-3a; H-6 with C-7a and C-8a; and H-8 with C-2a, C -7a, C-8a and C-16; respectively. The mass spectrum (Appendix 13), the molecular ion peak at m/z 387.1 [M$^+$ + Na] corresponds to the molecular formula $C_{19}H_{14}N_4O_2S$. Figure 5.3b shows proposed fragments formed.

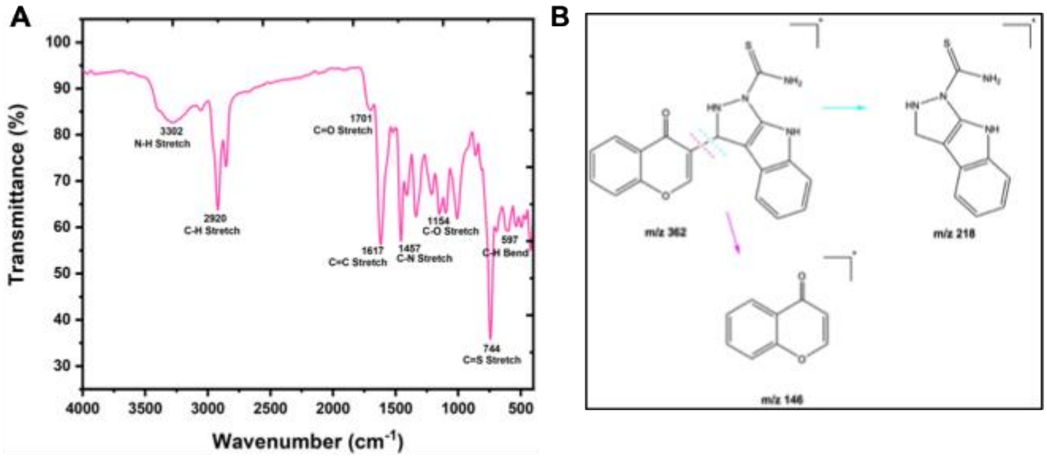

Figure 5.3: (**A**) FTIR spectrum and (**B**) Proposed fragmentation of compound **4b.**

5.2 Biology of indole-pyrazoles

5.2.1 Mutagenicity

Table 5.1 shows the frequency of mutants caused by synthetic compounds in *S. typhimurium* TA 98 and TA 100. Mutant frequency was calculated as a percentage by dividing the number of revertant colonies by the total number of colonies in the negative control sample (Maron and Ames 1983). Mutant frequencies above two were considered mutagenic. According to the results of this study, the compounds did not show any mutagenic properties against the *S. typhimurium* TA 98, and TA 100 strain. Compared to the control (NaN_3), none of the synthesised compounds examined significantly increased the number of revertant colonies. The mutagen NaN_3 was used in the experiment to demonstrate the existence of revertant colonies. NaN_3 is commonly used as a positive control in the Ames test due to its effectiveness even at very low concentrations, reducing the need to handle large amounts overall. Therefore, NaN_3 was excluded at concentrations of 100 and 1000 g/mL. The results of this experiment showed that the number of revertant colonies (Figure 5.4) increased in direct proportion to the concentration.

Table 5.1: Mutagenic response to *S. typhimurium* strain TA 98 and TA 100.

Compounds	**Mutant Frequency of revertant at different concentrations**				
	5 µg/mL	**10 µg/mL**	**20 µg/mL**	**100 µg/mL**	**1000 µg/mL**
4a	0.26±0.03	0.376±0.06	0.391±0.59	0.520±0.06	0.555±0.12
	0.19±0.21	0.310±0.2	0.318±1.74	0.332±0.2	0.517±0.41
4b	0.16±0.01	0.310±0.3	0.332±0.27	0.453±0.25	0.654±0.15
	0.21±0.18	0.345±0.18	0.349±0.15	0.362±0.15	0.512±0.3
Sodium Azide	1.039±0.35	2.01±0.3	3.9±0.2	na	na
	1.055±0.15	2.12±0.2	4.2±0.14	na	na

Values are expressed as mean (±SD), n = 3, unshaded TA 98 and shaded indicate TA 100. na = not applicable, 0 = no activity

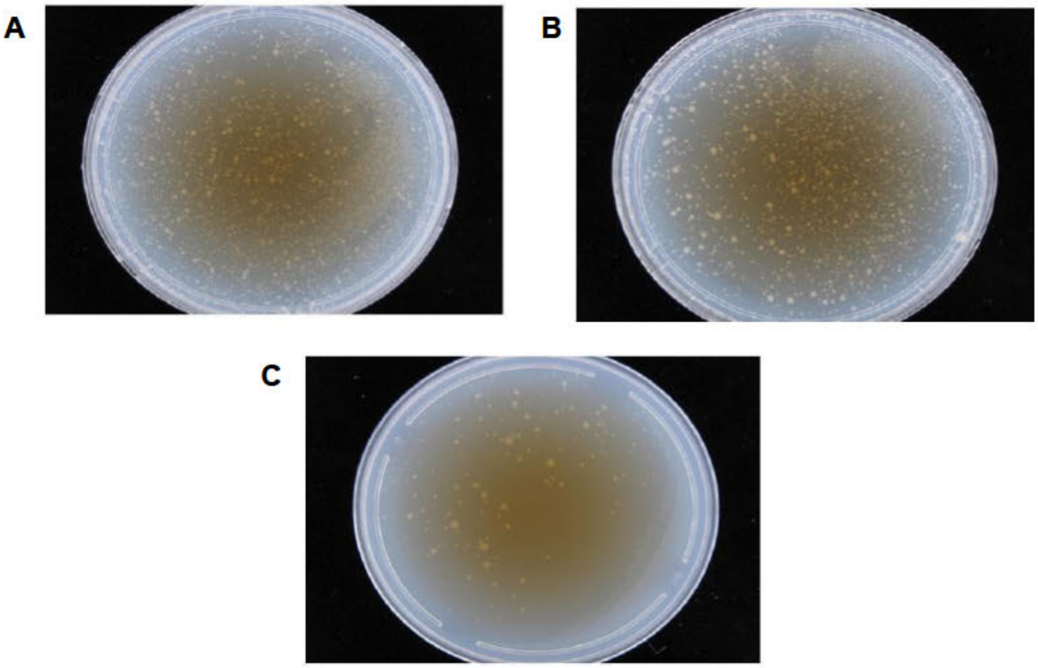

Figure 5.4: Revertant colonies: (**A**) plate with T 100, (**B**) plate with TA98, (**C**) plate with compound 4a at 100 µg/mL demonstrating revertant colonies.

5.2.2 *In vitro* inhibition of α-amylase and α-glucosidase: Diabetes

5.2.2.1 Inhibitory activity against α-Amylase

The α-amylase inhibitory activities of the fused indole-pyrazole compounds were evaluated in comparison to the commercially available acarbose α-amylase inhibitor. Tables 5.2 illustrate the *in vitro* inhibition of α-amylase by the compounds. The IC_{50} values for α-amylase showed that all target compounds showed excellent inhibition against α-amylase at concentrations below 26.6 µg/mL, whereas acarbose had an IC_{50} value of 208.5 µg/mL. Notably, all compounds showed higher half-maximal inhibitory concentrations than the acarbose reference standard. Compound **4a** showed the highest activity with an IC_{50} value of 3.09 µg/Ml. Compound **4b** also, showed significantly higher IC_{50} values of 19.0 µg/mL compared to 208.5 µg/mL of acarbose. Compound **4a** contains an indole aldehyde substitute and **4b** contains chromone aldehyde. Both the indole and chromone moieties exhibit antidiabetic activity (Zhu *et al.* 2021; Niri *et al.* 2022). However, compound **4a** achieved better results, which may be because has a double indole moiety in its structure. Indole has been used as a key pharmacophore for the development of α-glucosidase inhibitors (Hu *et al.* 2024).

Table 5.2: α-amylase half maximal inhibitory concentrations (IC_{50}).

Compounds	**IC_{50} (µg/mL)**
4a	3.9 ± 0.98
4b	19.0 ±1.20
Acarbose	208.5 ± 0.46

5.2.2.2 Inhibitory activity against α-glucosidase

The *in vitro* α-glucosidase inhibitory activities of the synthesised compounds were also evaluated. The IC_{50} values are listed in Table 5.3, with acarbose serving as the reference standard. Compared to the standard inhibitor acarbose, which has an IC_{50} value of 55.4 µg/mL. The compounds showed significant inhibition of α - glucosidase, with IC_{50} values varying between 12.1 and 57.0 µg/mL. Compound **4a** had the highest activity against α-glucosidase with an IC_{50} value of 12.1 µg/mL. Compounds **4b**, on the other hand, showed no significant α-glucosidase inhibitory activity with IC_{50} values of 57 µg/mL compared to standard acarbose, which had 55.4 µg/mL. Based on these findings, compound **4a** was found to be more effective against α-glucosidase than acarbose. **4a** demonstrated lower IC_{50} values compared to previously reported chromone and indole derivatives (Table 5.4). **4b** is still a promising inhibitor, though it is not as strong as **4a**. However, it is comparable to some compounds in Table 5.4.

Table 5.3: α-glucosidase half maximal inhibitory concentrations (IC_{50}**)**.

Compounds	**IC_{50} (µg/mL)**
4a	12.1 ± 0.29
4b	57.0 ± 1.04
Acarbose	55.4 ± 1.14

Table 5.4: Previously reported chromone and indole derivatives for antidiabetic.

Enzyme	Structure Name	IC_{50} (µg/mL)	Reference
α-glucosidase	3-((1H-indol-3-yl)(phenyl)methyl)-4-hydroxy-2H-chromen-2-one	17.84	(Niri *et al.* 2022)
α-glucosidase	(Z)-4-Phenyl-2-(2-((1-(propyl sulfonyl)-1H-indol-3-yl) methylene) hydrazine) thiazole	93.75	(Ullah *et al.* 2023)
α-amylase	2-Amino-4-(3,4-dichloro-2-hydroxyphenyl)-6-(1,3-dioxoisoindolin-2-yl)nicotinonitril	31.74	(Al-Ghorbani *et al.* 2023)
α-amylase	2-Amino-5-oxo-4-phenyl-4H,5H-pyrano[3,2-c]chromene-3-carbonitrile derivatives	15.63	(Farzaneh *et al.* 2024)
α-amylase	4-(4-(4-((2-isopropyl-5-methylphenoxy)methyl)-1H-1,2,3-triazol-1-yl)butoxy)-2H-chromen-2-one	11.72	(Singh *et al.* 2024)

5.2.3 Cytotoxicity: Cancer

The synthesised indole-pyrazoles were examined by MTT assay for *in vitro* cytotoxicity against two human cancer cell lines: lung adenocarcinoma (A549), hepatocellular carcinoma (Hep-G2) and normal human embryonic kidney (HEK 293). The results were compared with the activity of the known anticancer drug, DOX. The cytotoxic activities of the tested compounds were expressed as IC_{50} µg/mL values, which represent the dose that reduces survival to 50%. The results presented in Table 5.5 show that the activity of these molecules varied from low to high. Compound **4b** showed the most promising anticancer properties as it showed better potency against cancer cell lines A549 and HepG-2 with IC_{50} values of 18.7 and 50.07 µg/mL; respectively. In comparison, the positive control drug doxorubicin had IC_{50} values of 2.26 and 3.5 µg/mL; respectively. This interesting activity could be attributed to the structural backbone of compound **4b** which has a chromone moiety in its structure. Both natural and synthetic, are attracting attention in drug development because they exhibit extensive anticancer activities (Sun *et al.* 2022).

Chromones exhibit efficacy against several types of cancer cells, mostly because of the presence of the benzopyran scaffold, which is an exceptional class of chemotherapy agents (Sun *et al.* 2022; Kirishnamaline, Magdaline and Chithambarathanu 2023). On the other hand, compounds **4a** showed weak cytotoxicity against A549 and Hep-G2 with IC_{50} values of 0.939 and 0.411 µg/mL. Notably, the tested compounds **4a** and **4b** had minimal inhibitory effects on the normal human embryonic kidney (HEK) 293, with inhibition percentages of 5.4 and 10.04 % at 100 µg/mL; respectively. The addition of the chromone moiety enhanced the antiproliferative effect of the indole-pyrazole hybrid, and compared to previous studies, compound **4b** demonstrated a stronger effect against cell line A542. Table 5.6 presents published results of derivatives containing chromone, indole, and pyrazole moieties. The findings observed for compound 4b in this study show comparable activity to those reported in previous literature. These biological assays were helps to gain an early understanding of the pharmacological relevance, biocompatibility, and the behaviour of the newly synthesised compounds in biological systems, especially since they were later applied as key functional materials in the immunosensor.

Table 5.5: Half minimum inhibitory concentration against A542 and HEP-G2

Compounds	**Cell lines IC_{50} µg/mL**	
	A549	**HEP-G2**
4a	933.9 ± 1.3	411.02 ± 1.6
4b	18.7 ± 1.4	50.07± 0.8
Doxorubicin	2.26 ± 0.5	3.5 ± 0.6

Table 5.6: Previously reported chromone and indole derivatives for anticancer**.**

Cell Line	**Structure Name**	**IC_{50} (µg/mL)**	**Reference**
Hep-G2	3,5-di((E)-styryl)-1H-pyrazole	408.11	(Pham *et al.* 2020)
Hep-G2	5-Amino-4-((3-(trifluoromethyl)phenyl)diazenyl)-1H-pyrazol-3-ol	47.80	(Fayed *et al.* 2023)
A549	5-((1H-Indol-3-yl)methyleneamino)-N-phenyl-3-(phenylamino)-1H-pyrazole-4-carboxamide	23.70	(Hassan *et al.* 2021)
A549	Benzyl4-(7-methoxy-2,3-dimethyl-4-oxo-4H-chromen-8-yl)−6-methyl-2-oxo-1,2,3,4-tetrahydropyrimidine-5-carboxylate	22.26	(Kirishnamaline, Magdaline and Chithambarathanu 2023)
A549	1,1-bis(3′-indoly)-1-(p-floro phenyl)	36.59	(Mageed, Mohsin and Al-Sahaf 2023)

5.3 Summary

New fused indole-pyrazole derivatives, bis indole-pyrazole **4a** and chromone-indole-pyrazole **4b**, were successfully designed and synthesized via a one-pot 3+2 annulation reaction. Their biological properties were explored to assess potential anticancer and antidiabetic activities. Neither compound showed mutagenic effects against *S typhimurium* strains, indicating safety at this preliminary stage. In cytotoxicity assays, compound **4b** demonstrated strong anticancer activity against A549 and HepG-2 cell lines, with IC_{50} values comparable to the control drug doxorubicin, while compound **4a** exhibited weak activity. In enzyme inhibition assays targeting diabetes-related enzymes, compound **4a** showed excellent inhibitory effects on α-amylase and α-glucosidase, outperforming the standard drug acarbose, whereas compound **4b** had limited activity in this regard. These complementary profiles highlight the multifunctional potential of the synthesised compounds, providing a strong rationale for their further use as ligands in electrochemical immunosensor development.

PART B: Indole-Pyrazole Capped Nanoparticles

In this sub-section, the results of green-synthesised metal nanoparticles (Cobalt and Gold nanoparticles) synthesised using lemon extract and the indole-pyrazole derivatives **4a** (Bis indole-pyrazole) and **4b** (Chromone indole-pyrazole) are discussed. Each metal was used to produce two types of nanoparticles, one capped with **4a** and the other with **4b**. These nanoparticles serve as key functional materials for enhancing the surface properties of the electrochemical immunosensors developed in this study.

5.4 Chemistry of lemon peel extract

5.4.1 Phytochemicals: screening

Understanding the composition of the lemon peel extract is essential to justify its role in the green synthesis of nanoparticles. While the use of plant extracts in nanoparticle synthesis is common, knowing their specific phytochemical makeup provides valuable insight into the active compounds responsible for reducing metal ions and stabilising the resulting nanoparticles. Phenolic acids, flavonoids, tannins, and other bioactive compounds are known to play critical roles in these processes. By identifying the phytochemicals present, this study establishes a clearer link between the synthesis approach and its alignment with the study's overall objective developing stable, functional nanoparticles for sensor applications. A phytochemical screening (both qualitative and quantitative) was performed on the lemon peel extract to identify the key phytochemicals involved in the synthesis of the nanoparticles. Prior to this screening, FTIR analysis was conducted to assist in identifying functional groups present in the extract. The

FTIR spectrum shown in Figure 5.5 displays major peaks at 3298 cm⁻¹ , 1640 cm⁻¹ , and 1017 cm⁻¹. The peak at 3298 cm⁻¹ is indicative of O-H stretching, commonly found in phenolic acids, flavonoids and alcohols that might be present in the extract. The peak at 1640 cm⁻¹ is due to C=C stretching in aromatic or alkene compounds, common in terpenoids or flavonoids (Mathew, Jatawa and Tiwari 2012). At 1017 cm⁻¹ it is common for C-O stretching in primary or secondary alcohols and ethers. For qualitative determination, the presence of phenols, flavonoids, tannins, and alkaloids was tested, with the lemon peel extract testing positive for all. These results are consistent with those reported in the literature, as summarised in Table 5.7

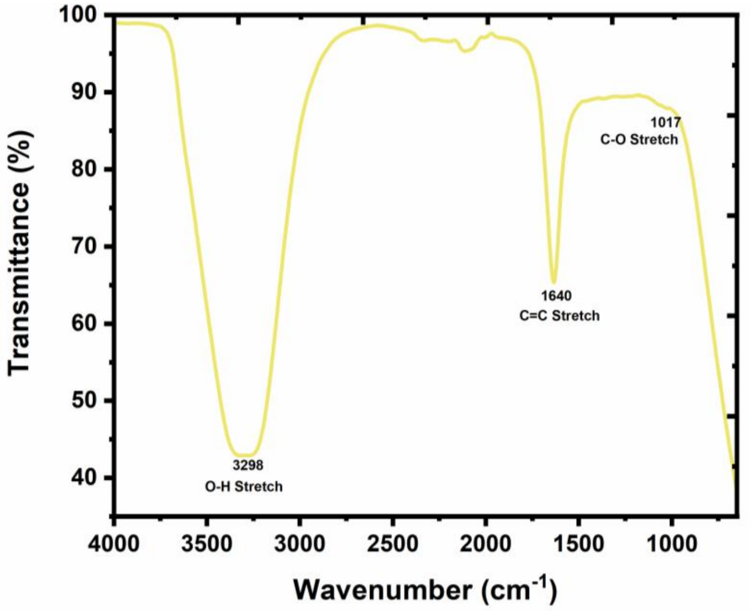

Figure 5.5: FTIR spectrum of lemon peel extract.

Table 5.7: Phytochemicals found in lemon peel extract.

Phytochemicals	**Test performed**	**Result**		**References**
		Current study	**Literature**	
Phenols	Ferric chloride	+	+	(Mathew, Jatawa and Tiwari 2012; Mahmood *et al.* 2021; Verma, Gupta and Singh 2021; Meydanju, Pirsa and Farzi 2022)
Flavonoids	Ammonia	+	+	(Mathew, Jatawa and Tiwari 2012; Mahmood *et al.* 2021; Verma, Gupta and Singh 2021; Meydanju, Pirsa and Farzi 2022)
Tannins	Lead acetate	+	+	(Mathew, Jatawa and Tiwari 2012; Mahmood *et al.* 2021; Verma, Gupta and Singh 2021; Meydanju, Pirsa and Farzi 2022)
Alkaloids	Mayer's	+	+	(Mathew, Jatawa and Tiwari 2012; Mahmood *et al.* 2021; Verma, Gupta and Singh 2021; Meydanju, Pirsa and Farzi 2022)

+ positive test

Quantitative determination of phytochemical content was carried out using Agilent Cary 60 UV-Vis spectrophotometer at different wavelengths. The phenolic and tannin contents were evaluated using a colorimetric reduction-based approach with FCR and tannic acid as the reference standard. The flavonoid content was evaluated using the aluminium chloride method and quercetin as the reference standard. To calculate the quantities, calibration curves for the phytochemicals were created by extrapolation. The calibration curve for phenols

(Figure 5.6a) and tannins (Figure 5.6b) was constructed using concentration of tannic acid and the amounts expressed in mg/g of tannic acid equivalent (TAE). The calibration curve for flavonoids (Figure 5.6c) was constructed using the quercetin concentration and the amounts were expressed in mg/g of quercetin (QE). The estimation of alkaloids was based on the reaction between alkaloids and BCG. A yellow-coloured complex with maximum absorption was formed. This complex was fully extractable with chloroform at pH 4.7. A calibration curve (Figure 5.6c) was constructed for various atropine concentrations and expressed in mg of atropine equivalent (A) per gram. All results are shown in Table 5.8 with their respective wavelengths. The flavonoid content in the lemon peels was higher than that of the other phytochemicals, with a concentration of 1355 mgQE/g. Whereas, the alkaloids had the lowest content of 63 mgAE/g.

Table 5.8: Phytochemical analysis of the M. oleifera leaf extract**.**

Phytochemicals	**Wavelength (nm)**	**Content**	**Dilution factor**	**Actual content**
Phenolic content (mgTAE/g of extract)	750	138	5	690
Tannins content (mgTAE/g of extract)	725	585	-	585
Flavonoid content (mgAE/g of extract)	510	271	5	1355
Total alkaloid content (mgAE/g of extract)	470	63	-	63

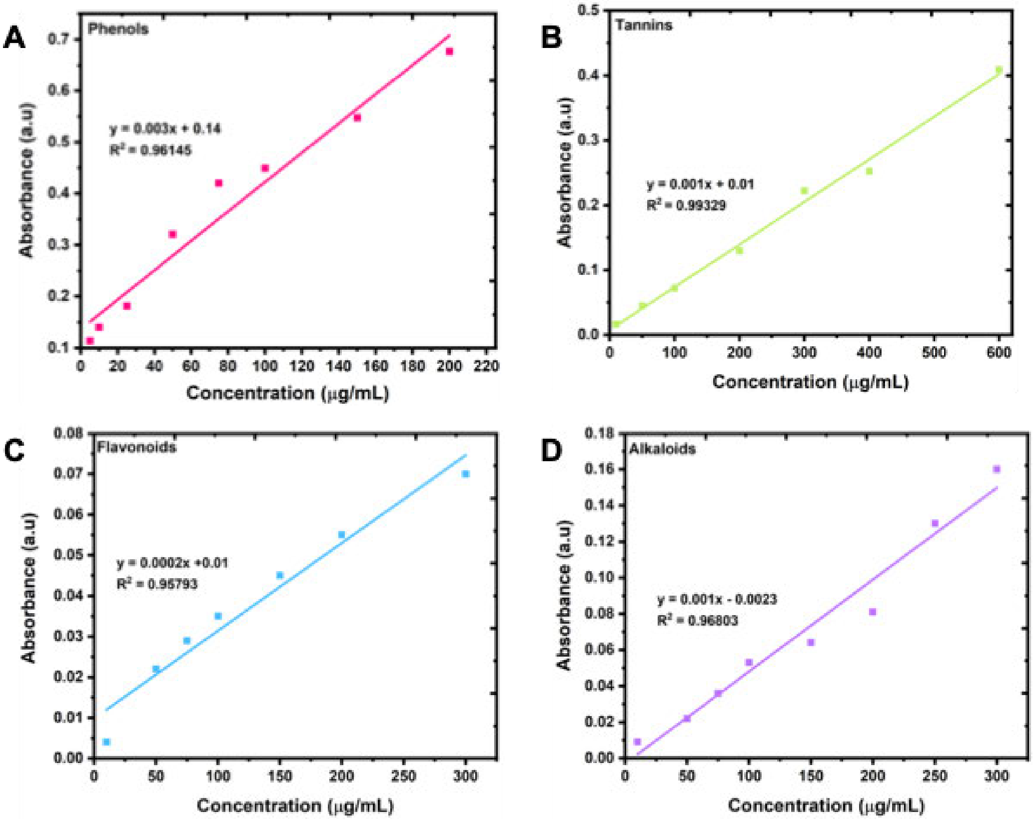

Figure 5.6: Calibration curves (**A**) Phenols, (**B**) Tannins, (**C**) Flavonoids and (**D**) Alkaloids

5.5 Chemistry of Indole-Pyrazole capped Nanoparticles

5.5.1 Synthesis and Characterisation of Cobalt Nanoparticles

Bis indole-pyrazole cobalt nanoparticles (BIP-CoNPs) and Chromone- indole-pyrazole cobalt nanoparticles (CIP-CoNPs) were successfully synthesised from lemon peel extract. The formation of a reddish-pink colour indicated the synthesis of the nanoparticles (Figure 5.7) and was preliminarily evidenced by the UV-Vis spectrum with high peak absorption spectrum at 510 nm (Figure 5.8a) with approximately 10 % difference in absorbance. The formation of such a peak occurs due to the surface plasmon resonance (SPR) of the nanoparticles. The result of the broad SPR peak clearly shows the polydispersity of the nanoparticles

(Cittrarasu *et al.* 2021). The addition of the CIP compound to CoNPs resulted in an increase in absorbance when compared to BIP-CoNPs. Similar results were reported by Huma and co-workers using orange peels (Ali, Dixit and Alarifi 2024). Kharade *et al* 2020. also reported an SPR band around 508 nm using Hibiscus cannabinus leaf extract (Kharade Suvarta *et al.* 2020).

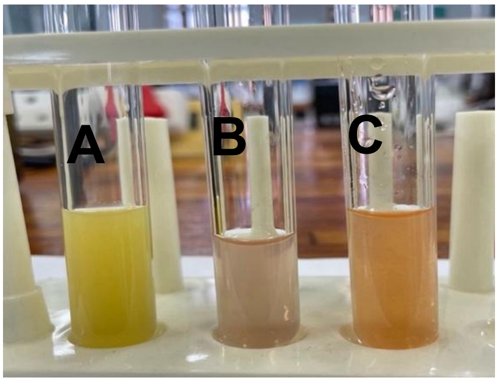

Figure 5.7: (**A**) Lemon peel extract. (**B**) Mixture of $Co(NO_3)_2{\cdot}6H_2O$ and lemon peel extract. (**C**) CoNPs

The FTIR spectrum is shown in Figure 5.8b, provided information about the functional groups involved in the reduction of cobalt ions and detects some possible biomolecules capped on the nanoparticles for both BIP-CoNPs and CIP-CoNPs. At 3306 & 3309 cm^{-1} the peaks could be attributed to the N-H stretching of amines, likely from the indole and pyrazole ring present in BIP and CIP structures. The peaks found at 2918 cm^{-1} correspond to C-H stretching vibrations, might be attributed by the presence of tannins in the lemon extract. The peaks at 1744 &1740 cm^{-1} are tributed to the C=O stretching vibrations in carbonyl groups which might be due to presence of flavonoids. The medium peaks at 1571 & 1569 cm^{-1} are attributed to N-H bending. At 1367 & 1364 the peaks are attributed to C-N stretching could be due to indole-pyrazole derivatives. Another peaks found at

1010 and 1051 cm^{-1} are attributed to C-O stretching. The results reveal that, lemon peel extract and indole-pyrazole derivatives were involved in reducing and capping cobalt nanoparticles. The results also correlated with the findings from the literature on the CoNPs synthesised from orange peel extract, which had prominent peaks of C-H, N-H and C-O (Anupong *et al.* 2023). Khadhim *et al.,* reported that significant predominant peaks N-H, and C-O correspond to various forms of phenols and other compounds that were involved in the reduction and capping of CoNPs produced by the aqueous extract of *Monocarps* erectus L (Khadhim and Kadhim 2021).

Surface imaging with elemental composition analysis was confirmed by SEM-EDS mapping analysis. The SEM images in Figure 5.8c (BIP-CoNPs) and Figure 5.8d (CIP-CoNPs) show distinct, predominantly spherical nanoparticles, along with some larger aggregates. The particle size distribution histograms in Figure 5.8e and 5.8f were calculated using ten TEM images for each sample and images used for this analysis are included in Appendix 16. The nanoparticles exhibited sizes ranging between 30 to 70 nm. The surface of synthesised nanoparticles was capped by secondary metabolites of lemon peel extract, which was responsible for this aggregation (Zaib *et al.* 2020). Similar SEM images were observed in literature for cobalt nanoparticles synthesised employing plant extract (Ahmed, Tariq and Mudassir 2021; Khadhim and Kadhim 2021; Vinayagam *et al.* 2023; Ali, Dixit and Alarifi 2024). Figure 10e and 10f shows the element quantitative and qualitative analysis may involve the formation of BIP-CoNPs and CIP-CoNPs; respectively. The analysis of EDS for revealed BIP-

CoNPs (Figure 5.8g) multiple peaks, which were oxygen (24.89 %), carbon (53.78 %), and cobalt (21.32 %).

Figure 5.8h shows the EDS spectrum of CIP-CoNPs, with carbon (25.63 %), oxygen (53.11 %), cobalt (18.39%), sodium (1.18 %), and sulphur (1.79 %) being the major elements present. The three characteristic cobalt peaks at 0.5, 7.0, and 7.6 keV, which correspond to the Lα, Kα, and Kβ transitions; respectively. Confirms the successful integration of cobalt into the synthesised nanoparticles. The unique Kα and Kβ peaks authenticate the elemental identity and reduce interference from other elements. These findings are consistent with the expected composition of cobalt nanoparticles generated with plant extract (Khadhim and Kadhim 2021; Ma *et al.* 2023; Yuan *et al.* 2023; Ali, Dixit and Alarifi 2024). The presence of carbon and oxygen absorption peaks resulted from the phytochemical moiety of lemon peel extract and sulphur from chromone derivative (Kharade Suvarta *et al.* 2020).

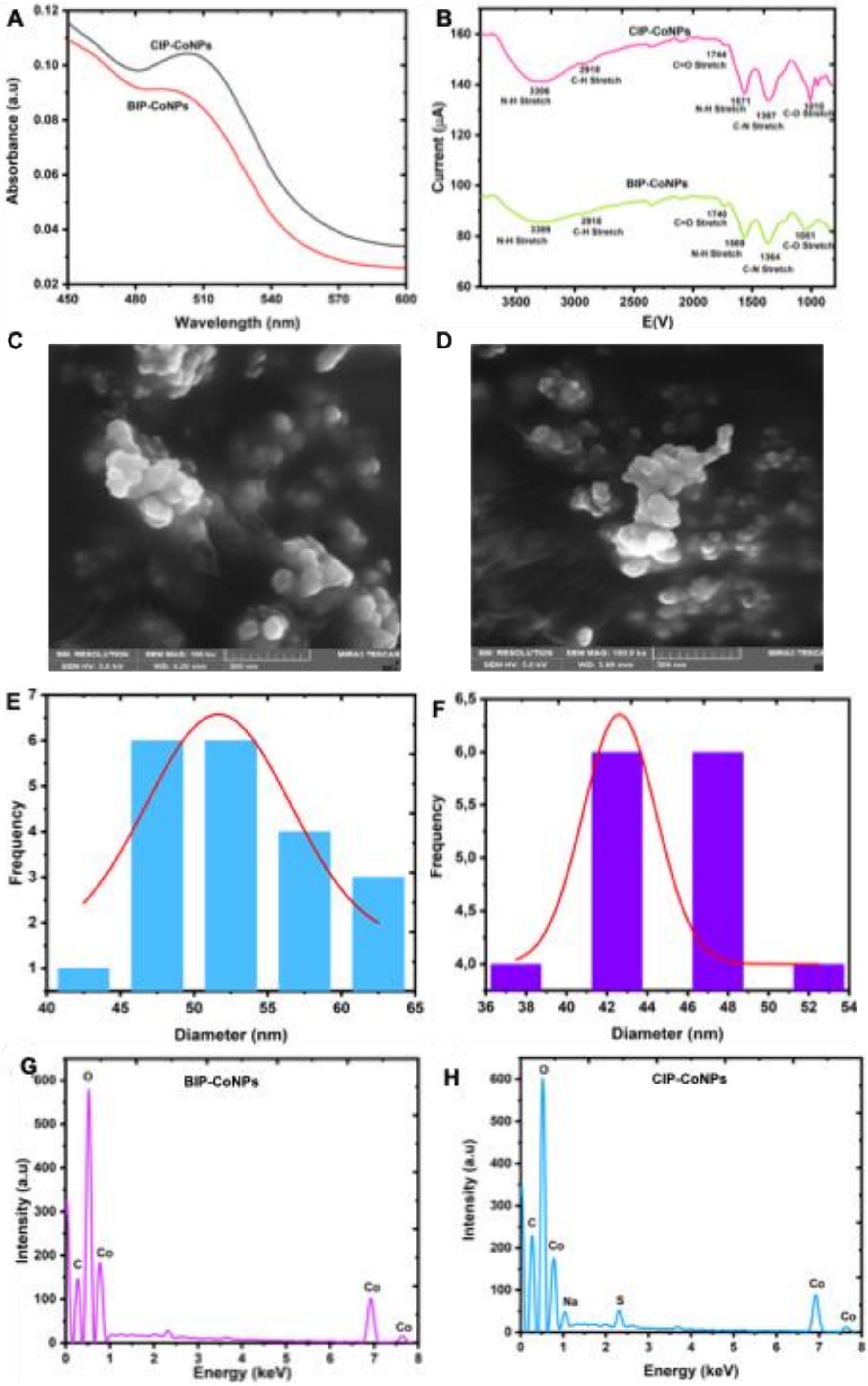

Figure 5.8: Spectra of BIP-CoNPs and CIP-CoNPs (**A**) UV-Vis and (**B**) FTIR. SEM images of (**C**) BIP-CoNPs and (**D**) CIP-CoNPs. Histogram prepared by image j software of (**E**) BIP-CoNPs and (**F**) CIP-CoNPs. EDS spectra of (**G**) BIP-CoNPs and (**H**) CIP-CoNPs.

5.5.2 Synthesis and Characterisation of Gold Nanoparticles

AuNPs formation was monitored visually and by UV-vis spectroscopy. The lemon peel extract was added into the aqueous solution of $HAuCl_4$. After 20 minutes, the colour of the solution started changing from yellow to dark violet, which was due to the reduction of Au^{3+} to Au^0 (Al-Radadi 2021) (Figure 5.9). In UV-vis spectroscopy, the light source generates excitation at a specific wavelength. Resulting in a distinct peak known as surface plasmonic resonance (SPR) (Hosny *et al.* 2021) and it is a fundamental technique for obtaining SPR of prepared metal nanoparticles (Al-Radadi 2021). The SPR peak in metallic nanoparticles' absorption spectrum is one of their most distinguishing features and the morphology of nanoparticles defines the form and location of the SPR peak (Hosny *et al.* 2021). During the reduction reaction $HAuCl_4$ ions converted to Au ions using lemon peel extract and are easily observed under UV-Vis spectroscopy. The synthesised AuNPs (BIP-AuNPs and CIP-AuNPs) gave a strong SPR peak at 544 nm wavelength (Figure 5.10a) indicating the successful synthesis (Hosny *et al.* 2021; Li *et al.* 2021; Pechyen *et al.* 2021) .

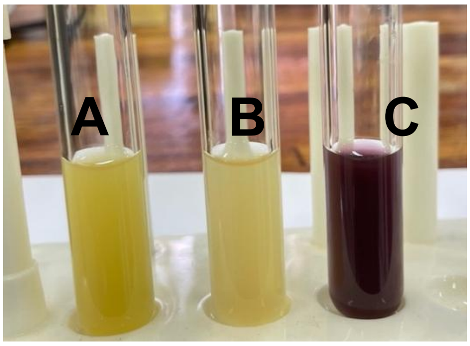

Figure 5.9: (**A**) Lemon peel extract. (**B**) Mixture of $HAuCl_4$ and lemon peel extract. (**C**) AuNPs.

The identification of functional groups likely contributing to the reduction and stabilisation of synthesised CIP-AuNPs was carried out using FTIR spectroscopy. For the FTIR spectra of CIP-AuNPs and BIP-AuNPs (Figure 5.10b), the main bands observed were O-H stretching at 3309 cm^{-1}, which might be due to the phenolic acids, flavonoids, and alcohols present in the lemon peel extract. C=C (1632 & 1636 cm^{-1}) stretching from flavonoids or aromatic systems in the extract or IP derivative. C-N (1222 & 1218 cm-1) stretching may be due to aliphatic or aromatic amines, which may relate to the indole-pyrazole moiety. And lastly, the C-O stretching at 1010 cm^{-1} and 1013 cm^{-1} in primary or secondary alcohols and ethers.

To examine the size and shape of the AuNPs, both SEM and TEM analyses were performed. Figure 5.10ac and Figure 5.10d show the SEM images, where the AuNPs appear predominantly spherical and uniformly distributed. For more accurate particle size analysis, TEM imaging was also conducted and used to calculate the size distribution using ImageJ software. The resulting histograms are presented in Figure 5.10e and Figure 5.10f. The TEM images used for this analysis are included in Appendix 16. EDS surface scanning analysis was performed, and the EDS spectra confirm the primary composition of Au, S, Na, O, and C elements in BIP-AuNPs (Figure 5.10g) and CIP-AuNPs (Figure 5.10h). The optical signals at 1.6, 2.1, 9.7, and 11.4 keV confirm the AuNPs (Rey-Méndez, Rodríguez-Argüelles and González-Ballesteros 2022; Shirzadi-Ahodashti *et al.* 2023; Nobahar *et al.* 2024). The presence of sodium, carbon, and oxygen absorption peaks resulted from the phytochemical moiety of lemon peel extract (Kharade Suvarta *et al.* 2020), sulphur might be due from indole-pyrazole derivatives.

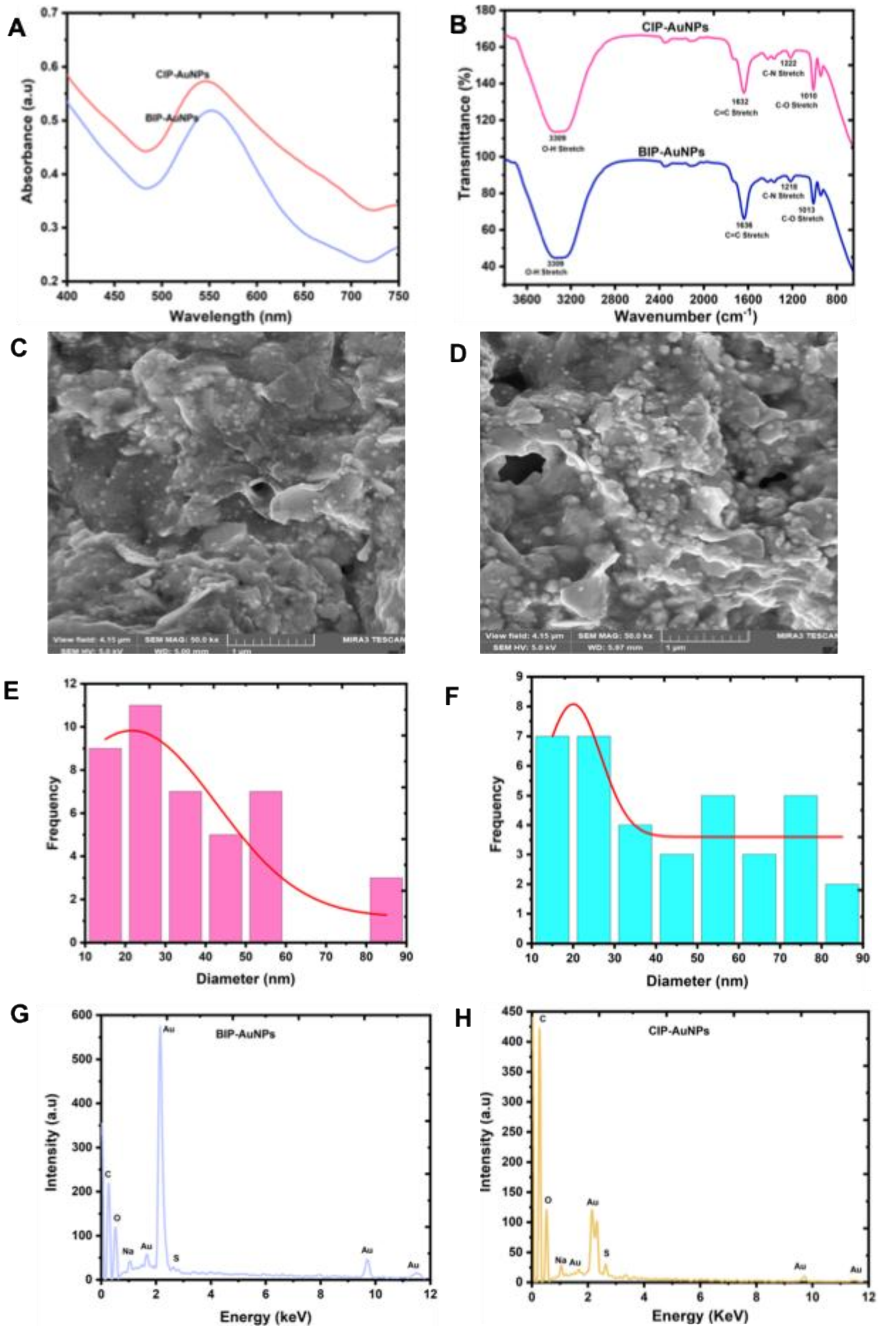

Figure 5.10: Spectra of BIP-AuNPs and CIP-AuNPs (**A**) UV-Vis and (**B**) FTIR. SEM images of (**C**) BIP-AuNPs and (**D**) CIP-AuNPs. Histogram prepared by image j software of (**E**) BIP-AuNPs and (**F**) CIP-AuNPs. EDS spectra of (**G**) BIP-AuNPs and (**H**) CIP-AuNPs.

5.6 Summary

The environmentally friendly synthesis of cobalt and gold nanoparticles using lemon peel extract was explored. The nanoparticles were further modified by incorporating the indole-pyrazole derivatives (**4a** and **4b**). Phytochemical analysis confirmed the presence of phenols, flavonoids, tannins, and alkaloids within the extract, with flavonoids identified as the predominant component. Successful synthesis of CoNPs was evident from the colour change to reddish-pink and a UV-Vis absorption peak at 510 nm. FTIR spectra confirmed that plant-based compounds helped in both reducing and capping the nanoparticles. SEM images revealed a mix of spherical nanoparticles, while EDS analysis confirmed cobalt as the main element, along with traces of carbon, oxygen, sodium, and sulphur. AuNPs were synthesised in a similar manner, with the solution changing from yellow to dark violet, indicating the reduction of gold ions. The UV-Vis spectrum displayed a characteristic peak at 544 nm. FTIR analysis identified similar functional groups to those found in CoNPs. SEM images showed mostly spherical nanoparticles and EDS confirmed the presence of gold along with other plant-derived elements.

Part C: Electrochemical Immunosensors

This section presents the results of the developed electrochemical immunosensors for the detection of insulin antibodies. The sensors were fabricated using cobalt and gold nanoparticles capped with the indole-pyrazole derivatives **4a** (bis indole-pyrazole) and **4b** (chromone indole-pyrazole), and their performance in antibody detection was evaluated.

5.7 Cobalt Nanoparticles-based Immunosensors

5.7.1 Electrochemical characterisation

The conductivity of the substrate material influences the sensitivity of the electrochemical immunosensor (Zhao *et al.* 2021a). CV and EIS were applied to monitor the efficiency of the immobilisation process of the electrochemical immunosensor. The electrochemical immunosensor modified with CIP-CoNPs was selected as a template to discuss the layer by layer modification. The results obtained for the CV using the redox signal of 5 mM hexacyanoferrate $Fe(CN)_6]^{3/4}$ are shown in Figure 5.11a. A well-defined sharp redox peak for the reduction of $Fe(CN)_6]^{3/4}$ was obtained at the bare platinum electrode (curve i, I_{pa} = 4.33 μA). By modifying the bare PtE with CIP-CoNPs, the peak current increase (curve ii, I_{pa} = 5.41 μA) is due to the nanomaterial having a large specific surface area and more electroactive sites, which is the case with CoNPs the case is provide high capacity, electrical conductivity and excellent catalytic ability (Lü *et al.* 2022; Long *et al.* 2024). However, when recombinant insulin protein (antigen) was adsorbed on CIP-CoNPs/PtE, the current decreased (curve iii, I_{pa} = 5.22 μA), due to the successful immobilisation because the protein molecules inhibit electron transfer (Maleki *et al.* 2023).

The current continued to decrease after the dropping of BSA (curve iv, I_{pa} = 4.87 μA) on Anti/CIP-CoNPs/PtE. Having observed the electrochemical characteristics through CV. It was rational to evaluate conductivity of electrodes and electrode materials by EIS, which is a highly sensitive characterisation technique (Rahmati *et al.* 2021; Anusha *et al.* 2022). Figure 5.11b shows the prototype Nyquist plots of pure PtE, CIP-CoNPs/PtE, anti/CIP-CoNPs/PtE, and BSA/anti/CIP-CoNPs/PtE using 5 mM $[Fe(CN)_6]^{3/4}$. The Nyquist diagram consist of two parts: the linear component at lower frequencies represents the electron diffusion process and the semi-circular section at higher frequencies, which is part of the charge transfer resistance (R_{ct}), represents the electron transfer process (Rahmati *et al.* 2021). The R_{ct} values are obtained by simulation according to the equivalent circuit (Figure 5.11c), and the corresponding R_{et} values are shown in Table 5.9. In comparison to the semicircle diameter of bare PtE (curve ii), which exhibits a R_{ct} of 16.85 kΩ, the semicircle diameter of CIP-CoNPs modified PtE (curve ii) is reduced.

The remarkable conductivity of CIP-CoNPs contributes to an enhanced rate of electron transfer, proven by a R_{ct} of 12.76 kΩ. The diameter of the semicircle progressively expanded as the antigen (curve iii) and BSA (curve iv) were immobilised in layers on the CIP-CoNPs/PtE, exhibiting R_{ct} values of 12.86 and 13.58 kΩ; respectively. Since, proteins are biological macromolecular materials with high resistance. This has an impact on the electron transfer rate of PtE (Zhao *et al.* 2021a). Both techniques yielded consistent results, indicating the successful preparation of the immunosensor. The electrochemical immunosensor enhanced with BIP-CoNPs exhibited comparable behaviour; the findings are presented in Appendix 14. Following the electrochemical characterisation, the sensors employing CV were compared to determine which derivative yields better outcomes (Figure 5.11d). The immunosensor modified with CIP-CoNPs produced the maximum anodic current. Chromones, a class of benzopyran derivatives, demonstrate significant electrochemical properties. Owing to their conjugated structures and electron-rich oxygen functions (Mucha *et al.* 2019). Additionally, the carbonyl group also experiences reduction, which is affected by substituents on the chromone ring. Electron-donating or electron-withdrawing groups modify the reduction potential (Kurma *et al.* 2023).

Table 5.9: Summary of Equivalent circuit Parameters from Impedance Spectra in 5 mM $[Fe\ (CN)_6]^{3-/-4}$

Electrode	R_s(kΩ)	R_{ct} (kΩ)	χ^2
(i): PtE	0.194	16.85	0.130
(ii): CIP-CoNPs/PtE	0.142	8.76	0.098
(iii): Anti/CIP-CoPNs/PtE	0.168	12.86	0.092
(iv): BSA/Anti/CIP-CoPNs/PtE	0.170	13.58	0.094
(ii): BIP-CoNPs/PtE	0.218	8.87	0.213
(iii): Anti/BIP-CoPNs/PtE	0.167	10.50	0.121
(iv): BSA/Anti/BIP-CoNPs/PtE	0.146	15.30	0.117

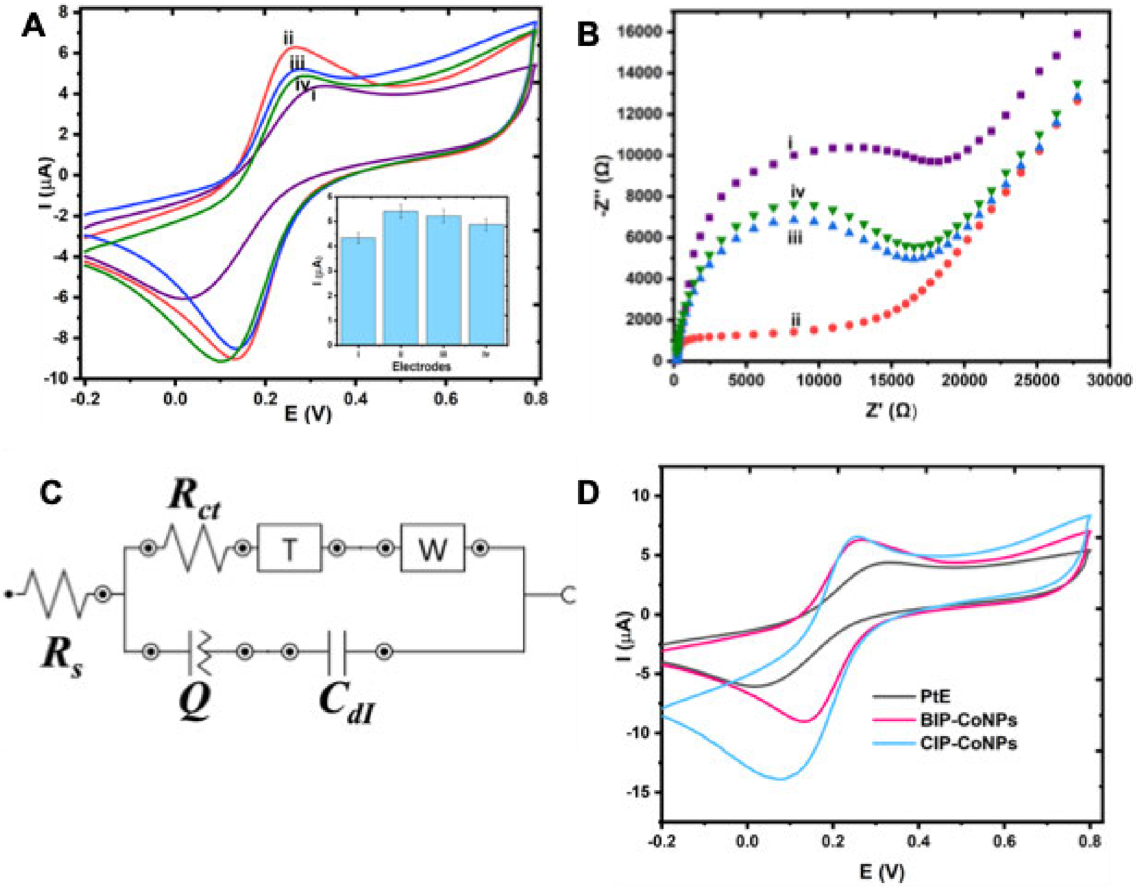

Figure 5.11: (**A**) Cyclic voltammograms and (**B**) Nyquist plots obtained for bare and modified electrodes in 5 mM $[\mathrm{Fe}\ (\mathrm{CN})_6]^{-3/-4}$ solution prepared in 0.1 M phosphate buffer.(i) Bare PtE, (ii) CIP-CoNPs/PtE, (iii) Anti/CIP-CoNPs/PtE and BSA/Anti/CIP-CoNPs/PtE (**C**) Equivalent circuits used in fitting EIS data for the bare and modified electrodes for BSA/anti/CIP-CoNPs/PtE and (**D**) Cyclic voltammograms of bare PtE, BSA/anti/CIP-CoNPs/PtE and BSA/anti/CIP-CoNPs/PtE.

5.7.2 Optimisation of experimental conditions

The optimal conditions for electrochemical sensor construction have a significant influence on sensor sensitivity (Asadpour *et al.* 2021). To obtain the best current signal, several experimental parameters were optimised using the CV technique in 5 mM $[\mathrm{Fe}\ (\mathrm{CN})_6]^{3\text{-}/4\text{-},}$ which includes pH of the phosphate buffer, scan rate, antigen incubation temperature, concentration, and antigen incubation time. The immunosensors' analytical performance under the phosphate buffer solution was evaluated in the pH levels ranging from 5 to 7.4. It was found to perform optimally at pH 6.4 as can be seen in Figure 5.12a and therefore it was used through the analysis. The effect of scan rate on the redox peak current of Fe^{2+} and Fe^{3+} was assessed using BSA/Anti/CIP-CoNPs/PtE (Figure 5.12b) and BSA/Anti/BIP-CoNPs/PtE (Figure 5.12c) at different scan rates. The anodic and cathodic peak currents showed an increase with the rise in scan rate, ranging from 10 to 100 mV s^{-1}. The linear relationship to the peak current of the CVs and the square root of the scan rate in Figure 5.12d and 5.12e. Showed that the electron transfer of the BSA/anti/CIP-CoNPs/PtE or BSA/anti/BIP-CoNPs/PtE surface was diffusion controlled (Gao *et al.* 2019; Maleki *et al.* 2023) and the optimal scan rate was 100 mV s^{-1}.

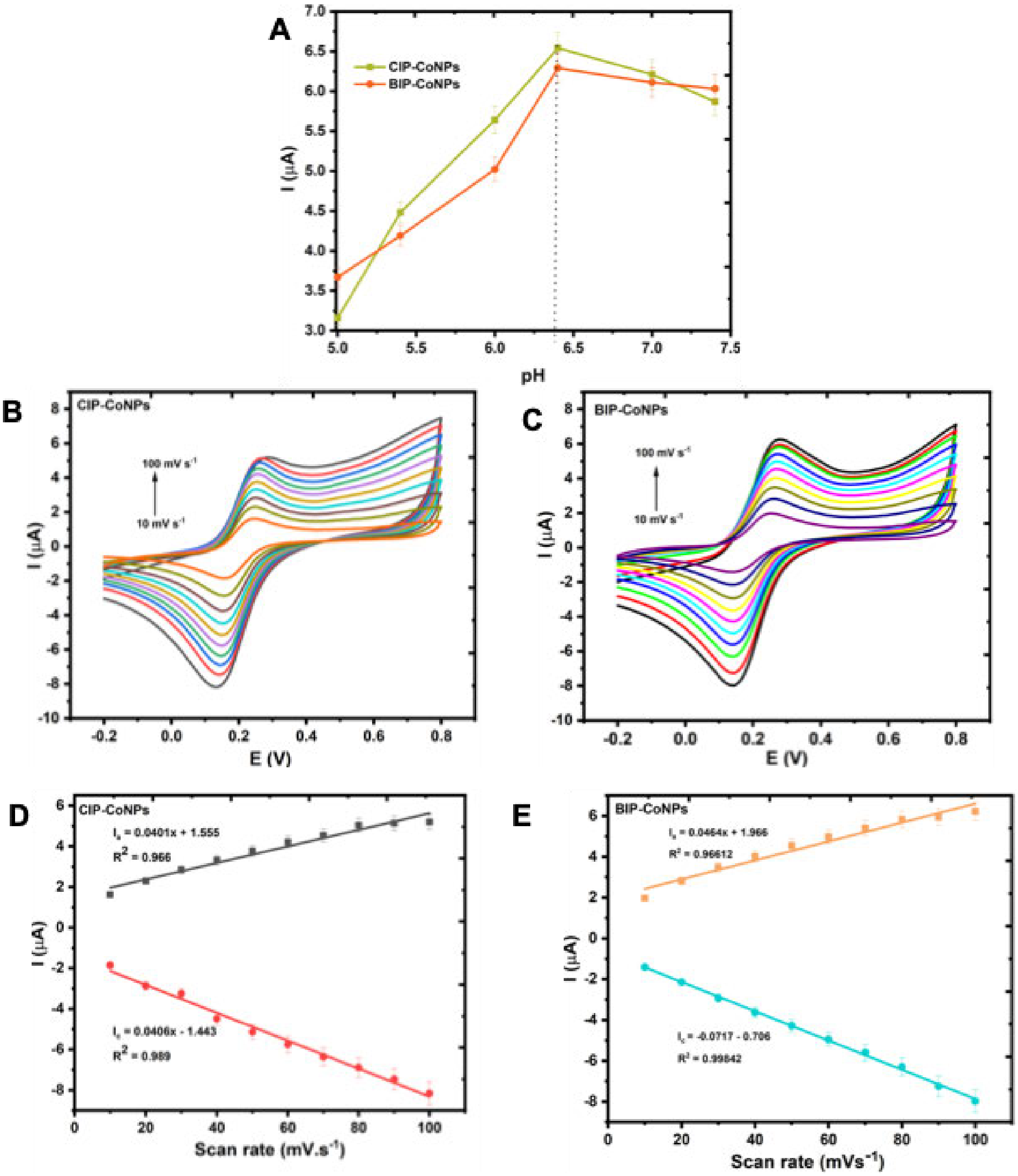

Figure 5.12: (**A**)Plot of phosphate buffer pH levels vs anodic current and a corresponding insert of CVs of modified immunosensors at different pH levels (**B**) CVs of modified BSA/anti/CIP-CoNPs/PtE in [Fe (CN)$_6$]$^{3/4}$ (5 mM) at different scan rates. (**C**) CVs of modified BSA/anti/BIP-CoNPs/PtE in [Fe (CN)$_6$]$^{3/4}$ (5 mM) at different scan rates. (**D**) The correlation between the anodic and cathodic peak currents and the square root of the scan rate (5 mM [Fe (CN)$_6$]$^{3/4}$) of BSA/anti/CIP-CoNPs/PtE peak currents (**E**) The correlation between the anodic and cathodic peak currents and the square root of the scan rate (5 mM [Fe (CN)$_6$]$^{3/4}$) of BSA/anti/BIP-CoNPs/PtE peak currents.

Volumes of insulin antigen (50 μg.mL^{-1}) ranging from 1 μL to 7 μL were tested to determine the optimal volume for immobilising the insulin antigen and achieving maximum detection efficiency. The peak anodic current initially increased as the amount of insulin antigen grew, but once the volume reached 4 μL, the current value plateaued and reached its maximum, as shown in Figure 5.13a. Increasing the insulin antigen volume beyond 4 μL led to saturation of the electrode platform with biological components, which obstructed electron flow through the nanocomposite medium (Farrokhnia *et al.* 2022). Therefore, 4 μL was chosen as the immobilisation volume of the insulin antigen in the subsequent immunosensor.

The incubation time for insulin antigen immobilisation directly affects the performance of the electrochemical immunosensor. This was investigated using an immunosensor prepared with the immobilisation of 4 μL of insulin antigen and varying incubation times (20 to 160 minutes). Figure 5.13b shows that the anodic currents increased linearly as the incubation time increased from 20 to 160 minutes. Thereafter, decreased with time as an indication of saturated immunocomplex formation on the electrode platform (Farrokhnia *et al.* 2022). An incubation time of 120 minutes was chosen for the immobilisation time. Lastly, the influence of temperature on the immobilisation of the insulin antigen was examined at different temperatures (4, 25, and 37 °C). To determine the optimal immobilisation temperature for the insulin antigen. Optimal immobilisation temperatures were found to be 25 °C and 37 °C (Figure 5.13c). However, 37 °C was chosen as the best optimal temperature.

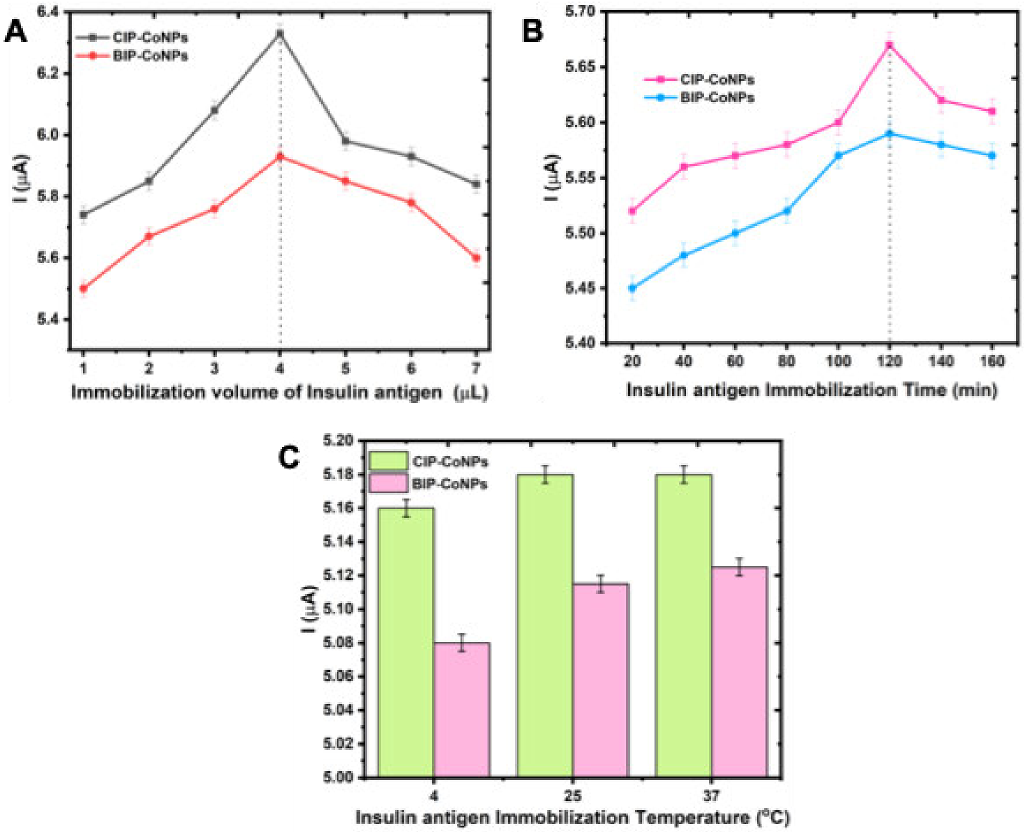

Figure 5.13: (**A**) Plot of immobilisation volumes of the antigens vs anodic current and a corresponding insert of CVs of modified immunosensors at different volumes. (**B**) Plot of immobilisation time vs anodic current and a corresponding insert of CVs of modified immunosensors at different times. (**C**) Histogram of the immobilisation temperatures effect.

5.7.3 Analytical performance

The proposed immunosensors were used to detect various concentrations of insulin antibodies using the SWV method under optimal conditions to test its analytical performance. The detection was carried out in a phosphate buffer with a pH of 6.4, containing 5.0 mM of [Fe(CN)$_6$]$^{3-/4-}$ and the results are shown in Figure 5.14a and 5.14b. The electrocatalytic current of the immunosensors increased with the rise in insulin antibody concentration. This increase in current can be attributed to the enhanced adsorption of insulin antibodies onto the insulin antigens. Forming antigen-antibody complexes that promote a specific spatial arrangement, that creates spatial channels to facilitate the transfer of electrons from the probe electrolyte to the modified electrode. Thereby, improving the flow of electrons to the platinum electrode substrate (Farrokhnia *et al.* 2022). Additionally, the presence of CIP-CoNPs or BIP-CoNPs on the electrode's surface can contribute to the overall current observed during the electrochemical measurement. This is because cobalt nanoparticles can facilitate a high rate of electron transfer and provide a large number of active sites. Increasing the amount of immobilised antigen and improves the efficiency of antibody-antigen binding, as well as the surface area (Maleki *et al.* 2023).

The immunosensors' calibration curve show a linear correlation between peak current and log of insulin antibody concentration. For CIP-CoNPs, the R^2 value is 0.994, and the linear regression equation is $I = 5.6x + 132$ (Figure 5.14c). For BIP-CoNPs, the R^2 value is 0.978, and the linear regression equation is $I = 2.19x + 150$ (Figure 5.14d). The error bars on the curves represented the mean values derived from three measurements, specifically indicating the standard error at each data point. The proposed immunosensors had low limit of detection (LOD) and high sensitivity. For CIP-CoNPs, the LOD is 0.054 ng/mL, with a sensitivity of 5.60 μA/ng/mL, and for BIP-CoNPs, the LOD is 0.137 ng/mL, with a sensitivity of 2.19 μA/ng/mL. Table 5.10 shows that both sensors demonstrated better performance in the detection of insulin antibodies when contrasted with some of the electrochemical biosensors that have been previously reported. However, the CIP-CoNPs immunosensor had a LOD and higher sensitivity. This makes it better suited for applications requiring precise, sensitive insulin antibodies detection, especially at low concentrations.

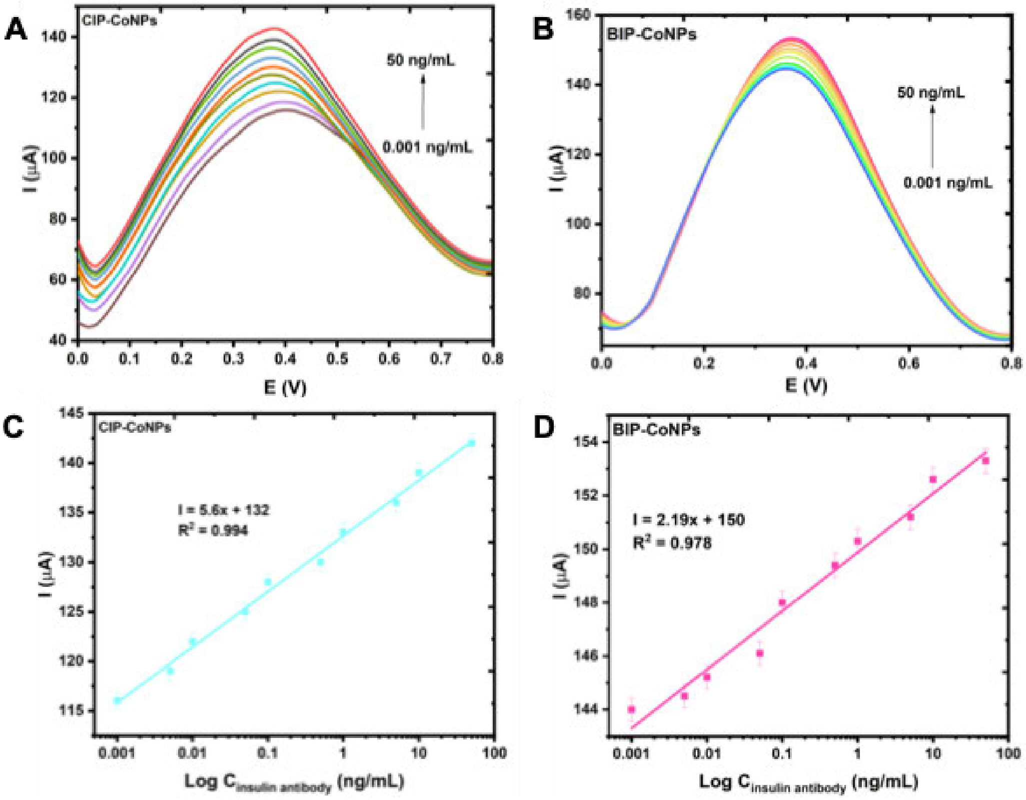

Figure 5.14: SWVs of the designed immunosensor in different insulin antibody concentrations (0.001−50 ng/mL) in a phosphate buffer containing 5.0 mM [Fe(CN)6]$^{3-/4-}$ (**A**) BSA/anti/CIP-CoNPs/PtE and (**B**) BSA/anti/BIP-CoNPs/PtE. The linear dependency between the peak current versus the logarithm concentration of insulin antibody (**C**) BSA/anti/CIP-CoNPs/PtE. and (**D**) BSA/anti/BIP-CoNPs/PtE.

Table 5.10: Recently developed electrochemical biosensor research work for sensitive determination of insulin.

Electrochemical technique	Modifier	Linear range	LOD (ng/mL)	Reference
Voltammetric	Polypyrrole & Nickel Nanoparticles	500 nM - 5 μM	38.00 nM	(Šišoláková *et al.* 2023)
Voltammetric	Nickel Nanoparticles	600 nM -10 μM	19.60 nM	(Shepa *et al.* 2021)
Voltammetric	Copper nanoparticles	0.05 μM - 5 μM	25.00 nM	(Šišoláková *et al.* 2020)
Voltammetric	Silver Nanoparticles-Graphene Quantum Dots	10 μM - 120 μM	1.10 nM	(Wang, Liu and Hua 2021)
Voltammetric	Mesoporous Silica Nanoparticles Thin-Film	10 nM - 350 nM	3.00 nM	(Asadpour *et al.* 2021)
Voltammetric	-	10 nM -1 μM	3.30 nM	(Zhou *et al.* 2024)
Voltammetric	Silver Nanoparticles	0 - 225 nM	2.00 nM	(Bhardwaj *et al.* 2023)
Voltammetric	CIP-CoNPs	0.001 nM - 50 nM	0.05 nM	**This work**
Voltammetric	BIP-CoNPs	0.001 nM - 50 nM	0.14 nM	**This work**
Voltammetric	CIP-AuNPs	0.001 nM - 50 nM	0.99 nM	**This work**
Voltammetric	BIP-AuNPs	0.001 nM - 50 nM	1.00 nM	**This work**

5.7.4 Selectivity, reproducibility and repeatability

To ensure optimal performance and reliable results, it is important for the sensor to exhibit exceptional selectivity, reproducibility, and repeatability. Therefore, all three factors using the SWV method were effectively evaluated. Selectivity was assessed by detecting common interferences in human serum at standard concentrations. These included 7.25 μM human serum albumin (HSA), 3.0 μM ascorbic acid (AA), 6.0 mM glucose (GL), 0.50 mM uric acid (UA), and 0.50 μM dopamine (DP). All interferences had a significantly lower current response than the insulin antibody (anti). Moreover, the current responses of these interferences mixed with Anti were not significantly different from those of Anti alone (Figure 5.15a). The results demonstrate the sensor's selectiveness for Anti. Wardani and co-workers reported comparable results when they employed an electrochemical sensor modified with multiwalled carbon nanotubes and a cryogel made of a molecularly imprinted polymer (Wardani *et al.* 2023).

One of the key factors in assessing a sensor's precision is its excellent reproducibility. Six replicative modified immunosensors for each sensor detecting insulin antibody (5 ng/mL) under the same conditions in a phosphate buffer (pH 6.4) containing 5.0 mM of $[Fe(CN)_6]^{3-/4-}$ were investigated. The designed immunosensors displayed good precision, with a relative standard deviation (RSD) of 1.47 % (CIP-CoNPs) and 0.86 % (BIP-CoNPs). The results are displayed in Figure 5.15b and 5.15c; respectively. The immunosensor utilising BIP-CoNPs exhibited the highest precision in terms of its RSD. Repeatability was also validated by detecting 5 ng/mL of antibody concentration 50 times with the same immunosensor. Figure 5.15d clearly displayed that, for BSA/anti/CIP-CoNPs/PtE, there was no considerable change between the first and the 25th cycle, but from the 25th to the 50th cycle. There was a decrease in current, and for BSA/anti/BIP-CoNPs/PtE, there was no considerable change between the first and the 15th cycle. Based on achieved results, both immunosensors have a considerable intra-day stability level (Shepa *et al.* 2021). However, BSA/anti/CIP-CoNPs/PtE is more considerable.

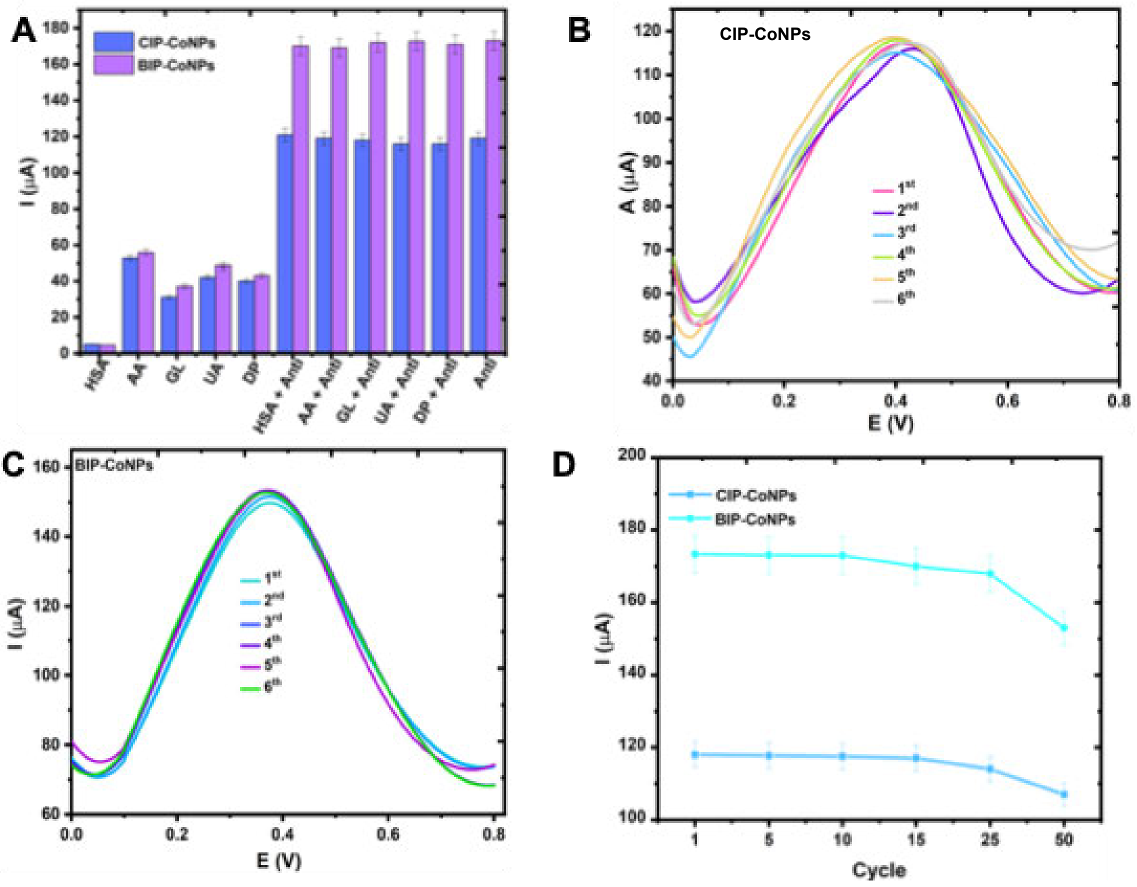

Figure 5.15: (**A**) Histograms of the responses regarding the selectivity investigations of the immunosensors. SWVs of reproducibility response of 5 ng/mL of insulin antibody to 6 different immunosensors under similar conditions (**B**) BSA/anti/CIP-CoNPs/PtE and (**C**) BSA/anti/BIP-CoNPs/PtE. (**D**) Line graph regarding the repeatability investigations.

5.7.5 Recovery studies

We tested insulin antibodies and the immunosensor's practicality using synthetic human serum. We made the synthetic serum (Basiaga *et al.* 2014; Calabria *et al.* 2023; Zhang *et al.* 2024) by mixing phosphate-buffered saline (PBS) (pH = 7.4), 4 % BSA, and 0.1 ng/mL immunoglobulins (IgG) to imitate insulin's protein environment. To simulate normal blood glucose, we added 0.8 mg/mL D-glucose. To simulate lipid content, we added 0.1 ng/mL cholesterol and adjusted the pH to 7.4. SWV was used to quantify synthetic serum spiked with 0.5, 1, and 5 ng/mL insulin antibodies. Table 5.11 reveals a recovery range of 93.4 % - 101.3 % and an RSD of 1.1 9% - 5.39 %. These numbers indicate that the immunosensors demonstrates excellent precision and acceptable accuracy. For detecting the insulin antibody, and their dependability makes them ideal for routine analysis.

Table 5.11: Recovery results of Insulin antibodies detection in synthetic serum sample using fabricated CoNPs immunosensors.

Sample	**Added insulin antibody concertation (ng/mL)**	**Detected value (ng/mL)**	**Recovery (%)**	**RSD %**	**Standard Error**
CIP-CoNPs					
1	0.5	0.493	98.70	1.19	0.88
2	1.0	0.988	98.90	2.45	1.86
3	5.0	5.065	101.30	2.34	1.86
BIP-CoNPs					
1	0.5	0.467	93.40	5.39	2.91
2	1.0	0.893	89.30	1.71	0.88
3	5.0	4.750	95.00	2.19	2.56

n=3

5.8 Gold Nanoparticles-based Immunosensors

5.8.1 Electrochemical characterisation

Using a redox probe consisting of 5 mM $[Fe(CN)_6]^{3-/4-}$in a phosphate buffer at pH 7.4, The EIS and CV techniques were employed to demonstrate the systematic construction approach of the proposed immunosensors. The template chosen to discuss the layer-by-layer alteration was the electrochemical immunosensor modified with BIP-AuNPs. One was selected as the immunosensor modified with CIP-AuNPs (Appendix 15) showed comparable performance. The CV response EIS spectra in Figures 5.16a and 5.16b; respectively show the progressive construction of the immunosensor. The anodic peak current of the bare PtE was 4.25 μA (curve i) and After BIP-AuNPs modification, the peak current of BIP-AuNPs/PtE increased (curve a; I_{pa} = 5.1 μA). AuNPs can enhance electron transfer between electrode substrates and electroactive species, potentially increasing the immunosensor's sensitivity while improving the electrode's effective surface area. (Tajik, Beitollahi and Torkzadeh-Mahani 2022; Nanda *et al.* 2024). After Anti modification, Anti/BIP-AuNPs/PtE (curve c) peak current was reduced to 4.55 μA and a further reduction to 4.46 μA occurred when BSA (curve iv) was added to prevent nonspecific binding on the active electrode surface. Because the protein molecules inhibit electron transfer (Maleki *et al.* 2023) and due to this reduction both Anti and BSA were successful immobilised.

EIS (Figure 5.16b) further confirms the impedance changes during the immobilisation process. The spectroscopic curve characteristics were also used to deduce the structure of the equivalent circuit (Figure 5.16c). The impedance spectra consist of two main parts: a semicircular region representing electron transfer resistance and a linear region indicating diffusion-limited processes. Smaller, curved semicircles reflect reduced resistance, enhancing charge transfer. These semicircles in the EIS curve highlight the interface layer resistance on the electrode surface. The electron transfer of the unmodified PtE and modified PtE electrodes was examined, the results depicted in Table 5.12. The bare PtE (curve a) electrode showed an Rct value of 16.85 kΩ, and the Rct value of the AuNPs/PtE electrode (curve b) was reduced to 4.48 kΩ, implying electron transfer. When biological species were added, the Rct values went up at each stage. This showed that the redox probe was blocking the electrode surface after the AuNPs/PtE surface was changed with anti (curve c, Rct value: 8.63 kΩ) and BSA (curve d, Rct 13.40 kΩ). When comparing these two immunosensors (BIP-AuNPs and CIP-AuNPs) in terms of current, there was not much difference; however, the sensor with CIP-AuNPs had a slightly higher current (Figure 5.16d).

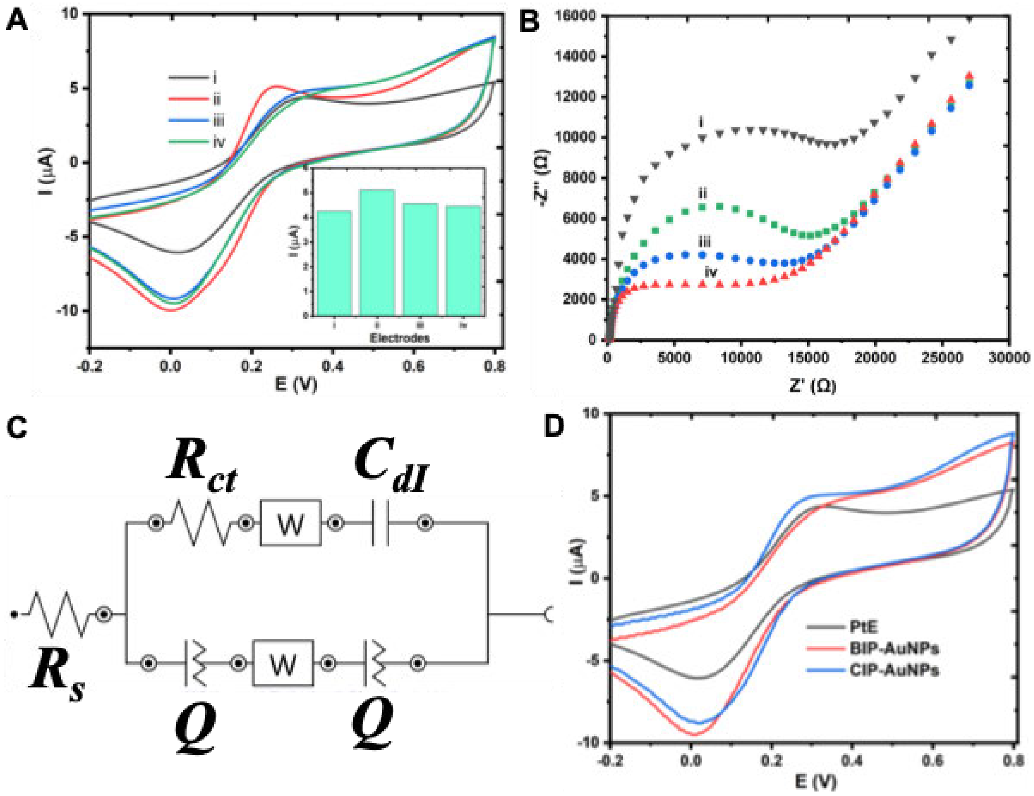

Figure 5.16: (**A**) Cyclic voltammograms and (**B**) Nyquist plots obtained for bare and modified electrodes in 5 mM $[Fe\ (CN)_6]^{-3/-4}$ solution prepared in 0.1 M phosphate buffer. .(i) Bare PtE, (ii) CIP-AuNPs/PtE, (iii) Anti/CIP-AuNPs/PtE and BSA/Anti/CIP-AuNPs/PtE. (**C**) Equivalent circuits used in fitting EIS data for the bare and modified electrodes for BSA/anti/BIP-AuNPs/PtE and (**D**) Cyclic voltammograms of bare PtE, BSA/anti/BIP-AuNPs/PtE and BSA/anti/CIP-AuNPs/PtE.

Table 5.12: Summary of Equivalent circuit Parameters from Impedance Spectra in 5 mM $[Fe\ (CN)_6]^{3-/-4}$

Electrode	**R_s(kΩ)**	**R_{ct} (kΩ)**	**χ^2**
(i): PtE	0.194	16.85	0.130
(ii): CIP-AuNPs/PtE	0.206	4.70	0.144
(iii): Anti/CIP-AuPNs/PtE - (iii)	0.155	4.80	0.099
(iv): BSA/Anti/CIP-AuPNs/PtE	0.148	5.43	0.089
(ii): BIP-AuNPs/PtE	0.177	4.48	0.161
(iii): Anti/BIP-AuPNs/PtE	0.144	8.63	0.170
(iv): BSA/Anti/BIP-AuPNs/PtE	0.160	13.40	0.174

5.8.2 Optimisation of experimental conditions

Several factors affect the development and performance of electrochemical immunosensors, with the pH of the phosphate buffer, scan rate, antigen incubation temperature, concentration, and incubation time being the most significant. To improve the efficiency of the proposed immunosensor, the experimental conditions were optimised. Among these factors, the pH of the detection solution plays a crucial role, as acidity can influence the activity of the immobilised protein (Nanda *et al.* 2024). To determine the optimal pH, the immunosensors were evaluated using CV in phosphate buffers with pH values ranging from 5.0 to 7.4.

The impact of detecting solution pH on the relative change in peak current is shown in Figure 5.17a; as the pH increases, so does the peak current. Therefore, pH 7.4 was chosen as the ideal pH for this encounter. Additionally, using the CV approach, the electrochemical scan rate investigation of the BSA/anti/BIP-AuNPs/PtE (Figure 5.17b) and BSA/anti/CIP-AuNPs/PtE (Figure 19c) immunosensors was examined at various scan rates ranging from 10 mVs^{-1} to 100 mVs^{-1}; peak currents increased with increasing scan rate. Dependence of maximal current value on scan rate for redox processes occurring at BSA/anti/BIP-AuNPs/PtE and BSA/anti/CIP-AuNPs/PtE fitted by linear function are also shown in Figures 5.17d and 5.17e, respectively.

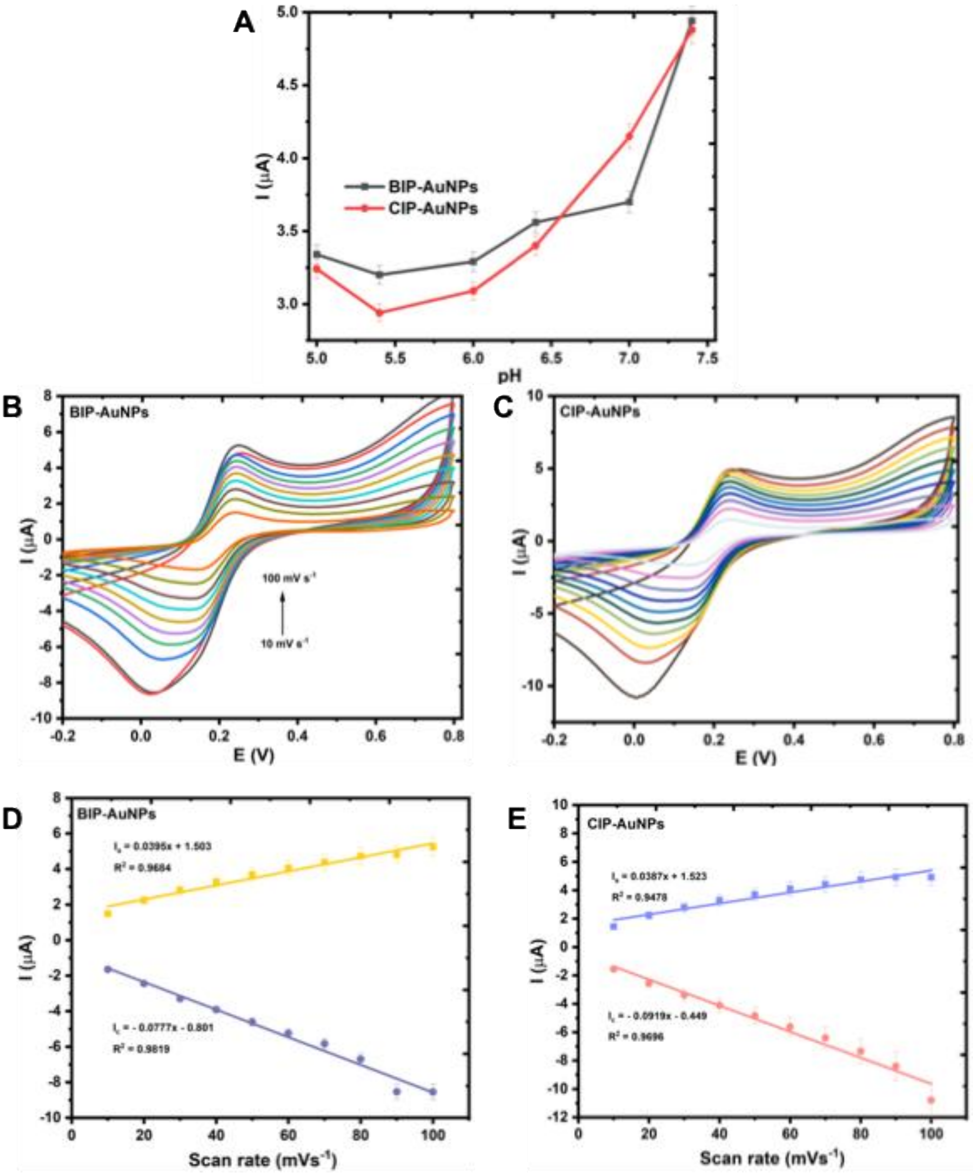

Figure 5.17: (**A**) Plot of phosphate buffer pH levels vs anodic current and a corresponding insert of CVs of modified immunosensors at different pH levels. (**B**) CVs of modified BSA/anti/BIP-AuNPs/PtE in [Fe $(CN)_6]^{3/4}$ (5 mM) at different scan rates. (**C**) CVs of modified BSA/anti/CIP-AuNPs/PtE in [Fe $(CN)_6]^{3/4}$ (5 mM) at different scan rates.(**D**) The correlation between the anodic and cathodic peak currents and the square root of the scan rate (5 mM [Fe $(CN)_6]^{3/4}$) of BSA/anti/BIP-AuNPs/PtE peak currents. (**E**) The correlation between the anodic and cathodic peak currents and the square root of the scan rate (5 mM [Fe $(CN)_6]^{3/4}$) of BSA/anti/CIP-AuNPs/PtE peak currents.

The stability and performance of the proposed immunosensors are also impacted by the amounts of immobilised antigen or antibody (Sadique *et al.* 2022). To guarantee the ideal volume of immobilised insulin antigen and attain maximal detection effectiveness, volumes of insulin antigen (50 μg.mL^{-1}) ranging from 1 μL to 7 μL were investigated. Figure 5.18a shows insulin antigen volumes and the respective peak current of CV. When the amount of insulin antigen is increased beyond 4 μL, the peak current is reduced. Therefore, based on the findings, a volume of 4 μL was determined to be the optimal volume. The antigen incubation time proved to be a key factor influencing the performance of the developed immunosensor.

The immunosensors were tested for various durations, ranging from 20 to 160 minutes (Figure 5.18b). The peak current measured by CV increased proportionally as the incubation time increased from 20 to 120 minutes, and after 120 minutes it decreased for BSA/anti/CIP-AuNPs/PtE. However, for BSA/anti/BIP-AuNPs/PtE, the peak current decreased from 20 to 100 minutes and then increased at 120 minutes. Further increasing the incubation time resulted in a decrease in the peak current. For both sensors, the ideal incubation period for the antigen on the electrode surface was 120 minutes. The effect of temperature on the efficacy of the suggested immunosensors was examined within a range of 4-37 ºC, as shown in Figure 5.18c. The maximum response current was recorded at 25 ºC, which also remained at 37 ºC. Therefore, 37 °C was selected as the ideal temperature.

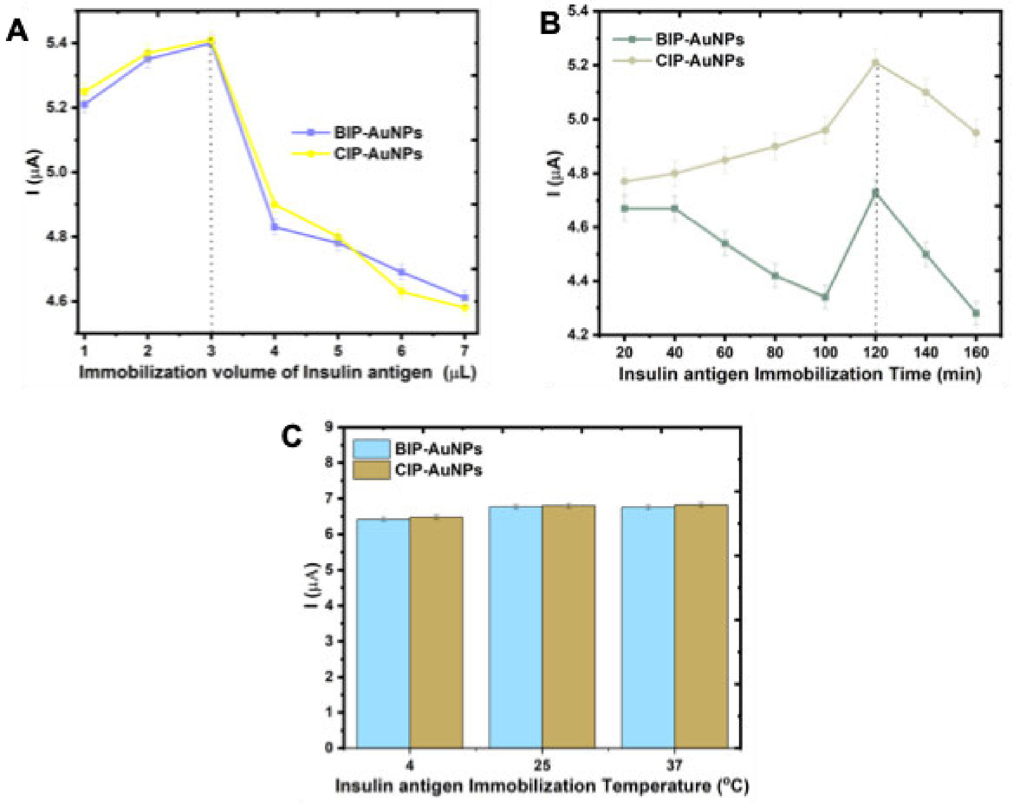

Figure 5.18: (**A**) Plot of immobilisation volumes of the antigen's vs anodic current and a corresponding insert of CVs of modified immunosensors at different volumes. (**B**) Plot of immobilisation time vs anodic current and a corresponding insert of CVs of modified immunosensors at different times. (**C**) Histogram of the immobilisation temperatures effect.

5.8.3 Analytical performance

The insulin antibody was detected at different concentrations (0.001-50 ng/mL) using SWV (Figure 5.19a and 5.19b) to confirm the performance of the produced immunosensors (BSA/anti/BIP-AuNPs/PtE and BSA/anti/CIP-AuNPs/PtE). The characteristic peak of the 5.0 mM $[Fe(CN)_6]^{3-}/^{4-}$ without the analyte was observed around 0.3 V. When the insulin antibody was added the current response was directly dependent on the concentration of the antibody. This can be attributed to an increase in electron transfer, between the negatively charged ferrocyanide redox couple and the positively charged insulin antibody attracted toward each other (Sadique *et al.* 2022). Figures 5.19c and 5.19d provides the linear relationship between the log of concentration and change in current response between 0.001 ng/mL and 50 ng/mL. The proposed immunosensors had comparable LOD and high sensitivity with those from the previously reported studies seen in Table 5.10. For BSA/anti/BIP-AuNPs/PtE, the LOD is 1.00 ng/mL, with a sensitivity of 3.70 A/ng/mL, and for BSA/anti/CIP-AuNPs/PtE, the LOD is 0.99 ng/mL, with a sensitivity of 1.42 A/ng/mL.

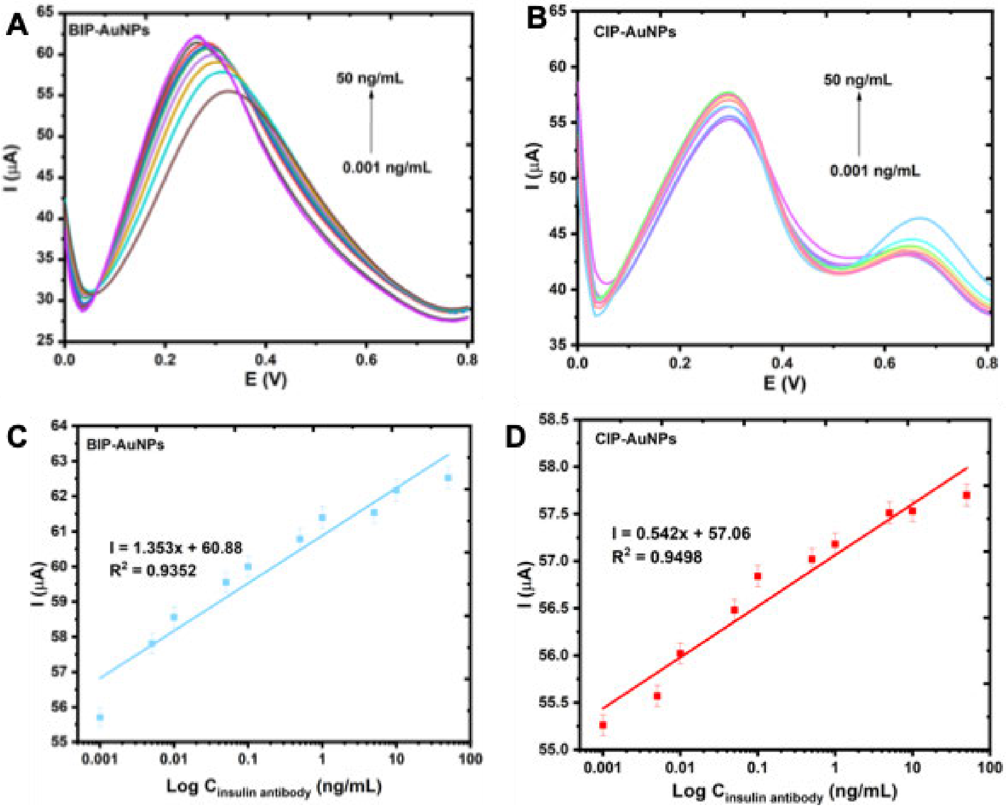

Figure 5.19: SWVs of the designed immunosensor in different insulin antibody concentrations (0.001−50 ng/mL) in a phosphate buffer containing 5.0 mM [Fe(CN)6]$^{3-/4-}$ (**A**) BSA/anti/BIP-AuNPs/PtE and (**B**) BSA/anti/CIP-AuNPs/PtE. The linear dependency between the peak current versus the logarithm concentration of insulin antibody (**C**) BSA/anti/BIP-AuNPs/PtE. and (**D**) BSA/anti/CIP-AuNPs/PtE.

5.8.4 Selectivity, reproducibility, and repeatability

Selectivity was determined by identifying common interferences in human serum at standard quantities. These contained 7.25 mM HAS, 3.0 µM AA, 6.0 mM GL, 0.50 mM UA, and 0.50 µM DP. The sensors' selectivity in terms of current responses was modest when compared to the antibody's current peak. Though some interferences had a substantially lower current response than the insulin antibody. When these interferences were combined with antibody the current peak increased significantly (Figure 5.20a). This demonstrates that the sensors are able to detect the antibody.

The reproducibility of the immunosensors was confirmed through a series of fixed electrodes designed for the detection of 5 ng/mL antibody under optimised experimental conditions (Figures 5.20b and 5.20c). The findings demonstrated satisfactory reproducibility and accuracy, with relative standard deviations of 0.67 % for BIP-AuNPs and 1.21 % for CIP-AuNPs. The validation of repeatability involved detecting 5 ng/mL of antibody concentration 50 times using the same immunosensor. Figure 5.20d clearly displayed that, for BSA/anti/BIP-AuNPs/PtE, there was no considerable change between the first and the 5th cycle. Afterwards, there was a decrease in peak current. And, for BSA/anti/CIP-AuNPs/PtE there was no considerable change between the first and the 15th cycle. Based on these results, BSA/anti/CIP-AuNPs/PtE has more intra-day stability levels.

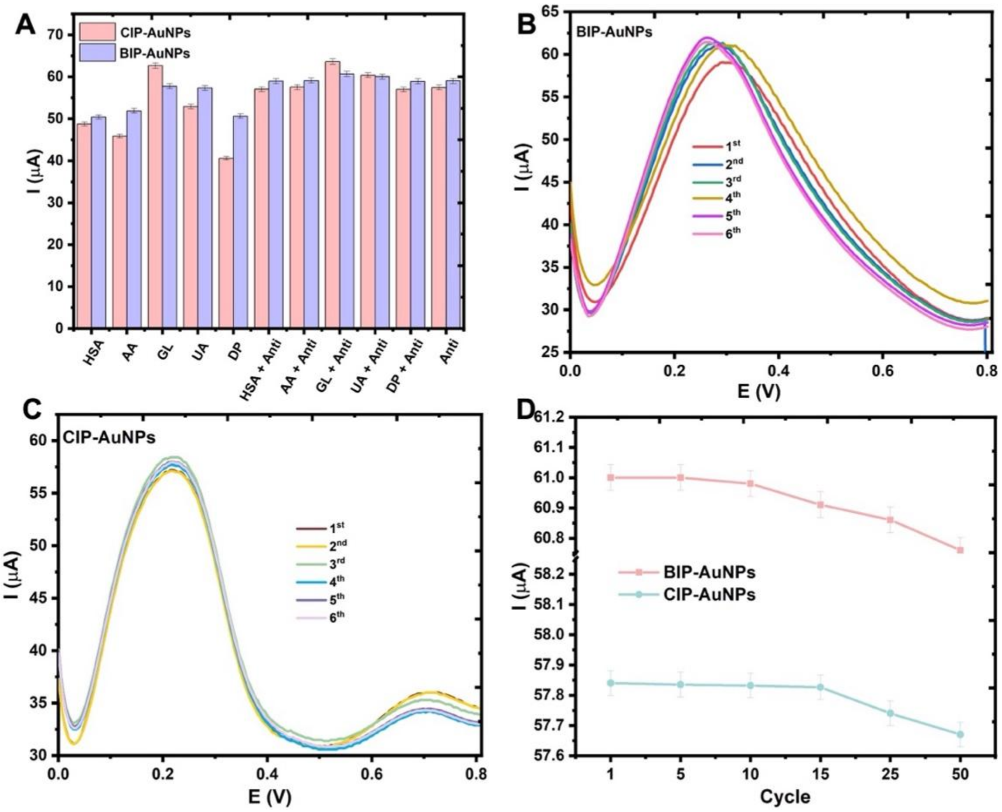

Figure 5.20: (**A**) Histograms of the responses regarding the selectivity investigations of the immunosensors. SWVs of reproducibility response of 5 ng/mL of insulin antibody to 6 different immunosensors under similar conditions (**B**) BSA/anti/BIP-AuNPs/PtE and (**C**) BSA/anti/CIP-AuNPs/PtE. (**D**) Line graph regarding the repeatability investigations.

5.8.5 Recovery studies

The synthetic serum was spiked with three different concentrations (1.00, 1.5, and 5 ng/mL) of insulin antibody and then quantified with the SWV method. Table 5.13 reveals a recovery range of 95.86 -111 % and an RSD of 0.93 -1.43 %. These numbers indicate that the immunosensors demonstrate excellent precision and acceptable accuracy for detecting the insulin antibody. Their dependability makes them ideal for routine analysis. However, BSA/anti/CIP-AuNPs/PtE had better recoveries when compared to BSA/anti/BIP-AuNPs/PtE.

Table 5.13: Recovery results of Insulin antibodies detection in synthetic serum sample using fabricated AuNPs immunosensors.

Sample	Added insulin antibody concertation (ng/mL)	Detected value (ng/mL)	Recovery (%)	RSD %	Standard Error
CIP-AuNPs					
1	1.0	1.110	111	1.76	0.65
2	1.5	1.482	98.8	1.43	1.87
3	5.0	4.985	99.7	0.93	0.76
BIP-AuNPs					
1	1.0	0.961	96.60	0.88	0.49
2	1.5	1.439	95.93	1.06	0.98
3	5.0	4.793	95.86	1.32	1.17

n=3

5.9 Sensor Performance Comparison

The electrochemical performance of the four developed immunosensors was evaluated by comparing their LOD and sensitivity values, as shown in Figure 5.21. Among the four sensors, those modified with cobalt nanoparticles showed the lowest LODs, with CIP-CoNPs achieving an LOD of 0.054 ng/mL, followed by BIP-CoNPs at 0.137 ng/mL (Figure 5.21a). The gold nanoparticle-based sensors exhibited significantly higher LODs, with CIP-AuNPs and BIP-AuNPs reaching 0.990 ng/mL and 1.000 ng/mL, respectively A low LOD indicates higher sensitivity to trace-level analyte detection, which is highly desirable for early-stage diagnostics. Sensitivity, which is the change in current per unit concentration of analyte (μA/ng/mL), is a key parameter for assessing sensor responsiveness.

The CIP-CoNPs sensor again demonstrated superior performance, with the highest sensitivity of 5.60 µA/ng/mL, followed by BIP-AuNPs (3.70 µA/ng/mL), BIP-CoNPs (2.19 µA/ng/mL), and CIP-AuNPs (1.42 µA/ng/mL) as shown in Figure 5.21b. A higher sensitivity indicates a stronger and more measurable signal in response to small analyte concentration changes, making the sensor more effective and reliable for quantification. Sensors with higher sensitivity generally exhibit improved signal-to-noise ratios and stronger analytical performance, particularly in biosensing applications (Nanda *et al.* 2024). These results demonstrate that the CIP-CoNPs modified sensor is the best-performing system, with both the lowest LOD and the highest sensitivity, confirming the combined importance of the metal core (CoNPs) and ligand environment (CIP) in enhancing biosensor efficiency.

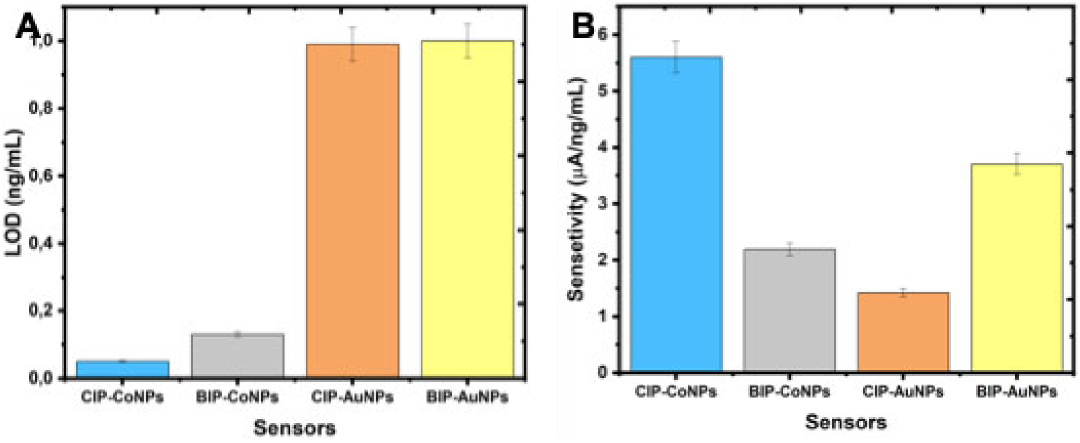

Figure 5.21: The comparison of sensor performance based on (**A**) LOD and (**B**) Sensitivity for CoNPs and AuNPs based immunosensors.

5.10 Summary

For the selective detection of insulin antibody, highly sensitive electrochemical immunosensors based on modification with nanoparticles (cobalt or gold) capped with indole-pyrazole derivatives (bis indole-pyrazole or chromone-indole pyrazole) were successfully synthesised. The nanoparticles were coated onto PtE, which increased the specific surface area and stability of the biosensor platform. Followed by the antigen to facilitate the adsorption of insulin antibody. Resulting in the formation of antigen-antibody complexes, promoting specific spatial arrangement and creating channels that facilitate electron transfer. Each metal nanoparticle had two sensors: one capped with bis indole-pyrazole and another with chromone-indole-pyrazole. High detection ability for insulin antibody with a low detection limit, good selectivity, sufficient stability, and excellent recoveries for all the sensors was achieved. Thereby demonstrating the potential of the developed immunosensors for quantifying insulin antibody. However, the sensors with the chromone-indole-pyrazole (CIP) derivative outperformed the bis indole-pyrazole derivative sensors, exhibiting better LODs and higher recoveries for both metals.

6 CHAPTER 6: CONCLUSION AND FUTURE RECOMMENDATIONS

6.1 Conclusion

To achieve the goal of developing a sensitive electrochemical immunosensor for insulin antibodies, this study was carried out in three connected parts. The first part focused on the design, synthesis, and biological evaluation of two new fused indole-pyrazole compounds. Although the main aim was to use these compounds for sensor development, their biological activity was also explored to better understand how they behave in biological environments. The compounds showed no mutagenic effects, with compound 4b showed strong anticancer potential, while compound 4a had excellent inhibitory activity against diabetes-related enzymes. These results helped justify their use as ligands in the sensor system. The second part focused on the green synthesis of cobalt and gold nanoparticles using lemon peel extract, along with the two indole-pyrazole derivatives. Phytochemical screening confirmed the presence of active compounds like flavonoids, which played an important role in reducing and stabilising the metal ions. The successful synthesis and characterisation of well-shaped nanoparticles confirmed that this eco-friendly method could provide stable nanomaterials suitable for biosensor construction.

In the final part, the nanoparticles were used to develop electrochemical immunosensors. These sensors showed strong performance, including low detection limits, high sensitivity, and good selectivity when detecting insulin antibodies. Among the two, the sensors modified with the chromone-indole-pyrazole derivative performed better than those with the bis indole-pyrazole derivative. This study brought together organic synthesis, green nanotechnology, and electrochemical sensing to create a working diagnostic tool for insulin antibodies. These findings are especially important in the context of type 1 diabetes, where insulin antibodies act as early indicators. The developed immunosensors offer a cost-effective and sensitive platform that could be explored further for early screening and monitoring, and this work also opens new possibilities for multifunctional biosensors in other areas of medical diagnostics.

6.2 Future Recommendations

For future work, using actual patient serum or plasma instead of synthetic serum is recommended to improve the clinical relevance of the results. Real samples would offer a more accurate assessment of the immunosensor's performance under real-world conditions. Additionally, further optimisation of the sensor's sensitivity and specificity could enhance its reliability and potential for use in diagnostic applications.

REFERENCES

Abbasi, N., Ghaneialvar, H., Moradi, R., Zangeneh, M. M. and Zangeneh, A. 2021. Formulation and characterization of a novel cutaneous wound healing ointment by silver nanoparticles containing Citrus lemon leaf: A chemobiological study. *Arabian Journal of Chemistry*, 14 (7): 103246.

Abel, E. D., Gloyn, A. L., Evans-Molina, C., Joseph, J. J., Misra, S., Pajvani, U. B., Simcox, J., Susztak, K. and Drucker, D. J. 2024. Diabetes mellitus—Progress and opportunities in the evolving epidemic. *Cell*, 187 (15): 3789-3820.

Adnan, W. G. and Mohammed, A. M. 2024. Green synthesis of chromium oxide nanoparticles for anticancer, antioxidant and antibacterial activities. *Inorganic Chemistry Communications*, 159: 111683.

Ahmad, S., Munir, S., Zeb, N., Ullah, A., Khan, B., Ali, J., Bilal, M., Omer, M., Alamzeb, M. and Salman, S. M. 2019. Green nanotechnology: A review on green synthesis of silver nanoparticles—An ecofriendly approach. *International Journal of Nanomedicine*, 14: 5087.

Ahmed, K., Tariq, I. and Mudassir, S. U. S. M. 2021. 11. Green synthesis of cobalt nanoparticles by using methanol extract of plant leaf as reducing agent. *Pure and Applied Biology (PAB)*, 5 (3): 453-457.

Al-Ghorbani, M., Alharbi, O., Al-Odayni, A.-B. and Abduh, N. A. 2023. Quinoline- and Isoindoline-Integrated Polycyclic Compounds as Antioxidant, and Antidiabetic Agents Targeting the Dual Inhibition of α-Glycosidase and α-Amylase Enzymes. *Pharmaceuticals*, 16 (9): 1222.

Al-Radadi, N. S. 2021. Facile one-step green synthesis of gold nanoparticles (AuNp) using licorice root extract: Antimicrobial and anticancer study against HepG2 cell line. *Arabian Journal of Chemistry*, 14 (2): 102956.

Alam, M. K., Sahadat Hossain, M., Tabassum, S., Bahadur, N. M. and Ahmed, S. 2024. Green synthesis of nano-MgO using lemon juice for amplified photocatalytic degradation of organic pollutants. *Open Ceramics*, 19: 100625.

Ali, A., Zhang, N. and Santos, R. M. 2023. Mineral characterization using scanning electron microscopy (SEM): a review of the fundamentals, advancements, and research directions. *Applied Sciences*, 13 (23): 12600.

Ali, H., Dixit, S. and Alarifi, S. 2024. Biosynthesis and screening of cobalt nanoparticles using citrus species for antimicrobial activity. *Open Chemistry*, 22 (1)

Aljabali, A. A., Rezigue, M., Alsharedeh, R. H., Obeid, M. A., Mishra, V., Serrano-Aroca, Á., El-Tanani, M. and Tambuwala, M. M. 2022. Protein-based nanomaterials: a new tool for targeted drug delivery. *Therapeutic delivery*, 13 (6): 321-338.

Alvi, G. B., Iqbal, M. S., Ghaith, M. M. S., Haseeb, A., Ahmed, B. and Qadir, M. I. 2021. Biogenic selenium nanoparticles (SeNPs) from citrus fruit have anti-bacterial activities. *Scientific Reports*, 11 (1): 1-11.

Alzahrani, E. and Alkhudidy, A. T. 2021. Synthesis, optimization, and characterization of ecofriendly production of gold nanoparticles using lemon peel extract. *International Journal of Analytical Chemistry*, 2021 (7192868): 1-13.

Anupong, W., On-uma, R., Jutamas, K., Joshi, D., Salmen, S. H., Alahmadi, T. A. and Jhanani, G. K. 2023. Cobalt nanoparticles synthesizing potential of orange peel aqueous extract and their antimicrobial and antioxidant activity. *Environmental Research*, 216: 114594.

Anusha, T., Bhavani, K. S., Kumar, J. S., Brahman, P. K. and Hassan, R. Y. 2022. Fabrication of electrochemical immunosensor based on GCN-β-CD/Au nanocomposite for the monitoring of vitamin D deficiency. *Bioelectrochemistry*, 143 (107935): 1-16.

Arbouche, N., Walch, A., Raul, J. S. and Kintz, P. 2023. Intentional overdose of glargine insulin: Determination of the parent compound in postmortem blood by LC-HRMS. *Journal of forensic sciences*, 68 (3): 1077-1083.

Arya, S., Gourley, A. J., Penedo, J. C., Blindauer, C. A. and Stewart, A. J. 2021. Fatty acids may influence insulin dynamics through modulation of albumin-Zn^{2+} interations. *BioEssays*, 43 (12): 1-9.

Asadpour, F., Mazloum-Ardakani, M., Hoseynidokht, F. and Moshtaghioun, S. M. 2021. In situ monitoring of gating approach on mesoporous silica nanoparticles thin-film generated by the EASA method for electrochemical detection of insulin. *Biosensors and Bioelectronics*, 180 (113124): 1-7.

Ashraf, J., Mughal, E. U., Sadiq, A., Naeem, N., Muhammad, S. A., Qousain, T., Zafar, M. N., Khan, B. A. and Anees, M. 2020. Design and synthesis of new flavonols as dual α-amylase and α-glucosidase inhibitors: structure-activity relationship, drug-likeness, in vitro and in silico studies. *Journal of Molecular Structure*, 1218: 128458.

BabuáGudise, V. 2021. [3+ 2] regioselective annulation reaction of 2-arylidene-1, 3-indandiones towards synthesis of spirocyclopentenes: understanding the mechanism of γ-attack vs. α-attack using DFT studies. *RSC Advances*, 11 (61): 38648-38653.

Bals, J. and Epple, M. 2023. Deep learning for automated size and shape analysis of nanoparticles in scanning electron microscopy. *RSC Advances*, 13 (5): 2795-2802.

Basiaga, M., Paszenda, Z., Walke, W., Karasiński, P. and Marciniak, J. 2014. Electrochemical impedance spectroscopy and corrosion resistance of SiO2 coated cpTi and Ti-6Al-7Nb alloy. In: Proceedings of *Information Technologies in Biomedicine, Volume 4*. Springer, 411-420.

Benvidi, A., Banaei, M., Tezerjani, M. D., Molahosseini, H. and Jahanbani, S. 2018. Impedimetric PSA aptasensor based on the use of a glassy carbon electrode modified with titanium oxide nanoparticles and silk fibroin nanofibers. *Microchimica Acta*, 185: 1-10.

Bhardwaj, G., Kaur, R., Saini, S., Kaur, N. and Singh, N. 2023. Electrochemical and spectroscopic detection of insulin using AgNPs-decorated organic derivative. *Colloids and Surfaces A: Physicochemical and Engineering Aspects*, 679: 132511.

Brais, C. J., Ibañez, J. O., Schwartz, A. J. and Ray, S. J. 2021. Recent advances in instrumental approaches to time-of-flight mass spectrometry. *Mass Spectrometry Reviews*, 40 (5): 647-669.

Bratovcic, A. and Dautovic, A. 2024. Green Synthesis of Silver Nanoparticles Using Aqueous Orange and Lemon Peel Extract and Evaluation of Their Antimicrobial Properties. *Advances in Nanoparticles*, 13 (2): 11-28.

Calabria, D., Lazzarini, E., Pace, A., Trozzi, I., Zangheri, M., Cinti, S., Difonzo, M., Valenti, G., Guardigli, M., Paolucci, F. and Mirasoli, M. 2023. Smartphone-based 3D-printed electrochemiluminescence enzyme biosensor for reagentless glucose quantification in real matrices. *Biosensors and Bioelectronics*, 227: 115146.

Calcagno, D., Perina, M. L., Zingale, G. A., Pandino, I., Tuccitto, N., Oliveri, V., Parravano, M. C. and Grasso, G. 2024. Detection of insulin oligomeric forms by a novel surface plasmon resonance-diffusion coefficient based approach. *Protein Science*, 33 (4): e4962.

Catanzaro, L., Scardaci, V., Scuderi, M., Condorelli, M., D'Urso, L. and Compagnini, G. 2023. Surface plasmon resonance of gold nanoparticle aggregates induced by halide ions. *Materials Chemistry and Physics*, 308: 128245.

Cecchin, A., Reynolds, C., Ali, S. and Hissaria, P. 2023. Evaluation of glutamic acid decarboxylase (GAD) 65 antibody detection methods for neurological and diabetic investigation in an Australian diagnostic laboratory. *Pathology*, 55 (4): 538-542.

Charmkar, R. P., Dubey, N. and Ganeshpurkar, A. 2024. Evaluation of Lemon Peel Extract as Hepatoprotective Agent against Paracetamol-Induced Liver Toxicity: Insights from Biochemical Studies. *Free Radicals and Antioxidants*, 14 (1): 15-20.

Chen, S., Xu, L., Sheng, K., Zhou, Q., Dong, B., Bai, X., Lu, G. and Song, H. 2021. A label-free electrochemical immunosensor based on facet-controlled Au nanorods/reduced graphene oxide composites for prostate specific antigen detection. *Sensors and Actuators B: Chemical*, 336 (129748): 1-9.

Chen, Z., Zhang, Y., Teng, R., Li, M., Ding, C. and Huang, Y. 2025. AIE multifunctional probe empowering colorimetric-fluorescence dual-mode biosensor for early diabetic screening. *Biosensors and Bioelectronics*, 269: 116941.

Chia, S. R., Ahmad, M., Sultana, S., Zafar, M., Asif, S., Bokhari, A., Nomanbhay, S., Mubashir, M., Khoo, K. S. and Show, P. L. 2022. Green synthesis of biodiesel from Citrus medica seed oil using green nanoparticles of copper oxide. *Fuel*, 323: 124285.

Chupradit, S., Km Nasution, M., Rahman, H. S., Suksatan, W., Turki Jalil, A., Abdelbasset, W. K., Bokov, D., Markov, A., Fardeeva, I. N., Widjaja, G., Shalaby, M. N., Saleh, M. M., Mustafa, Y. F., Surendar, A. and Bidares, R. 2022. Various types of electrochemical biosensors for leukemia detection and therapeutic approaches. *Analytical biochemistry*, 654: 114736.

Cittrarasu, V., Kaliannan, D., Dharman, K., Maluventhen, V., Easwaran, M., Liu, W. C., Balasubramanian, B. and Arumugam, M. 2021. Green synthesis of selenium nanoparticles mediated from Ceropegia bulbosa Roxb extract and its cytotoxicity, antimicrobial, mosquitocidal and photocatalytic activities. *Scientific Reports*, 11 (1): 1-15.

Clayden, J., Greeves, N. and Warren, S. 2012. *Organic chemistry*. Oxford University Press, USA.

Costa, J. J., Hosseinzadeh, H., Saha, D. K., Al Mahmud, S. U., Uddin, B. M. M. and Ratan, Z. A. 2021. Green Synthesis of Silver Nanoparticles using Citrus aurantifolia (Bangladeshi Lemon Leaf) Extract and Its Antibacterial Activity. In: Proceedings of *2021 IEEE International Biomedical Instrumentation and Technology Conference (IBITeC)*. IEEE, 29-32.

Coy-Barrera, C. A. and Quiroga, D. 2024. In silico evaluation for the design of coumarin-type compounds based on phenol and naphthol rings as a coating in carbon steel corrosion processes: DFT B3LYP calculations, synthesis and electrochemical characterization. *Progress in Organic Coatings*, 188: 108266.

Cruz, A. G., Haq, I., Cowen, T., Di Masi, S., Trivedi, S., Alanazi, K., Piletska, E., Mujahid, A. and Piletsky, S. A. 2020. Design and fabrication of a smart sensor using in silico epitope mapping and electro-responsive imprinted polymer nanoparticles for determination of insulin levels in human plasma. *Biosensors and Bioelectronics*, 169 (112536): 1-7.

Dadiboyena, S. and Nefzi, A. 2011. Synthesis of functionalized tetrasubstituted pyrazolyl heterocycles–A review. *European journal of medicinal chemistry*, 46 (11): 5258-5275.

De Graaf, R. A. 2019. *In vivo NMR spectroscopy: principles and techniques*. John Wiley & Sons.

Dery, B. and Zaixiang, L. 2023. Scanning electron microscopy (SEM) as an effective tool for determining the morphology and mechanism of action of functional ingredients. *Food Reviews International*, 39 (4): 2007-2026.

Desouky, M. M., Abou-Saleh, R. H., Moussa, T. A. and Fahmy, H. M. 2025. Nano-chitosan-coated, green-synthesized selenium nanoparticles as a novel antifungal agent against Sclerotinia sclerotiorum: in vitro study. *Scientific Reports*, 15 (1): 1004.

Dey, B., Ahmad, M. W., Syed, A., Bahkali, A. H., Verma, M. and Choudhury, A. 2024. Iron metal organic framework decorated carbon nanofiber-based electrode for electrochemical sensing platform of chlorpyrifos in fruits and vegetables. *Materials Science in Semiconductor Processing*, 181: 108669.

Dönmez, S. 2020. Green synthesis of zinc oxide nanoparticles using zingiber officinale root extract and their applications in glucose biosensor. *El-Cezeri Journal of Science and Engineering*, 7 (3): 1191-1200.

Drozd, M., Kobylska, E., Żmieńko, M. and Chudy, M. 2024. Sensitive and label-free SPR biosensing platforms for high-throughput screening of plasma membrane receptors interactions with insulin-like targets of hypoglycaemic activity. *Talanta*, 274: 125914.

El Malahi, A., Van Elsen, M., Charleer, S., Dirinck, E., Ledeganck, K., Keymeulen, B., Crenier, L., Radermecker, R., Taes, Y. and Vercammen, C. 2022. Relationship between time in range, glycemic variability, HbA1c, and complications in adults with type 1 diabetes mellitus. *The Journal of Clinical Endocrinology & Metabolism*, 107 (2): e570-e581.

Elgamouz, A., Idriss, H., Nassab, C., Bihi, A., Bajou, K., Hasan, K., Abu Haija, M. and Patole, S. P. 2020. Green synthesis, characterization, antimicrobial, anti-cancer, and optimization of colorimetric sensing of hydrogen peroxide of algae extract capped silver nanoparticles. *Nanomaterials*, 10 (9): 1861.

Elnoby, R. M., Mourad, M. H., Elnaby, S. L. H. and Kana, M. T. A. 2018. Monocrystalline solar cells performance coated by silver nanoparticles: Effect of NPs sizes from point of view Mie theory. *Optics & Laser Technology*, 101: 208-215.

Fabitha, K., Chandrakanth, M., Pramod, R. N., Arya, C., Li, Y. and Banothu, J. 2022. Recent Developments in the Synthesis of Indole-Pyrazole Hybrids. *ChemistrySelect*, 7 (21): e202201064.

Fan, M., Zhong, X., Huang, Y., Peng, Z. and Wang, G. 2023. Synthesis, biological evaluation and molecular docking studies of chromone derivatives as potential α-glucosidase inhibitors. *Journal of Molecular Structure*, 1274: 134575.

Farooq, S. and Ngaini, Z. 2020. One-pot and two-pot synthesis of chalcone based mono and bis-pyrazolines. *Tetrahedron Letters*, 61 (4): 151416.

Farrokhnia, M., Amoabediny, G., Ebrahimi, M., Ganjali, M. and Arjmand, M. 2022. Ultrasensitive early detection of insulin antibody employing novel electrochemical nano-biosensor based on controllable electro-fabrication process. *Talanta*, 238 (122947): 1-12.

Farzaneh, E., Mohammadi, M., Raymand, P., Noori, M., Golestani, S., Ranjbar, S., Ghasemi, Y., Mohammadi-Khanaposhtani, M., Asadi, M. and Esfahani, E. N. 2024. Pyrano [2, 3-b] chromone derivatives as novel dual inhibitors of α-glucosidase and α-amylase: Design, synthesis, biological evaluation, and in silico studies. *Bioorganic Chemistry*, 145: 107207.

Fayed, E. A., Gohar, N. A., Bayoumi, A. H. and Ammar, Y. A. 2023. Novel fluorinated pyrazole-based heterocycles scaffold: cytotoxicity, in silico studies and molecular modelling targeting double mutant EGFR L858R/T790M as antiproliferative and apoptotic agents. *Medicinal Chemistry Research*, 32 (2): 369-388.

Forte, A., Gawne, T., Humphries, O. S., Campbell, T., Shi, Y. and Vinko, S. M. 2024. Methods for energy dispersive x-ray spectroscopy with photon-counting and deconvolution techniques. *arXiv preprint arXiv:2411.16581*, Gao, Z., Li, Y., Zhang, C., Zhang, S., Li, F., Wang, P., Wang, H. and Wei, Q. 2019. Label-free electrochemical immunosensor for insulin detection by high-efficiency synergy strategy of Pd NPs@ 3D MoS_x towards H_2O_2. *Biosensors and Bioelectronics*, 126 (2019): 108-114.

Garg, R., Kumari, M., Kumar, M., Dhiman, S. and Garg, R. 2021. Green synthesis of calcium carbonate nanoparticles using waste fruit peel extract. *Materials Today: Proceedings*, 46 (170955): 6665-6668.

Geetha Bai, R., Muthoosamy, K., Tuvikene, R., Nay Ming, H. and Manickam, S. 2021. Highly sensitive electrochemical biosensor using folic acid-modified reduced graphene oxide for the detection of cancer biomarker. *Nanomaterials*, 11 (5): 1272.

Gijare, M., Chaudhari, S., Ekar, S., Shaikh, S. F., Mane, R. S., Pandit, B., Siddiqui, M. U. H. and Garje, A. 2023. Facile Green Preparation of Reduced Graphene Oxide Using Citrus Limetta-Decorated rGO/TiO2 Nanostructures for Enzymeless Glucose Sensing Application. *Electronics*, 12 (2): 294.

Gomaa, E. Z. 2022. Microbial mediated synthesis of zinc oxide nanoparticles, characterization and multifaceted applications. *Journal of Inorganic and Organometallic Polymers and Materials*, 32 (11): 4114-4132.

Guziejewski, D., Smarzewska, S. and Mirceski, V. 2023. Analytical aspects of novel techniques derived from square-wave voltammetry. *Journal of The Electrochemical Society*, 170 (6): 066503.

Hacke, A. C. M., Lima, D. and Kuss, S. 2022. Green synthesis of electroactive nanomaterials by using plant-derived natural products. *Journal of Electroanalytical Chemistry*: 116786.

Hallemans, N., Howey, D., Battistel, A., Saniee, N. F., Scarpioni, F., Wouters, B., La Mantia, F., Hubin, A., Widanage, W. D. and Lataire, J. 2023. Electrochemical impedance spectroscopy beyond linearity and stationarity—A critical review. *Electrochimica Acta*: 142939.

Hassan, A. S., Moustafa, G. O., Awad, H. M., Nossier, E. S. and Mady, M. F. 2021. Design, synthesis, anticancer evaluation, enzymatic assays, and a molecular modeling study of novel pyrazole–indole hybrids. *ACS omega*, 6 (18): 12361-12374.

Hassanisaadi, M., Bonjar, G. H. S., Rahdar, A., Pandey, S., Hosseinipour, A. and Abdolshahi, R. 2021. Environmentally safe biosynthesis of gold nanoparticles using plant water extracts. *Nanomaterials*, 11 (8): 2033.

Hawash, M., Ergun, S. G., Kahraman, D. C., Olgac, A., Hamel, E., Cetin-Atalay, R. and Baytas, S. N. 2023. Novel indole-pyrazole hybrids as potential tubulin-targeting agents; Synthesis, antiproliferative evaluation, and molecular modeling studies. *Journal of Molecular Structure*, 1285: 135477.

Hodoroaba, V.-D. 2020. Chapter 4.4 - Energy-dispersive X-ray spectroscopy (EDS). In: Hodoroaba, V.-D., Unger, W. E. S. and Shard, A. G. eds. *Characterization of Nanoparticles*. Elsevier, 397-417. Available: https://www.sciencedirect.com/science/article/pii/B9780128141823000213 (Accessed

Hosny, M., Fawzy, M., Abdelfatah, A. M., Fawzy, E. E. and Eltaweil, A. S. 2021. Comparative study on the potentialities of two halophytic species in the green synthesis of gold nanoparticles and their anticancer, antioxidant and catalytic efficiencies. *Advanced Powder Technology*, 32 (9): 3220-3233.

Hosny, M., Fawzy, M., El-Fakharany, E. M., Omer, A. M., Abd El-Monaem, E. M., Khalifa, R. E. and Eltaweil, A. S. 2022. Biogenic synthesis, characterization, antimicrobial, antioxidant, antidiabetic, and catalytic applications of platinum nanoparticles synthesized from Polygonum salicifolium leaves. *Journal of Environmental Chemical Engineering*, 10 (1): 106806.

Hu, C., Liang, B., Sun, J., Li, J., Xiong, Z., Wang, S.-H. and Xuetao, X. 2024. Synthesis and biological evaluation of indole derivatives containing thiazolidine-2, 4-dione as α-glucosidase inhibitors with antidiabetic activity. *European Journal of Medicinal Chemistry*, 264: 115957.

Hu, H., Wang, F., Ding, X., Imhanria, S., Wang, W. and Zhang, J. 2022. Green fabrication of Pt nanoparticles via tea-polyphenols for hydrogen peroxide detection. *Colloids and Surfaces A: Physicochemical and Engineering Aspects*, 637: 128201.

Huang, X., Zhu, Y. and Kianfar, E. 2021. Nano biosensors: properties, applications and electrochemical techniques. *Journal of Materials Research and Technology*, 12: 1649-1672.

Jahan, I. and Isildak, İ. b. 2021. Lemon Peel Extract for Synthesizing Non-Toxic Silver Nanoparticles through One-Step Microwave-Accelerated Scheme. *Kahramanmaraş Sütçü İmam Üniversitesi Tarım ve Doğa Dergisi*, 24 (1): 1-10.

Jayarambabu, N., Saraswathi, K., Akshaykranth, A., Anitha, N. and Rao, T. V. 2023. Bamboo-mediated silver nanoparticles functionalized with activated carbon and their application for non-enzymatic glucose sensing. *Inorganic Chemistry Communications*, 147: 110249.

Jebali, M., Gómez-Merino, A. I. and Colangelo, G. 2025. Influence of the lemon (Citrus Limon L.) juice amount on the green synthesis of CuO nanoparticles: Characterization, stability and thermal conductivity. *Ceramics International*, 51 (1): 72-84.

Jeevanandam, J., Ling, J. K. U., Barhoum, A., San Chan, Y. and Danquah, M. K. 2022. Bionanomaterials: definitions, sources, types, properties, toxicity, and regulations. In: Barhoum, A. and Danquah, M. K. eds. *Fundamentals of Bionanomaterials*. Elsevier, 1-29.

Jeong, G.-J., Khan, S., Tabassum, N., Khan, F. and Kim, Y.-M. 2022. Marine-bioinspired nanoparticles as potential drugs for multiple biological roles. *Marine Drugs*, 20 (8): 527.

Jessy Mercy, D., Girigoswami, K. and Girigoswami, A. 2024. A mini review on biosensor advancements-emphasis on quantum dots. *Results in Chemistry*, 7: 101271.

Joshi, R. J., Varu, H. L., Bhalodia, J. J., Ambasana, M. A., Bapodra, A. H. and Kapuriya, N. P. 2024. Highly selective fluorescence sensor based on azido pyrazole-chalcone conjugates for rapid detection of iodide ion. *Results in Chemistry*, 7: 101409.

Jozghorbani, M., Fathi, M., Kazemi, S. H. and Alinejadian, N. 2021. Determination of carcinoembryonic antigen as a tumor marker using a novel graphene-based label-free electrochemical immunosensor. *Analytical biochemistry*, 613 (114017): 1-8.

Judák, P., Coppieters, G., Lapauw, B., Van Eenoo, P. and Deventer, K. 2020. Urinary detection of rapid-acting insulin analogs in healthy humans. *Drug Testing and Analysis*, 12 (11-12): 1629-1635.

Kansay, V., Sharma, V. D., Srivastava, V., Batra, N., Chakrabarti, S. and Bera, M. 2024. Wearable, disposable and non-enzymatic fluorescence nanosensor for monitoring sweat glucose through smartphone. *Microchemical Journal*, 201: 110624.

Karaman, C., Karaman, O., Atar, N. and Yola, M. L. 2021. Electrochemical immunosensor development based on core-shell high-crystalline graphitic carbon nitride@ carbon dots and $Cd_{0.5}Zn_{0.5}S$/d-$Ti_3C_2T_x$ MXene composite for heart-type fatty acid–binding protein detection. *Microchimica Acta*, 188 (6): 1-15.

Karastogianni, S., Paraschi, I. and Girousi, S. 2022. Electrochemical sensing of the maple syrup urine disease biomarker valine, using saffron-silver nanoparticles. *Biosensors and Bioelectronics: X*, 12: 100275.

Kasturi, S., Eom, Y., Torati, S. R. and Kim, C. 2021. Highly sensitive electrochemical biosensor based on naturally reduced rGO/Au nanocomposite for the detection of miRNA-122 biomarker. *Journal of Industrial and Engineering Chemistry*, 93: 186-195.

Kasumbwe, K., N Venugopala, K., Mohanlall, V. and Odhav, B. 2017. Synthetic mono/di-halogenated coumarin derivatives and their anticancer properties. *Anti-Cancer Agents in Medicinal Chemistry (Formerly Current Medicinal Chemistry-Anti-Cancer Agents)*, 17 (2): 276-285.

Kem, A., Ansari, M. R., Prathap, P., Jayasimhadri, M. and Peta, K. R. 2022. Eco-friendly green synthesis of stable ZnO nanoparticles using citrus limon: X-ray diffraction analysis and optical properties. *Physica Scripta*, 97 (8): 085814.

Kesharwani, P., Ma, R., Sang, L., Fatima, M., Sheikh, A., Abourehab, M. A., Gupta, N., Chen, Z.-S. and Zhou, Y. 2023. Gold nanoparticles and gold nanorods in the landscape of cancer therapy. *Molecular cancer*, 22 (1): 98.

Khadhim, A. I. and Kadhim, R. E. 2021. Synthesis of Cobalt Nanoparticles Biologically by Conocarpus erectus L. Aqueous Leaves Extract. *Annals of the Romanian Society for Cell Biology*: 5361-5372.

Khalil, A. T., Ovais, M., Iqbal, J., Ali, A., Ayaz, M., Abbas, M., Ahmad, I. and Devkota, H. P. 2022. Microbes-mediated synthesis strategies of metal nanoparticles and their potential role in cancer therapeutics. *Seminars in Cancer Biology*, 86: 693-705.

Khan, M., Khan, S., Omar, M., Sohail, M. and Ullah, I. 2024. Nickel and cobalt magnetic nanoparticles (MNPs): synthesis, characterization, and applications. *Journal of Chemical Reviews*, 6 (1): 94-114.

Kharade Suvarta, D., Nikam Gurunath, H., Mane Gavade Shubhangi, J., Patil Sachinkumar, R. and Gaikwad Kishor, V. 2020. Biogenic synthesis of cobalt nanoparticles using Hibiscus cannabinus leaf extract and their antibacterial activity. *Res J Chem Environ*, 24 (5): 9-13.

Khursheed, A. 2024. Scanning electron microscopy.

Kirishnamaline, G., Magdaline, J. D. and Chithambarathanu, T. 2023. Structural elucidation, spectroscopic investigation, in silico docking, and in vitro cytotoxicity studies of chromone derivatives as potential anti-breast cancer agents. *Journal of Molecular Structure*, 1284: 135306.

Kiteto, M. K. and Mecha, C. A. 2024. Insight into the bouguer-beer-lambert law: a review. *Sustainable Chemical Engineering*: 567-587.

Kokoskarova, P., Stojanov, L., Najkov, K., Ristovska, N., Ruskovska, T., Skrzypek, S. and Mirceski, V. 2023. Square-wave voltammetry of human blood serum. *Scientific Reports*, 13 (1): 8485.

Kröger, S. and Danielsson, B. 2024. Calorimetric biosensors. In: *Handbook of Biosensors and Electronic Noses*. CRC Press, 279-298.

Kurma, S. H., Somanaboina, R., Vanammoole, L. R., Srivishnu, K., Bhimapaka, C. R. and Giribabu, L. 2023. 2 H-Pyrano [3, 2-c] chromene-2, 5 (6 H)-diones: Synthesis, Characterization, Photophysical and Redox Studies for Potential Optoelectronic Applications. *Journal of Fluorescence*, 33 (3): 1125-1138.

Kytsya, A., Berezovets, V., Verbovytskyy, Y., Bazylyak, L., Kordan, V., Zavaliy, I. and Yartys, V. 2022. Bimetallic Ni-Co nanoparticles as an efficient catalyst of hydrogen generation via hydrolysis of NaBH4. *Journal of Alloys and Compounds*, 908: 164484.

Lago, B. C., Silva, C. A., Melo, L. C. A. and de Morais, E. G. 2021. Predicting biochar cation exchange capacity using Fourier transform infrared spectroscopy combined with partial least square regression. *Science of The Total Environment*, 794: 148762.

Lakhera, P., Chaudhary, V., Singh, S., Vishwakarma, N., Sanchez Huertas, C., Kumar, P. and Kumar, S. 2023. Detection of glycosylated hemoglobin on boronic acid-modified zeolitic imidazolate framework-8 nanoparticles. *ACS Applied Nano Materials*, 6 (24): 22857-22864.

Lazanas, A. C. and Prodromidis, M. I. 2023. Electrochemical impedance spectroscopy─ a tutorial. *ACS Measurement Science Au*, 3 (3): 162-193.

Li, Q., Wang, H., Wang, T., Li, X., Liu, Y., Chen, W. and You, Z. 2024. Online diagnosis method of water management faults based on hybrid-frequency electrochemical impedance spectroscopy for PEMFC. *IEEE Transactions on Transportation Electrification*,

Li, S., Al-Misned, F. A., El-Serehy, H. A. and Yang, L. 2021. Green synthesis of gold nanoparticles using aqueous extract of Mentha Longifolia leaf and investigation of its anti-human breast carcinoma properties in the in vitro condition. *Arabian Journal of Chemistry*, 14 (2): 102931.

Lind, A., Freyhult, E., de Jesus Cortez, F., Ramelius, A., Bennet, R., Robinson, P. V., Seftel, D., Gebhart, D., Tandel, D. and Maziarz, M. 2024. Childhood screening for type 1 diabetes comparing automated multiplex Antibody Detection by Agglutination-PCR (ADAP) with single plex islet autoantibody radiobinding assays. *EBioMedicine*, 104

Liu, J., Zhu, B., Dong, H., Zhang, Y., Xu, M., Travas-Sejdic, J. and Chang, Z. 2021. A novel electrochemical insulin aptasensor: from glassy carbon electrodes to disposable, single-use laser-scribed graphene electrodes. *Bioelectrochemistry*, 143 (107995): 1-10.

Liu, X., Atwater, M., Wang, J. and Huo, Q. 2007. Extinction coefficient of gold nanoparticles with different sizes and different capping ligands. *Colloids and surfaces B: Biointerfaces*, 58 (1): 3-7.

Liu, Y., Yue, W. and Cui, Y. 2023. Development of an amperometric biosensor on a toothbrush for glucose. *Sensors and Actuators Reports*, 5: 100133.

Long, L.-L., Hu, W.-X., Wang, X., Yuan, R. and Chai, Y.-Q. 2024. Antibody-Protein-Aptamer Electrochemical Biosensor based on Highly Efficient Proximity-Induced DNA Hybridization on Tetrahedral DNA Nanostructure for Sensitive Detection of Insulin-like Growth Factor-1. *Analytical Chemistry*, 96 (9): 3837-3843.

Lü, H., Wang, H., Yang, L., Zhou, Y., Xu, L., Hui, N. and Wang, D. 2022. A sensitive electrochemical sensor based on metal cobalt wrapped conducting polymer polypyrrole nanocone arrays for the assay of nitrite. *Microchimica Acta*, 189: 1-9.

Ma, J., Yu, J., Chen, G., Bai, Y., Liu, S., Hu, Y., Al-Mamun, M., Wang, Y., Gong, W. and Liu, D. 2023. Rational design of N-doped carbon-coated cobalt nanoparticles for highly efficient and durable photothermal CO2 conversion. *Advanced Materials*, 35 (42): 2302537.

Ma, X. and Zhang, W. 2022. Recent developments in one-pot stepwise synthesis (OPSS) of small molecules. *Iscience*, 25 (9)

Mageed, A. H., Mohsin, M. I. and Al-Sahaf, S. 2023. One-Pot Multicomponent Synthesis, Antibacterial and Antiproliferative Evaluation of Indole Derivatives. *Pharmaceutical Chemistry Journal*, 57 (2): 250-264.

Mahiuddin, M. and Ochiai, B. 2022. Comprehensive study on lemon juice-based green synthesis and catalytic activity of bismuth nanoparticles. *ACS omega*, 7 (40): 35626-35634.

Mahmood, H., Hussain, S. B., Nosheen, A., Mahmood, T., Shafique, M., Ul-Haq, N. and Haq, A. U. 2021. Antibacterial activities of gold nanoparticles synthesized by Citrus limonum fruit extract. *Pak. J. Bot*, 53 (6): 2305-2310.

Majola, S., Sabela, M., Gengan, R. M. and Makhanya, T. R. 2023. Enzyme-indole Pyrazole-capped SeNPs based Electrochemical Biosensor for Sensitive

Detection of Adenosine Triphosphate. *Current Analytical Chemistry*, 19 (4): 298-308.

Makhanya, T. R., Gengan, R. M. and Kasumbwe, K. 2020. Synthesis of Fused Indolo-Pyrazoles and Their Antimicrobial and Insecticidal Activities against Anopheles arabiensis Mosquito. *ChemistrySelect*, 5 (9): 2756-2762.

Maleki, F., Rashidi, M.-R., Razmi, H. and Ghorbani, M. 2023. Label-free electrochemical immunosensor for detection of insulin-like growth factor-1 (IGF-1) using a specific monoclonal receptor on electrospun Zein-based nanofibers/rGO-modified electrode. *Talanta*: 124844.

Mamuru, S., Malachy, M., Eseyin, A. and Ankwai, G. 2022. The use of *Amaranthus Spinosus* in the synthesis of silver nanoparticles and their application in the detection of glucose. *Journal of Chemical Society of Nigeria*, 47 (2)

Man, R. J., Lu, T., Zheng, C. C., Li, T., Wu, M. K., Li, D. D. and He, X. M. 2023. Discovery of pyrazole-carbohydrazide with indole moiety as tubulin polymerization inhibitors and anti-tumor candidates. *Drug Development Research*, 84 (1): 110-120.

Mandali, P. K., Prabakaran, A., Annadurai, K. and Krishnan, U. M. 2023. Trends in Quantification of HbA1c Using Electrochemical and Point-of-Care Analyzers. *Sensors*, 23 (4): 1901.

Mandru, A., Mane, J. and Mandapati, R. 2023. A Review on UV-visible spectroscopy. *Journal of Pharma Insights and Research*, 1 (2): 091-096.

Maron, D. M. and Ames, B. N. 1983. Revised methods for the Salmonella mutagenicity test. *Mutation Research/Environmental Mutagenesis and Related Subjects*, 113 (3-4): 173-215.

Mathew, B. B., Jatawa, S. K. and Tiwari, A. 2012. Phytochemical analysis of Citrus limonum pulp and peel. *Int J Pharm Pharm Sci*, 4 (2): 369-371.

Mazloum-Ardakani, M., Barazesh, B., Khoshroo, A., Moshtaghiun, M. and Sheikhha, M. H. 2018. A new composite consisting of electrosynthesized conducting polymers, graphene sheets and biosynthesized gold nanoparticles for biosensing acute lymphoblastic leukemia. *Bioelectrochemistry*, 121: 38-45.

Mazloum-Ardakani, M., Barazesh, B. and Moshtaghioun, S. M. 2019. An aptasensor based on electrosynthesized conducting polymers, Cu_2O–carbon dots and biosynthesized gold nanoparticles, for monitoring carcinoembryonic antigen. *Journal of Nanostructures*, 9 (4): 659-668.

Megale, J. D. and De Souza, D. 2023. New approaches in antibiotics detection: the use of square wave voltammetry. *Journal of Pharmaceutical and Biomedical Analysis*, 234: 115526.

Mei, Y., Pan, X., Pan, J., Zhang, M. and Shen, H. 2025. Biosensor development for diabetes diagnosis: Determining relevant miRNA using a newly developed N-annulated perylene fluorescent dye. *Talanta*, 282: 126992.

Meydanju, N., Pirsa, S. and Farzi, J. 2022. Biodegradable film based on lemon peel powder containing xanthan gum and TiO_2–Ag nanoparticles: Investigation of physicochemical and antibacterial properties. *Polymer Testing*, 106 (107445): 1-12.

Mgwili, P. Y. 2017. Graphenated organic nanoparticles immunosensors for the detection of TB biomarkers (mini Dissertation). BSc Honours, University of the Western Cape. Available: http://hdl.handle.net/11394/6355 (Accessed

Mohd Yusof, H., Abdul Rahman, N. A., Mohamad, R. and Zaidan, U. H. 2020. Microbial mediated synthesis of silver nanoparticles by lactobacillus plantarum TA4 and its antibacterial and antioxidant activity. *Applied Sciences*, 10 (19): 6973.

Mojsoska, B., Larsen, S., Olsen, D. A., Madsen, J. S., Brandslund, I. and Alatraktchi, F. A. 2021. Rapid SARS-CoV-2 detection using electrochemical immunosensor. *Sensors*, 21 (2): 1-11.

Moscoso, R., Barrientos, C., Abarca, S. and Squella, J. A. 2023. Electrochemical characterization of nitrocoumarin-modified nanostructured electrode platforms: New precursors for the electrocatalysis of NADH. *Electrochimica Acta*, 443: 141933.

Moussa, F. B., Achi, F., Meskher, H., Henni, A. and Belkhalfa, H. 2022. Green one-step reduction approach to prepare rGO@ AgNPs coupled with molecularly imprinted polymer for selective electrochemical detection of lactic acid as a cancer biomarker. *Materials Chemistry and Physics*, 289: 126456.

Mucha, P., Hikisz, P., Gwoździński, K., Krajewska, U., Leniart, A. and Budzisz, E. 2019. Cytotoxic effect, generation of reactive oxygen/nitrogen species and electrochemical properties of Cu (II) complexes in comparison to half-sandwich complexes of Ru (II) with aminochromone derivatives. *RSC Advances*, 9 (55): 31943-31952.

Mushtaq, I. and Ahmed, A. 2023. Synthesis of biologically active sulfonamide-based indole analogs: a review. *Future Journal of Pharmaceutical Sciences*, 9 (1): 46.

Muthuchamy, N., Atchudan, R., Edison, T. N. J. I., Perumal, S. and Lee, Y. R. 2018. High-performance glucose biosensor based on green synthesized zinc oxide nanoparticle embedded nitrogen-doped carbon sheet. *Journal of Electroanalytical Chemistry*, 816: 195-204.

Nahar, K. N., Rahaman, M., Khan, G., Islam, M. and Al-Reza, S. M. 2021. Green synthesis of silver nanoparticles from Citrus sinensis peel extract and its antibacterial potential. *Asian Journal of Green Chemistry*, 5 (1): 135-150.

Nanda, A., Kalyani, T., Kotal, H. and Jana, S. K. 2024. Highly Sensitive Electrochemical Immunosensor for Ultra-Low-Level Detection of Interleukin-10 using A Cost-Effective Gold Nanoparticle-Modified Electrode. *Analytical and Bioanalytical Electrochemistry*, 16 (1): 60-78.

Nandhakumar, P., Muñoz San Martín, C., Arévalo, B., Ding, S., Lunker, M., Vargas, E., Djassemi, O., Campuzano, S. and Wang, J. 2023. Redox cycling amplified electrochemical lateral-flow immunoassay: Toward decentralized sensitive insulin detection. *ACS sensors*, 8 (10): 3892-3901.

Nandiyanto, A. B. D., Ragadhita, R. and Fiandini, M. 2023. Interpretation of Fourier transform infrared spectra (FTIR): A practical approach in the polymer/plastic thermal decomposition. *Indonesian Journal of Science and Technology*, 8 (1): 113-126.

Nassar, M. Y., Shaker, F. A., El-Sayed, G., Masoud, E. M., Adam, M. S., Khalil, A., Rashed, N. M., Abdelaziz, G. and El-Feky, H. H. 2024. Synthesis and Characterization of Lemon Leaf Extract-Mediated Silver Nanoparticles: An

Environmentally Friendly Approach with Enhanced Antibacterial Efficacy. *Journal of Molecular Structure*: 138753.

Nazarpour, S., Hajian, R. and Sabzvari, M. H. 2020. A novel nanocomposite electrochemical sensor based on green synthesis of reduced graphene oxide/gold nanoparticles modified screen printed electrode for determination of tryptophan using response surface methodology approach. *Microchemical Journal*, 154: 104634.

Negahdary, M. and Angnes, L. 2022. Application of electrochemical biosensors for the detection of microRNAs (miRNAs) related to cancer. *Coordination Chemistry Reviews*, 464: 214565.

Nigam, V., Singh, S., Kasana, S., Kumar, S., Das Kurmi, B., Das Gupta, G. and Patel, P. 2024. Revolutionizing Indole Synthesis: A Microwave-Powered Approach. *ChemistrySelect*, 9 (23): e202402171.

Niri, D. R., Sayahi, M. H., Behrouz, S., Moazzam, A., Mojtabavi, S., Faramarzi, M. A., Larijani, B., Rastegar, H., Mohammadi-Khanaposhtani, M. and Mahdavi, M. 2022. Design, synthesis, in vitro, and in silico biological evaluations of coumarin-indole hybrids as new anti-α-glucosidase agents. *BMC chemistry*, 16 (1): 84.

Nitulescu, G. M., Stancov, G., Seremet, O. C., Nitulescu, G., Mihai, D. P., Duta-Bratu, C. G., Barbuceanu, S. F. and Olaru, O. T. 2023. The importance of the pyrazole scaffold in the design of protein kinases inhibitors as targeted anticancer therapies. *Molecules*, 28 (14): 5359.

Nobahar, A., Lourenço, J. P., Costa, M. C. and Carlier, J. D. 2024. Printed Circuit Boards Leaching Followed by Synthesis of Gold Nanoparticle Clusters Using Plant Extracts. *Waste and Biomass Valorization*, 15 (4): 1999-2017.

Otitolaiye, C., Omonkhua, A., Oriakhi, K., Okello, E., Onoagbe, I. and Okonofua, F. 2023. Phytochemical analysis and in-vitro antioxidant potential of aqueous and ethanol extracts of Irvingia gabonensis stem bark. *Pharmacognosy Research*,

Oudah Mezan, S. and Khalaf Jabbar, K. 2024. Green synthesis of copper (II) oxide nanoparticles using lemon leaves and optimization for characterization. *Journal of Nanostructures*,

Pechyen, C., Ponsanti, K., Tangnorawich, B. and Ngernyuang, N. 2021. Waste fruit peel–Mediated green synthesis of biocompatible gold nanoparticles. *Journal of Materials Research and Technology*, 14: 2982-2991.

Pham, V. T. B., Nguyen, T. V., Nguyen, H. V., Nguyen, T. T. and Hoang, H. M. 2020. Curcuminoids versus pyrazole-modified analogues: synthesis and cytotoxicity against HepG2 cancer cell line. *ChemistrySelect*, 5 (37): 11681-11684.

Picollo, M., Aceto, M. and Vitorino, T. 2019. UV-Vis spectroscopy. *Physical sciences reviews*, 4 (4): 20180008.

Poudineh, M., Maikawa, C. L., Ma, E. Y., Pan, J., Mamerow, D., Hang, Y., Baker, S. W., Beirami, A., Yoshikawa, A. and Eisenstein, M. 2021. A fluorescence sandwich immunoassay for the real-time continuous detection of glucose and insulin in live animals. *Nature biomedical engineering*, 5 (1): 53-63.

Qi, J., Wei, F., Tung, C. H. and Xu, Z. 2021. Modular Synthesis of α-Quaternary Chiral β-Lactams by a Synergistic Copper/Palladium-Catalyzed Multicomponent Reaction. *Angewandte Chemie International Edition*, 60 (25): 13814-13818.

Rahman, M. M., Islam, F., Parvez, A., Azad, M. A., Ashraf, G. M., Ullah, M. F. and Ahmed, M. 2022. Citrus limon L.(lemon) seed extract shows neuro-modulatory activity in an in vivo thiopental-sodium sleep model by reducing the sleep onset and enhancing the sleep duration. *Journal of Integrative Neuroscience*, 21 (1): 42.

Rahmati, Z., Roushani, M., Hosseini, H. and Choobin, H. 2021. Electrochemical immunosensor with Cu_2O nanocube coating for detection of SARS-CoV-2 spike protein. *Microchimica Acta*, 188 (3): 1-9.

Rasitanon, N., Veenuttranon, K., Thandar Lwin, H., Kaewpradub, K., Phairatana, T. and Jeerapan, I. 2023. Redox-Mediated Gold Nanoparticles with Glucose Oxidase and Egg White Proteins for Printed Biosensors and Biofuel Cells. *International Journal of Molecular Sciences*, 24 (5): 4657.

Rey-Méndez, R., Rodríguez-Argüelles, M. C. and González-Ballesteros, N. 2022. Flower, stem, and leaf extracts from Hypericum perforatum L. to synthesize gold nanoparticles: Effectiveness and antioxidant activity. *Surfaces and Interfaces*, 32: 102181.

Ríos-Reina, R. and Azcarate, S. M. 2022. How chemometrics revives the UV-Vis spectroscopy applications as an analytical sensor for spectralprint (nontargeted) analysis. *Chemosensors*, 11 (1): 8.

Rubio-Melgarejo, A., Balois-Morales, R., Palomino-Hermosillo, Y. A., López-Guzmán, G. G., Ramírez-Ramírez, J. C., Cervantes-García, E., Villalobos-Rosario, B. J. and Bautista-Rosales, P. U. 2020. Phytochemical and Antioxidant Dynamics of the Soursop Fruit (Annona muricata L.) in response to Colletotrichum spp. *Journal of Food Quality*, 2020 (1): 3180634.

Sadique, M. A., Yadav, S., Ranjan, P., Khan, R., Khan, F., Kumar, A. and Biswas, D. 2022. Highly sensitive electrochemical immunosensor platforms for dual detection of SARS-CoV-2 antigen and antibody based on gold nanoparticle functionalized graphene oxide nanocomposites. *ACS Applied Bio Materials*, 5 (5): 2421-2430.

Sahu, A., Chatterjee, P. and Chakraborty, A. K. 2022. Non-enzymatic electrochemical sensing of glucose using phyto-extract modified reduced graphene oxide. *MRS Communications*, 12 (5): 902-909.

Sakthivel, S., Dhanapal, A. R., Paulraj, L. P., Gurusamy, A., Venkidasamy, B., Thiruvengadam, M., Govindasamy, R., Shariati, M. A., Bouyahya, A. and Zengin, G. 2022. Antibacterial activity of seed aqueous extract of Citrus limon (L.) mediated synthesis ZnO NPs: An impact on Zebrafish (Danio rerio) caudal fin development. *Heliyon*, 8 (9)

Salih, R. H., Ahmed, S. H., Hameed, R. S. and Al-Karkhi, I. H. T. 2021. Evaluation of a New Green Zirconium Nanoparticle from Lemon and Peel Extract Antioxidant and Anticancer Activity. *Medico Legal Update*, 21 (2): 977-981.

Salvi, V. K., Punia, K., Tiwari, S., Yadav, A. and Kumar, S. 2024. Lemon juice assisted green synthesis, structural and optical properties of NiO nanoparticles. In: Proceedings of *AIP Conference Proceedings*. AIP Publishing,

Santos, F. D. S., da Silva, L. V., Campos, P. V. S., de Medeiros Strunkis, C., Ribeiro, C. M. G. and Salles, M. O. 2022. Recent advances of electrochemical techniques in food, energy, environment, and forensic applications. *ECS Sensors Plus*, 1 (1): 013603.

Serpell, C. J., Cookson, J. and Beer, P. D. 2020. N-Functionalised Imidazoles as Stabilisers for Metal Nanoparticles in Catalysis and Anion Binding. *ChemistryOpen*, 9 (6): 683-690.

Shamsipur, M., Samandari, L., Farzin, L., Molaabasi, F. and Mousazadeh, M. H. 2020. Dual-modal label-free genosensor based on hemoglobin@gold nanocluster stabilized graphene nanosheets for the electrochemical detection of BCR/ABL fusion gene. *Talanta*, 217: 121093.

Shao, B., Ai, Y., Yan, L., Wang, B., Huang, Y., Zou, Q., Fu, H., Niu, X. and Sun, W. 2023. Wireless electrochemical sensor for the detection of phytoregulator indole-3-acetic acid using gold nanoparticles and three-dimensional reduced graphene oxide modified screen printed carbon electrode. *Talanta*, 253: 124030.

Sharma, R. and Kukreja, V. 2022. Amalgamated convolutional long term network (CLTN) model for Lemon Citrus Canker Disease Multi-classification. In: Proceedings of *2022 International conference on decision aid sciences and applications (DASA)*. IEEE, 326-329.

Sharma, S. and Chand, P. 2023. Supercapacitor and electrochemical techniques: A brief review. *Results in Chemistry*, 5: 100885.

Sharma, S. K., Sharma, P. R., Johnson, K. I., Madan, Y., Li, S., Cai, G., Brahmbhatt, I., Borges, W. and Hsiao, B. S. 2022. Plant-derived carboxycellulose: Highly efficient bionanomaterials for removal of toxic lead from contaminated water. In: Ahuja, S. ed. *Separation ccience and technology*. Academic Press, 87-95. Available: https://www.sciencedirect.com/science/article/pii/B9780323907637000044 (Accessed

Shepa, J., Šišoláková, I., Vojtko, M., Trnková, L., Nagy, G., Maskaľová, I., Oriňak, A. and Oriňaková, R. 2021. NiO Nanoparticles for Electrochemical Insulin Detection. *Sensors*, 21 (15): 1-12.

Shirzadi-Ahodashti, M., Mizwari, Z. M., Mohammadi-Aghdam, S., Ahmadi, S., Ebrahimzadeh, M. A. and Mortazavi-Derazkola, S. 2023. Optimization and evaluation of anticancer, antifungal, catalytic, and antibacterial activities: biosynthesis of spherical-shaped gold nanoparticles using Pistacia vera hull extract (AuNPs@ PV). *Arabian Journal of Chemistry*, 16 (1): 104423.

Shojaei, T. R., Soltani, S. and Derakhshani, M. 2022. Synthesis, properties, and biomedical applications of inorganic Bionanomaterials. In: Barhoum, A., Jeevanandam, J. and Danquah, M. K. eds. *Fundamentals of Bionanomaterials*. Elsevier, 139-174.

Shrikrishna, N. S., Sharma, R., Sahoo, J., Kaushik, A. and Gandhi, S. 2024. Navigating the landscape of optical biosensors. *Chemical Engineering Journal*, 490: 151661.

Singh, A., Singh, K., Kaur, K., Sharma, A., Mohana, P., Prajapati, J., Kaur, U., Goswami, D., Arora, S., Chadha, R. and Bedi, P. M. S. 2024. Discovery of triazole tethered thymol/carvacrol-coumarin hybrids as new class of α-glucosidase inhibitors with potent in vivo antihyperglycemic activities. *European Journal of Medicinal Chemistry*, 263: 115948.

Singh, A. K. 2022. A review on plant extract-based route for synthesis of cobalt nanoparticles: Photocatalytic, electrochemical sensing and antibacterial applications. *Current Research in Green and Sustainable Chemistry*: 100270.

Singh, A. K., Jaiswal, N., Tiwari, I., Ahmad, M. and Silva, S. R. P. 2023. Electrochemical biosensors based on in situ grown carbon nanotubes on gold microelectrode array fabricated on glass substrate for glucose determination. *Microchimica Acta*, 190 (2): 55.

Singh, M. K., Pal, S., Verma, A., Das, R. and Prajapati, Y. K. 2021. A nanolayered structure for sensitive detection of hemoglobin concentration using surface plasmon resonance. *Applied Physics A*, 127: 1-10.

Šišoláková, I., Gorejová, R., Chovancová, F., Shepa, J., Ngwabebhoh, F. A., Fedorková, A. S., Sáha, P. and Oriňaková, R. 2023. Polymer-based electrochemical sensor: Fast, accurate, and simple insulin diagnostics tool. *Electrocatalysis*, 14 (5): 697-707.

Šišoláková, I., Hovancová, J., Oriňaková, R., Oriňak, A., Trnková, L., Třísková, I., Farka, Z., Pastucha, M. and Radoňák, J. 2020. Electrochemical determination of insulin at CuNPs/chitosan-MWCNTs and CoNPs/chitosan-MWCNTs modified screen printed carbon electrodes. *Journal of Electroanalytical Chemistry*, 860 (113881): 1-9.

Sitio, R. and Akmal, M. 2024. Phytochemical screening of ethanolic extract of local Aceh lime (Citrus aurantifolia (Christm.) Swingle) peels. In: Proceedings of *IOP Conference Series: Earth and Environmental Science*. IOP Publishing, 012080.

Solomons, G. T. W., Fryhle, C. B. and Snyder, S. A. 2016. *Organic Chemistry, 12th Edition*. Wiley.

Solomons, T. G. and Fryhle, C. B. 2012. *Organic Chemistry 11e Binder Ready Version+ WileyPLUS Registration Card*. John Wiley & Sons.

Song, J., Zhang, B., Li, M. and Zhang, J. 2023. The current scenario of naturally occurring indole alkaloids with anticancer potential. *Fitoterapia*, 165: 105430.

Steiner, B., Leitner, C., Stadler, D., Prugger, E.-M., Magnes, C. and Herzog, P. L. 2024. Enzymatic detection of α-hydroxybutyrate, an important marker of insulin resistance, and comparison with LC-MS/MS detection. *Practical Laboratory Medicine*, 40: e00398.

Sun, J., Mu, J., Wang, S., Jia, C., Li, D., Hua, H. and Cao, H. 2022. Design and synthesis of chromone-nitrogen mustard derivatives and evaluation of anti-breast cancer activity. *Journal of Enzyme Inhibition and Medicinal Chemistry*, 37 (1): 437-450.

Tajik, S., Beitollahi, H. and Torkzadeh-Mahani, M. 2022. Electrochemical immunosensor for the detection of anti-thyroid peroxidase antibody by gold nanoparticles and ionic liquid-modified carbon paste electrode. *Journal of Nanostructure in Chemistry*, 12 (4): 581-588.

Tavakkoli, H., Akhond, M., Ghorbankhani, G. A. and Absalan, G. 2020. Electrochemical sensing of hydrogen peroxide using a glassy carbon electrode modified with multiwalled carbon nanotubes and zein nanoparticle composites: application to HepG2 cancer cell detection. *Microchimica Acta*, 187: 1-12.

Thapa, M. and Heo, Y. S. 2023. Label-free electrochemical detection of glucose and glycated hemoglobin (HbA1c). *Biosensors and Bioelectronics*, 221: 114907.

Thapa, S., Poudel, K., Limbu, S. K., Dahal, G. and Pokhrel, S. 2022. Phytochemical screening, GC analysis and antibacterial activity of Citrus limon peel extract and essential oil. *Journal of Nepal Chemical Society*, 43 (1): 69-75.

Theakstone, A. G., Rinaldi, C., Butler, H. J., Cameron, J. M., Confield, L. R., Rutherford, S. H., Sala, A., Sangamnerkar, S. and Baker, M. J. 2021. Fourier-transform infrared spectroscopy of biofluids: A practical approach. *Translational Biophotonics*, 3 (2): e202000025.

Tshireletso, P., Ateba, C. N. and Fayemi, O. E. 2021. Spectroscopic and antibacterial properties of CuONPs from orange, lemon and tangerine peel extracts: Potential for combating bacterial resistance. *Molecules*, 26 (3): 1-12.

Ullah, A., Aleem, U., Shaheen Siddiqui, B., Haider, S., Khan, M., Anjum, S., Jahan, H., Rigano, D., Choudhary, M. I. and Ul-Haq, Z. 2023. Synthesis of New Indole-Based Thiazole Derivatives as Potential Antiglycation and Anti α-Glucosidase Agents: In Vitro and In Silico Studies. *ChemistrySelect*, 8 (47): e202301884.

Vargas, E., Nandhakumar, P., Ding, S., Saha, T. and Wang, J. 2023. Insulin detection in diabetes mellitus: challenges and new prospects. *Nature Reviews Endocrinology*, 19 (8): 487-495.

Vargas, E., Povedano, E., Krishnan, S., Teymourian, H., Tehrani, F., Campuzano, S., Dassau, E. and Wang, J. 2020. Simultaneous cortisol/insulin microchip detection using dual enzyme tagging. *Biosensors and Bioelectronics*, 167 (112512): 1-9.

Vasiljevic, J., Torkko, J. M., Knoch, K. P. and Solimena, M. 2020. The making of insulin in health and disease. *Diabetologia*, 63 (10): 1981-1989.

Venugopalan, P. and Vidya, N. 2023. Microwave-assisted green synthesis of carbon dots derived from wild lemon (Citrus pennivesiculata) leaves as a fluorescent probe for tetracycline sensing in water. *Spectrochimica Acta Part A: Molecular and Biomolecular Spectroscopy*, 286: 122024.

Verma, D., Gulati, N., Kaul, S., Mukherjee, S. and Nagaich, U. 2018. Protein based nanostructures for drug delivery. *Journal of Pharmaceutics*, 2018

Verma, S., Gupta, A. and Singh, S. 2021. Observation of Phytochemicals, Total Phenolic, Total Flavonoid and DPPH content assay Lemon (Citrus) Peel for Importance in medicinal uses. *Annals of the Romanian Society for Cell Biology*, 25 (4): 4812-4821.

Vinayagam, R., Hebbar, A., Kumar, P. S., Rangasamy, G., Varadavenkatesan, T., Murugesan, G., Srivastava, S., Goveas, L. C., Kumar, N. M. and Selvaraj, R. 2023. Green synthesized cobalt oxide nanoparticles with photocatalytic activity towards dye removal. *Environmental Research*, 216: 114766.

Walther, T. 2024. Recent improvements in quantification of energy-dispersive X-ray spectra and maps in electron microscopy of semiconductors. *Applied Research*, 3 (6): e202300128.

Wang, H.-W., Bringans, C., Hickey, A. J., Windsor, J. A., Kilmartin, P. A. and Phillips, A. R. 2021a. Cyclic voltammetry in biological samples: a systematic review of methods and techniques applicable to clinical settings. *Signals*, 2 (1): 138-158.

Wang, J., Liu, C. and Hua, J. 2021. Au-Ag nanoparticles-graphene quantum dots as sensor for highly sensitive electrochemical determination of insulin level in pharmaceutical samples. *International Journal of Electrochemical Science*, 16 (211016): 1-12.

Wang, J., Zhao, J., Liu, Y., Meng, Z., Han, X., Xu, B., Liu, R., He, C., Cheng, Z. and Zhao, B. 2023a. SERS-based detection of early Type 1 diabetes mellitus biomarkers: glutamate decarboxylase antibody and insulin autoantibody. *Sensors and Actuators B: Chemical*: 133456.

Wang, L., Xiong, Q., Xiao, F. and Duan, H. 2017. 2D nanomaterials based electrochemical biosensors for cancer diagnosis. *Biosensors and Bioelectronics*, 89: 136-151.

Wang, R. and Wang, Y. 2021. Fourier transform infrared spectroscopy in oral cancer diagnosis. *International Journal of Molecular Sciences*, 22 (3): 1206.

Wang, X., Zhu, B., Dong, J., Tian, H., Liu, Y., Song, H. and Wang, Q. 2021b. Visible-light-mediated multicomponent reaction for secondary amine synthesis. *Chemical Communications*, 57 (41): 5028-5031.

Wang, Y., Hu, Y., Wang, R., Zhang, W., Mao, H., Yuan, C. and Hua, R. 2023b. Designing stimuli-responsive upconversion nanoparticles based on a mimetic immunoassay for potential accurate diabetic nephropathy diagnosis. *Analyst*, 148 (22): 5684-5690.

Wang, Z., Fei, Y., Tang, C., Cui, L., Shen, J., Yin, K., Lu, S. and Li, J. 2021c. Diastereoselective Synthesis of Tetracyclic Tetrahydroquinoline Derivative Enabled by Multicomponent Reaction of Isocyanide, Allenoate, and 2-Aminochalcone. *Organic Letters*, 23 (11): 4094-4098.

Wardani, N. I., Kangkamano, T., Wannapob, R., Kanatharana, P., Thavarungkul, P. and Limbut, W. 2023. Electrochemical sensor based on molecularly imprinted polymer cryogel and multiwalled carbon nanotubes for direct insulin detection. *Talanta*, 254: 124137.

Yamada, H., Yoshii, K., Asahi, M., Chiku, M. and Kitazumi, Y. 2022. Cyclic voltammetry part 1: fundamentals. *Electrochemistry*, 90 (10): 102005-102005.

Yameny, A. A. 2024. Diabetes Mellitus Overview 2024. *Journal of Bioscience and Applied Research*, 10 (3): 641-645.

Yao, L., He, L., Yang, Y., Zhang, Y., Liu, Z., Liang, L. and Piao, Y. 2021. Nanobiochar paper based electrochemical immunosensor for fast and ultrasensitive detection of microcystin-LR. *Science of The Total Environment*, 750 (141692): 1-9.

Yuan, F., Li, Y., Wang, Y., Li, Z., Wang, Q., Sun, H., Zhang, D., Wang, W. and Wang, B. 2023. Cobalt nanoparticles synergize with oxygen-containing functional groups to realize fast and stable potassium storage for carbon anode. *Advanced Functional Materials*, 33 (46): 2304753.

Zaib, M., Shahzadi, T., Muzammal, I. and Farooq, U. 2020. Catharanthus roseus extract mediated synthesis of cobalt nanoparticles: evaluation of antioxidant, antibacterial, hemolytic and catalytic activities. *Inorganic and Nano-Metal Chemistry*, 50 (11): 1171-1180.

Zaki, R. M., Wani, M. Y., Mohammed, A. and El-Said, W. A. 2023. Design, synthesis and evaluation of novel Se-alkylated pyrazoles and their cyclized analogs as potential anticancer agents. *Journal of Molecular Structure*, 1276: 134670.

Zamani, A., Marjani, A. P. and Mousavi, Z. 2019. Agricultural waste biomass-assisted nanostructures: synthesis and application. *Green Processing and Synthesis*, 8 (1): 421-429.

Zhang, D., Bai, Y., Niu, H., Chen, L., Xiao, J., Guo, Q. and Jia, P. 2024. Enzyme Immobilization by Inkjet Printing on Reagentless Biosensors for Electrochemical Phosphate Detection. *Biosensors*, 14 (4): 168.

Zhang, M., Liu, Y., Li, D., Cui, X., Wang, L., Li, L. and Wang, K. 2023a. Electrochemical impedance spectroscopy: A new chapter in the fast and accurate estimation of the state of health for lithium-ion batteries. *Energies*, 16 (4): 1599.

Zhang, W., Chen, Y.-P., Zhang, L., Feng, J.-J., Li, X.-S. and Wang, A.-J. 2022. Theophylline-regulated pyrolysis synthesis of nitrogen-doped carbon nanotubes with iron-cobalt nanoparticles for greatly boosting oxygen reduction reaction. *Journal of Colloid and Interface Science*, 626: 653-661.

Zhang, X., Cheng, B., Li, H., He, Y., Xu, W., Duan, X., Sun, H., Wang, T. and Zhai, H. 2021. Synthesis of Hydrobenzoimidazoles from para-Quinamines and 1, 3, 5-Triazinanes via a Formal [3+ 2] Annulation Reaction. *Advanced Synthesis & Catalysis*, 363 (2): 565-569.

Zhang, Y., Wu, C., Zhang, N., Fan, R., Ye, Y. and Xu, J. 2023b. Recent advances in the development of pyrazole derivatives as anticancer agents. *International Journal of Molecular Sciences*, 24 (16): 12724.

Zhao, H., Du, X., Dong, H., Jin, D., Tang, F., Liu, Q., Wang, P., Chen, L., Zhao, P. and Li, Y. 2021a. Electrochemical immunosensor based on Au/Co-BDC/MoS_2 and DPCN/MoS_2 for the detection of cardiac troponin I. *Biosensors and Bioelectronics*, 175 (112883): 1-8.

Zhao, P., El-kott, A., Ahmed, A. E., Khames, A. and Zein, M. A. 2021b. Green synthesis of gold nanoparticles (Au NPs) using Tribulus terrestris extract: Investigation of its catalytic activity in the oxidation of sulfides to sulfoxides and study of its anti-acute leukemia activity. *Inorganic Chemistry Communications*, 131: 108781.

Zhou, L., Zhu, R., Figueroa-Miranda, G., Neis, M., Offenhäusser, A. and Mayer, D. 2024. Ratiometric electrochemical aptasensor with strand displacement for insulin detection in blood samples. *Analytica Chimica Acta*, 1317: 342823.

Zhou, X., Lai, W., Zhong, J., Yang, Y., Chen, Z. and Zhang, C. 2023. Point-of-care detection of glycated hemoglobin using a novel dry chemistry-based electrochemiluminescence device. *Analytica Chimica Acta*, 1279: 341829.

Zhu, Y., Zhao, J., Luo, L., Gao, Y., Bao, H., Li, P. and Zhang, H. 2021. Research progress of indole compounds with potential antidiabetic activity. *European Journal of Medicinal Chemistry*, 223: 113665.

Appendix 1: Plausible mechanism for synthesis of compound 4b via 3 + 2 annulation reaction.

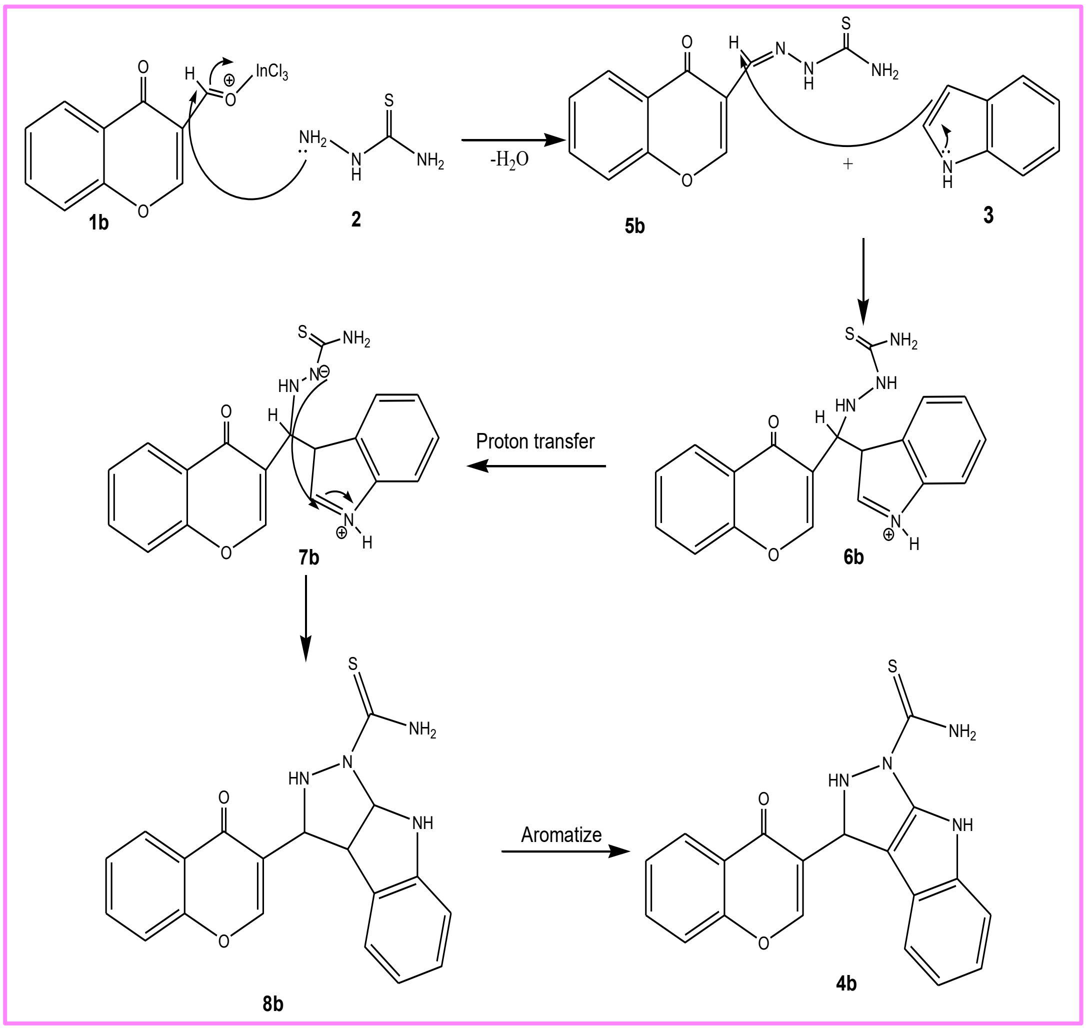

Appendix 2: ^{1}H NMR spectrum of Bis-indole-pyrazole 4a

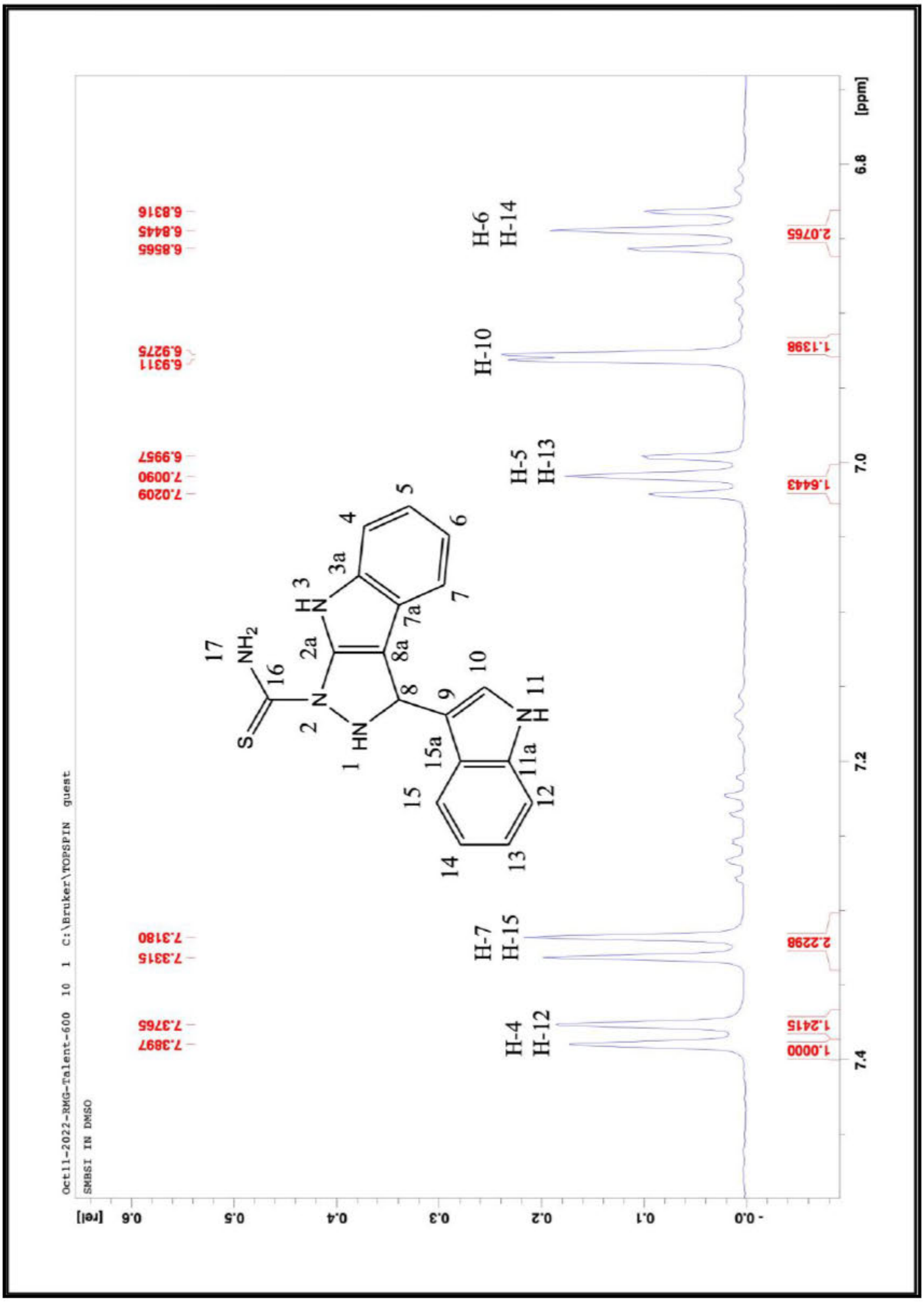

Appendix 3: APT spectrum of Bis-indole-pyrazole 4a

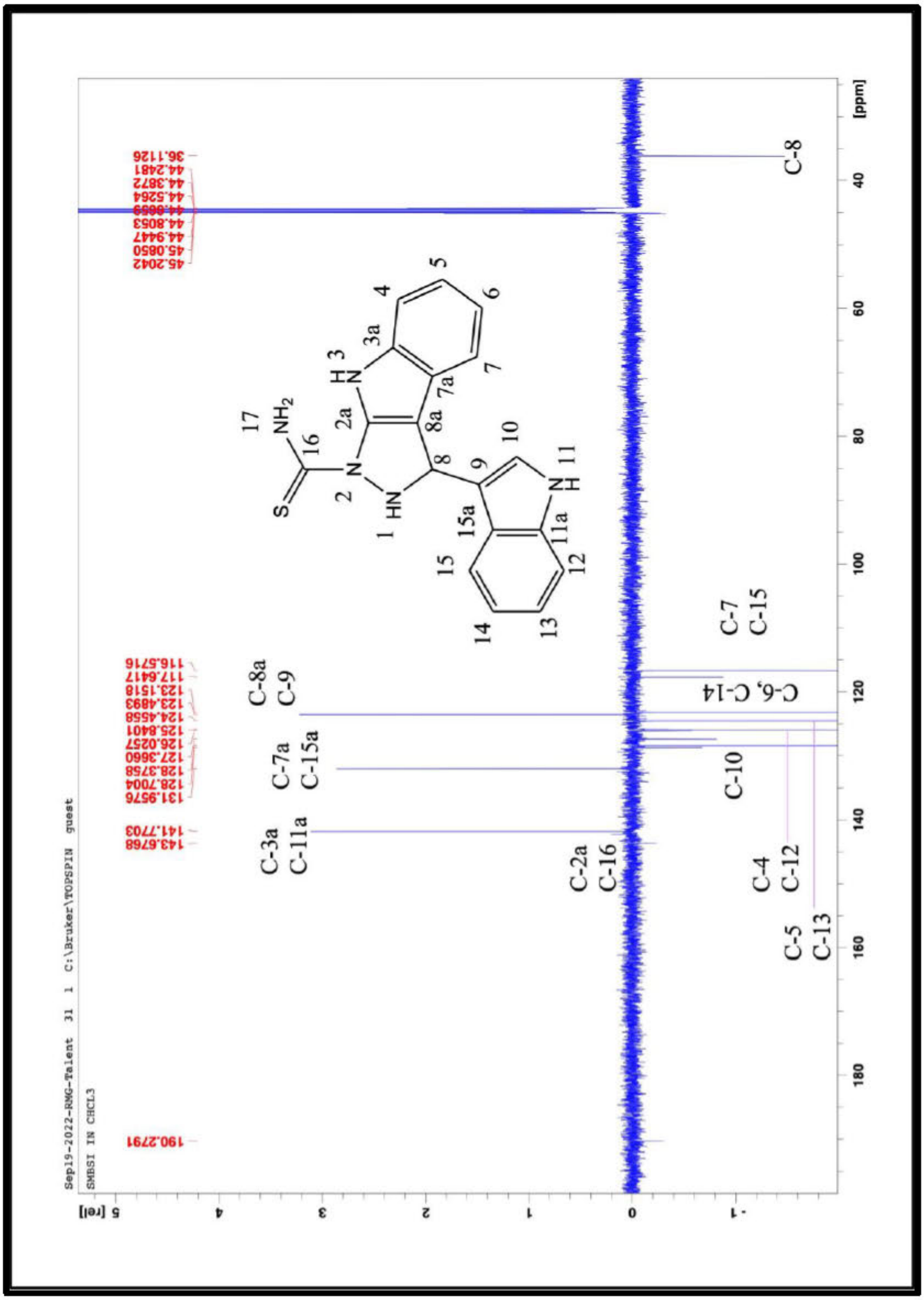

Appendix 4: H,H-COSY spectrum of Bis-indole-pyrazole 4a

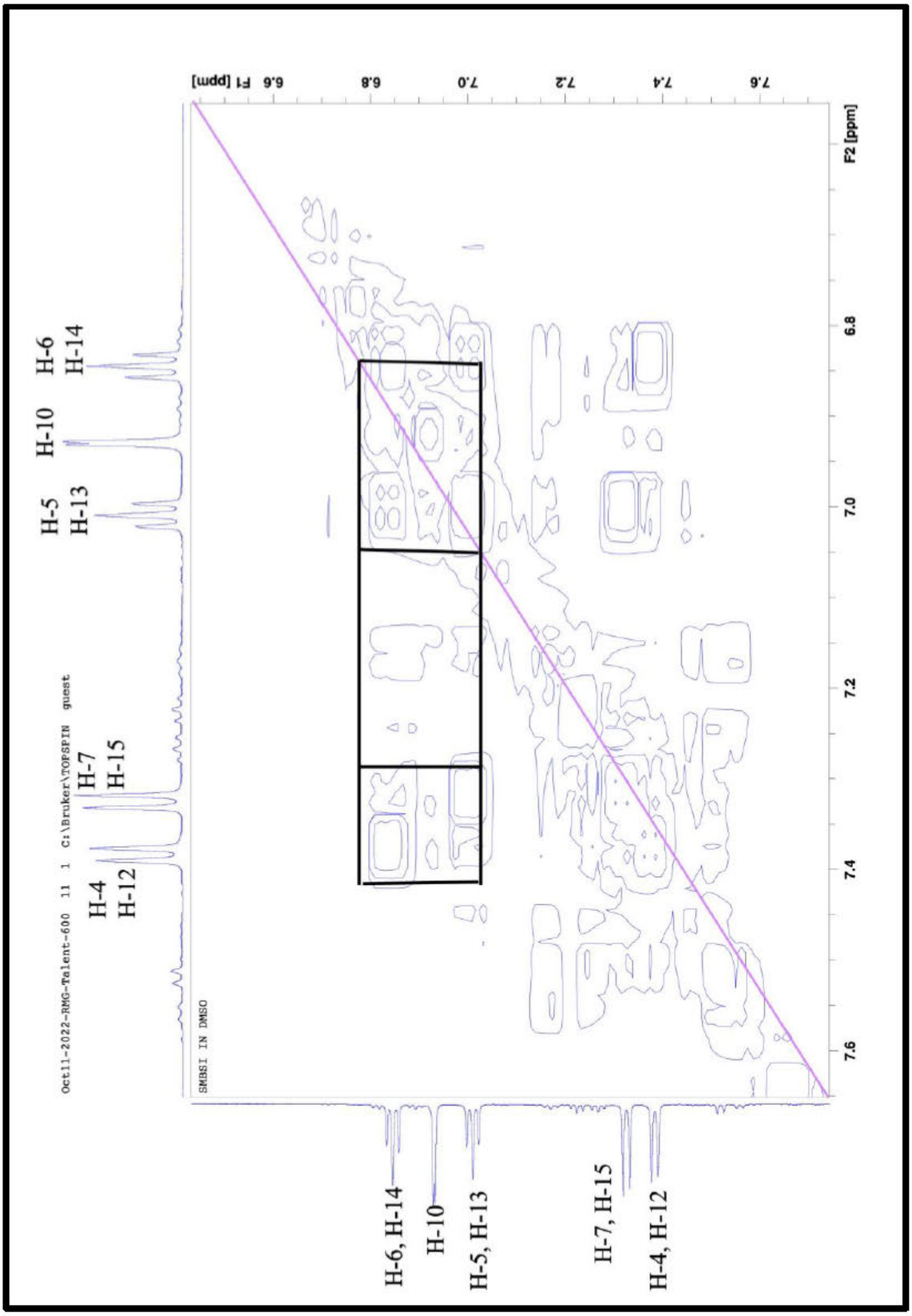

Appendix 5: HSQC spectrum of Bis-indole-pyrazole 4a

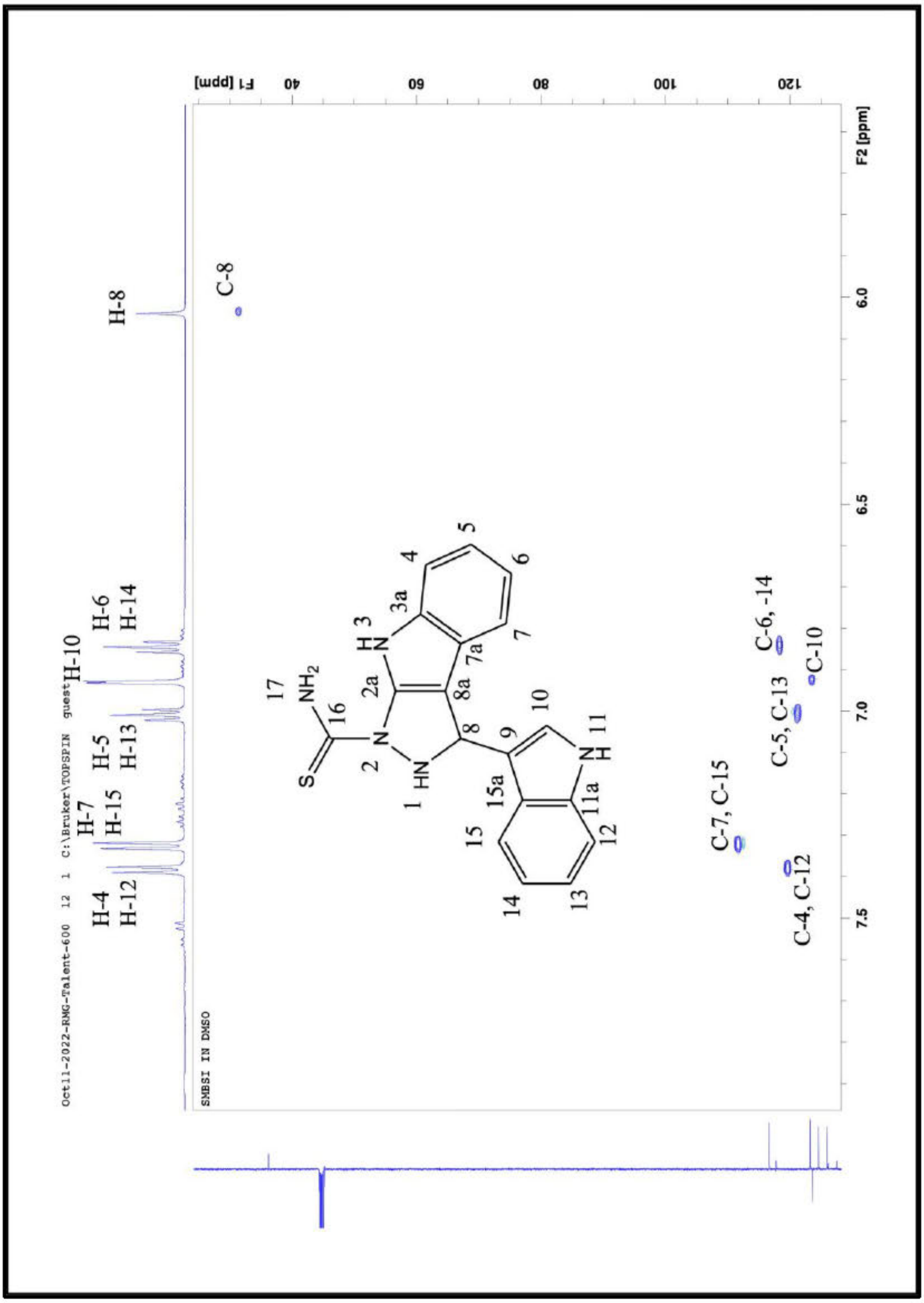

Appendix 6: HMBC spectrum of Bis-indole-pyrazole 4a

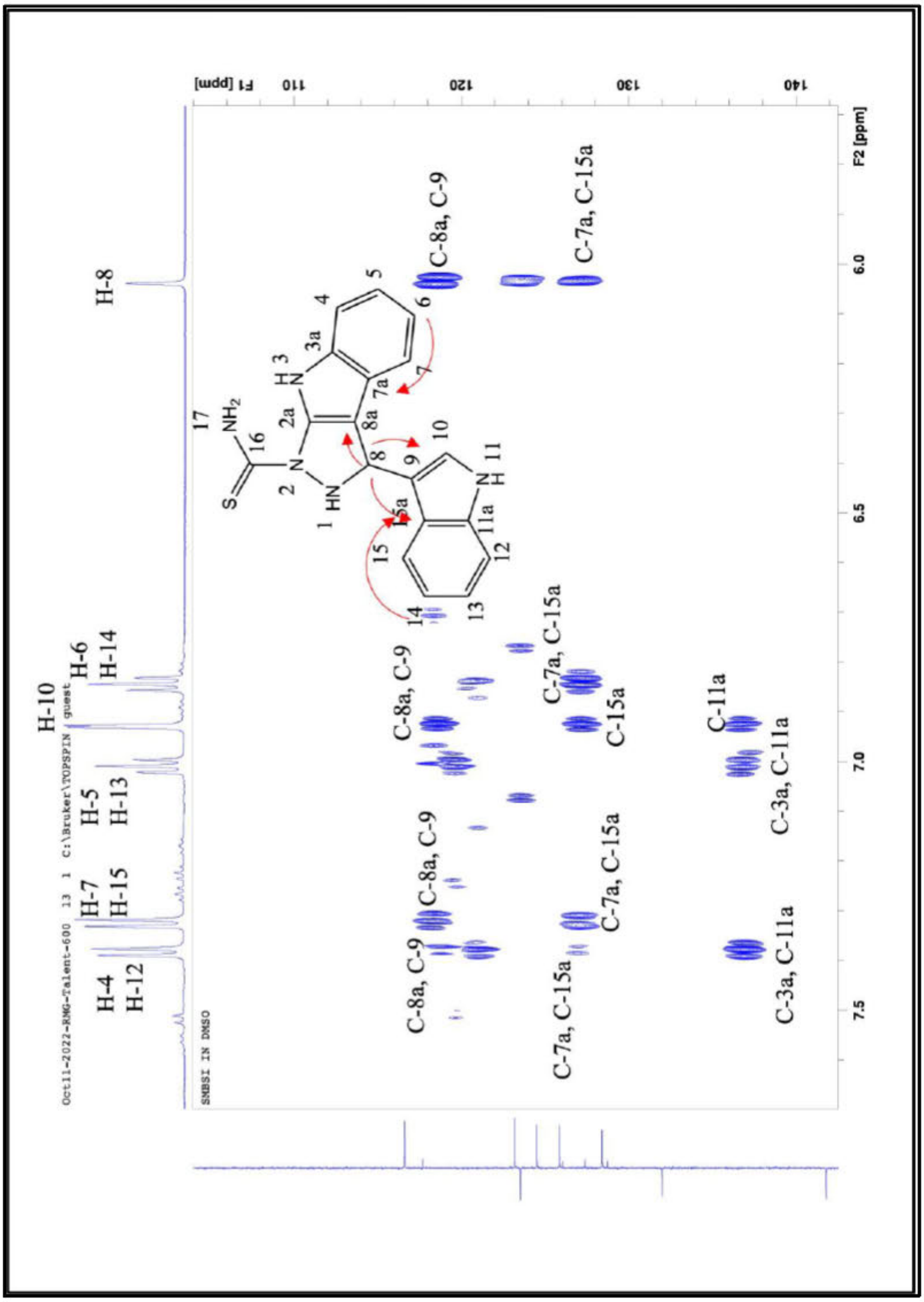

Appendix 7: TOF-MS spectrum of Bis-indole-pyrazole 4a

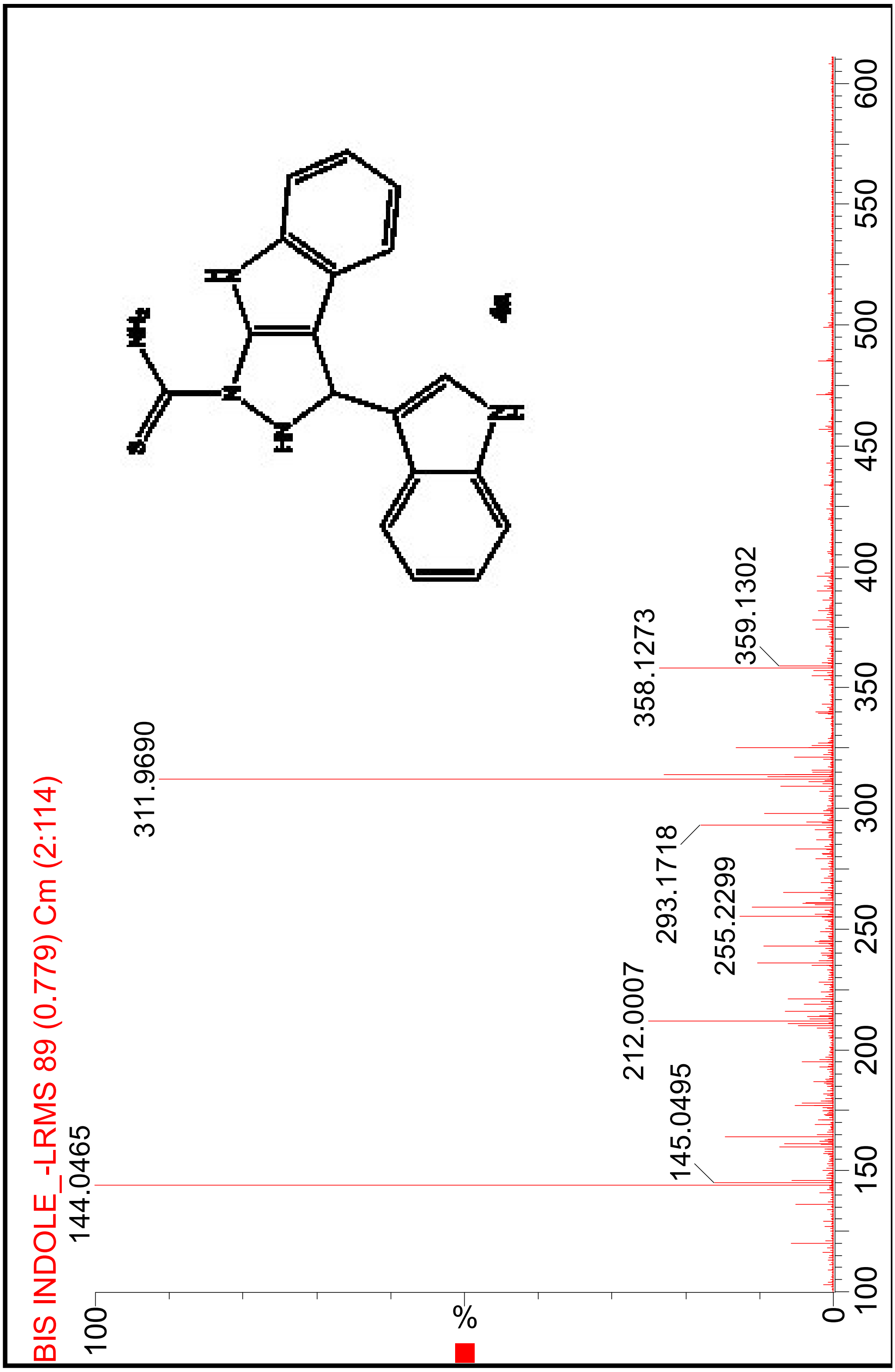

Appendix 8: ¹H NMR spectrum of Chromone indole-pyrazole 4b

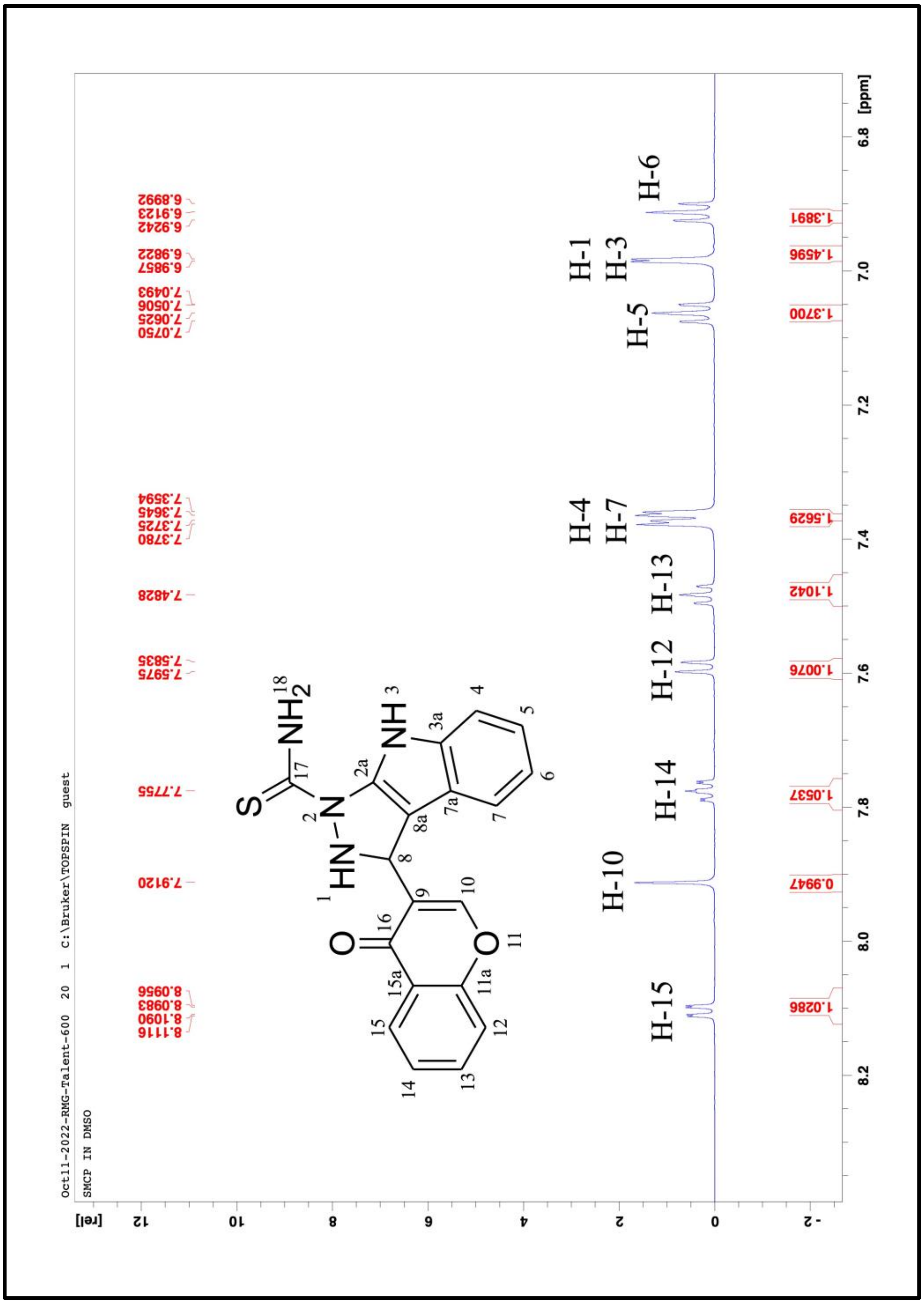

Appendix 9: APT spectrum of Chromone indole-pyrazole 4b.

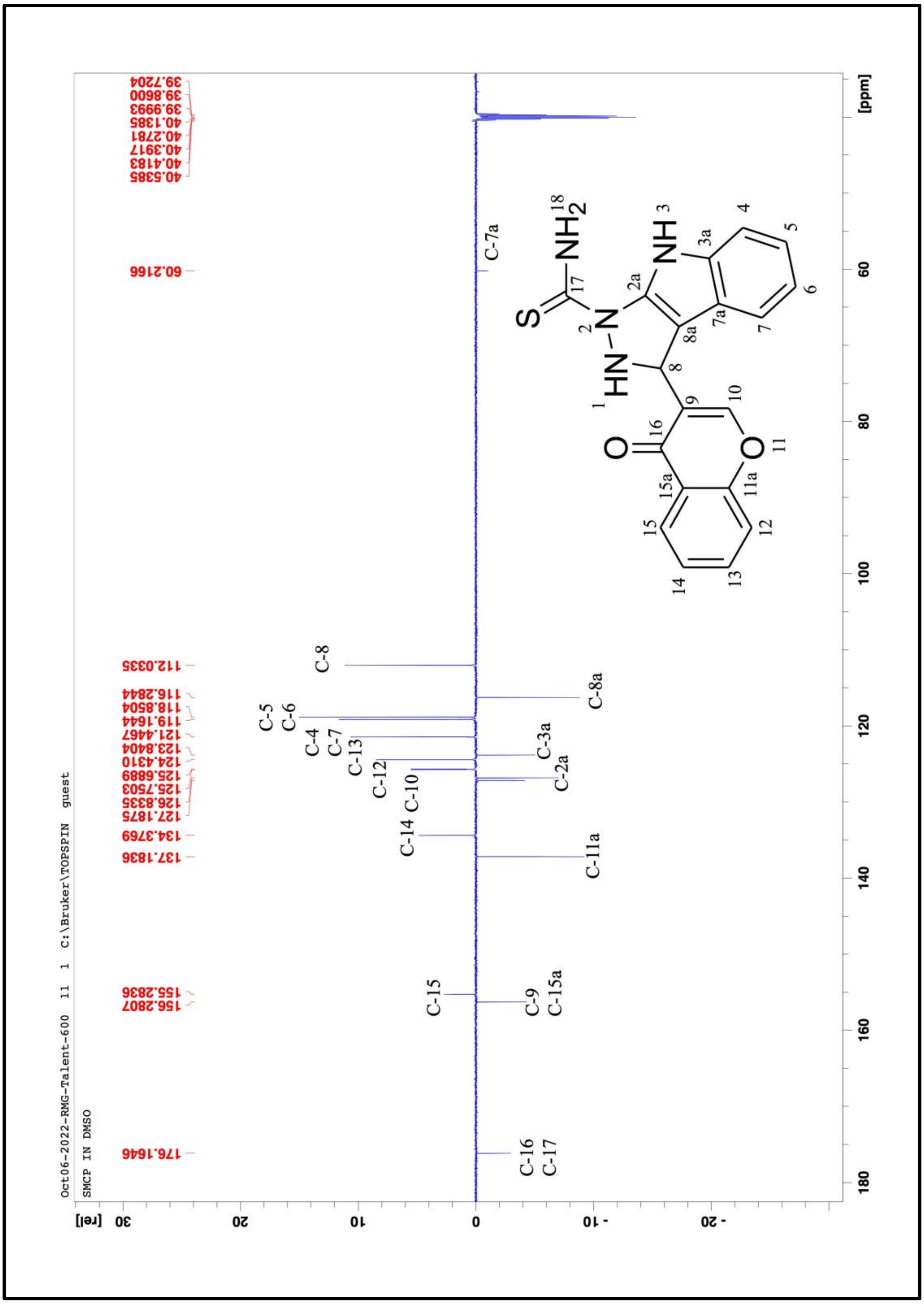

Appendix 10: H,H:COSY spectrum of Chromone indole-pyrazole 4b.

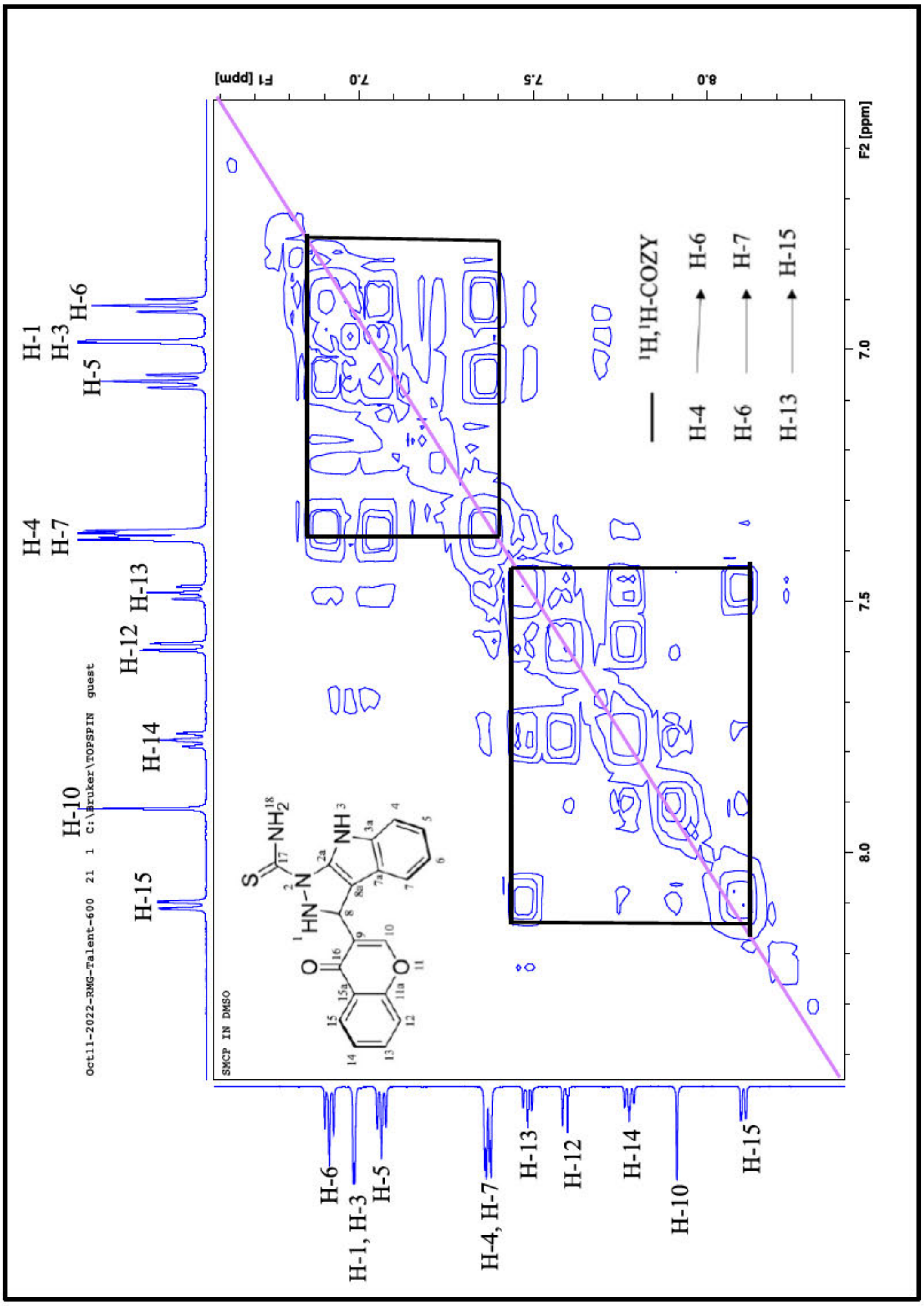

Appendix 11: HSQC spectrum of Chromone indole-pyrazole 4b.

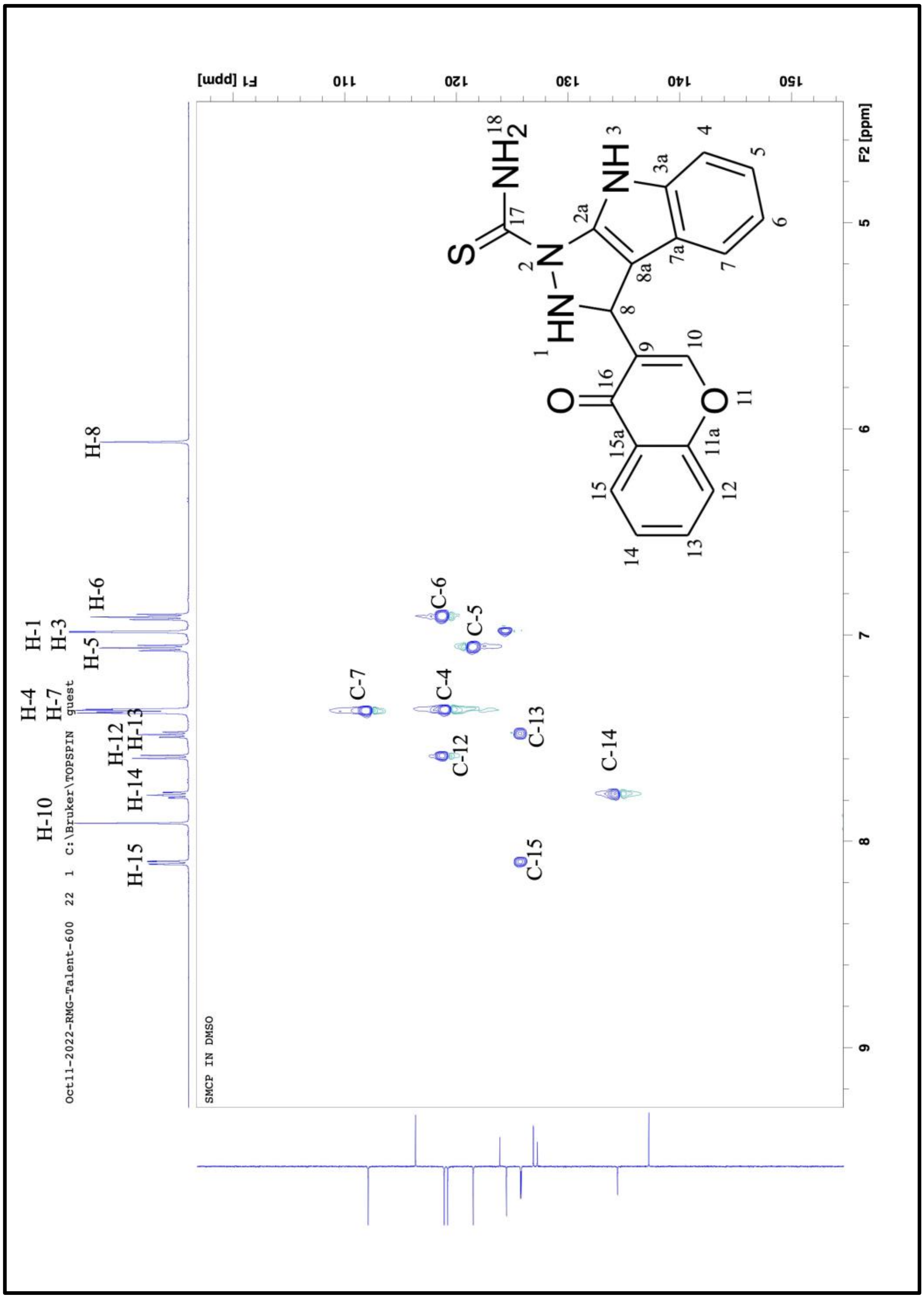

Appendix 12: HMBC spectrum of Chromone indole-pyrazole 4b.

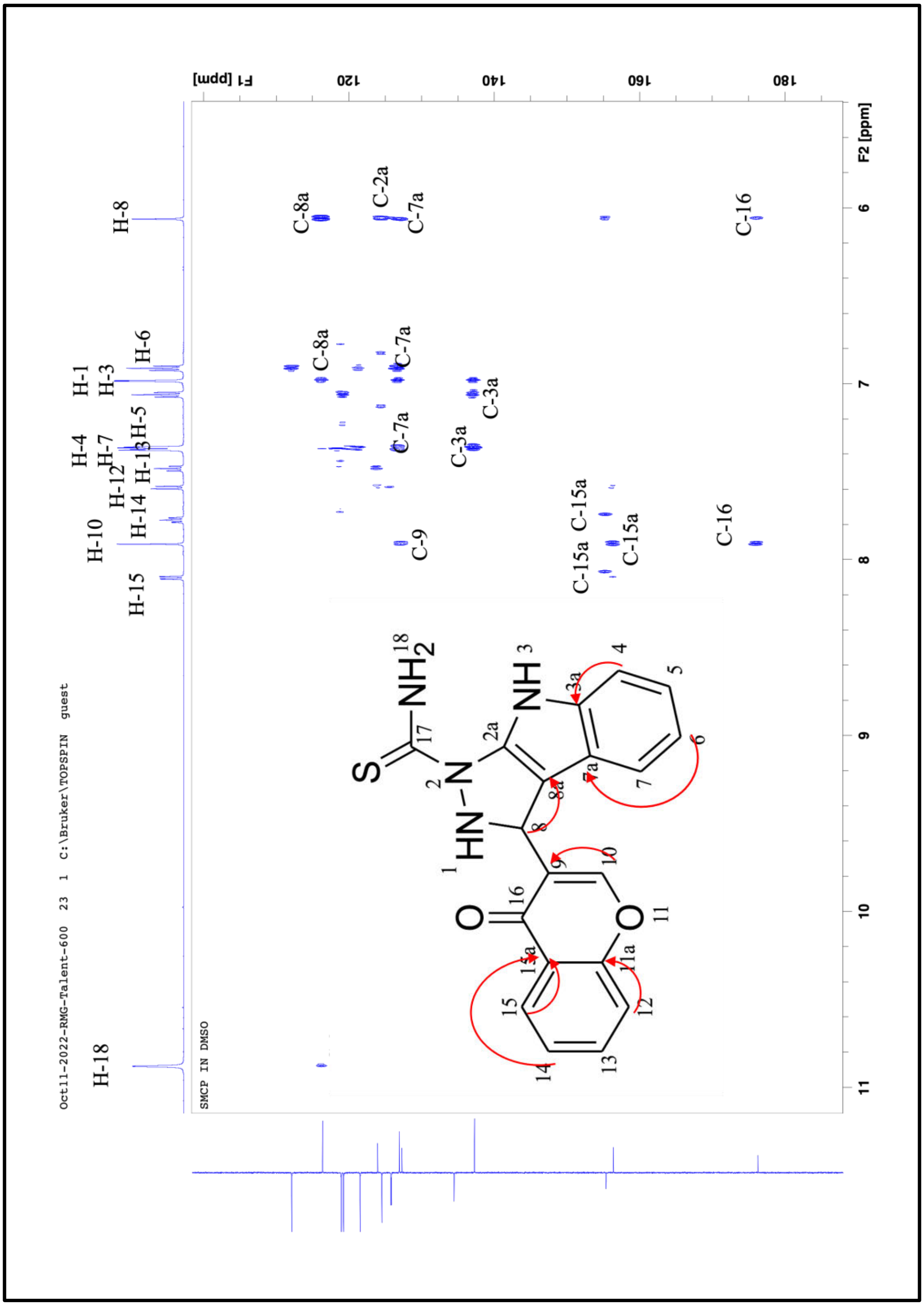

Appendix 13: TOF-MS spectrum of Chromone indole-pyrazole 4b

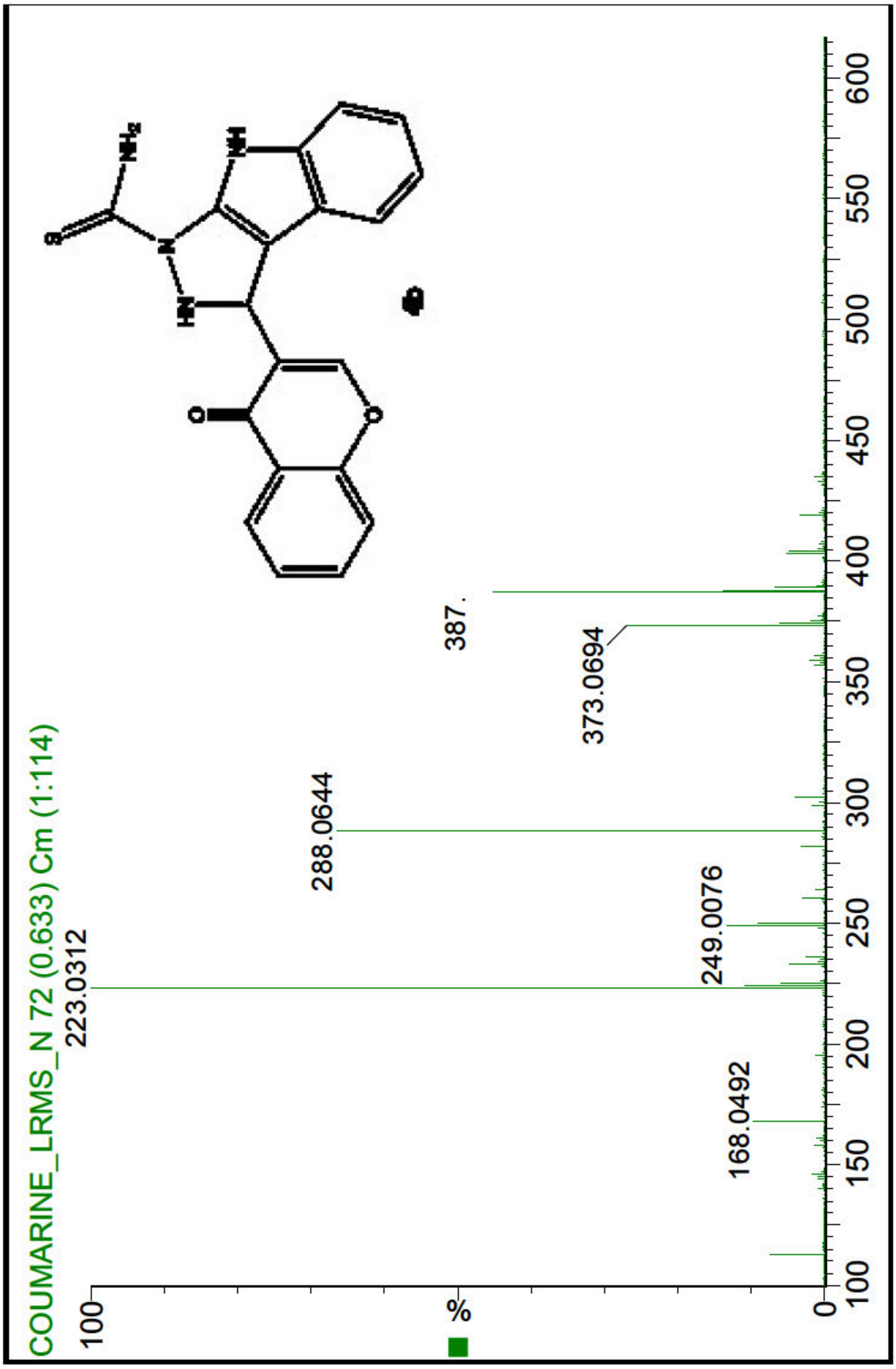

Appendix 14: Electrochemical characterization of BIP-CoNPs immunosensor

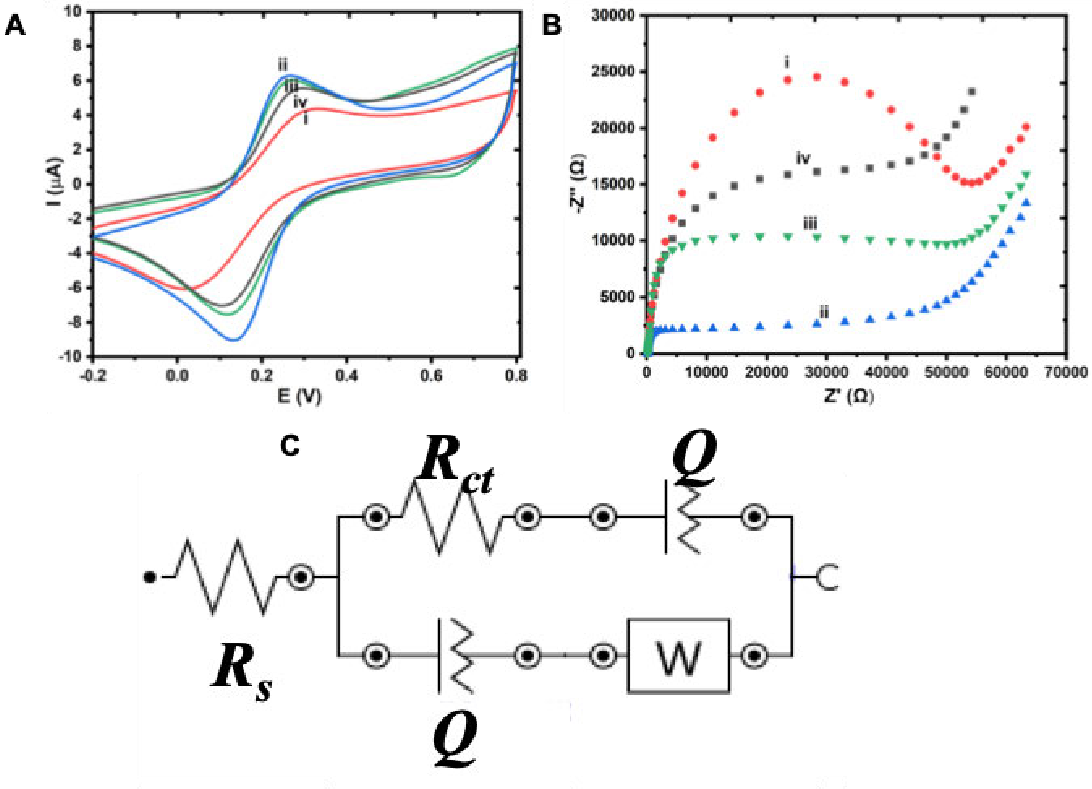

(**A**) Cyclic voltammograms and (**B**) Nyquist plots obtained for bare and modified electrodes in 5 mM [Fe (CN)$_6$]$^{-3/-4}$ solution prepared in 0.1 M phosphate buffer. (i) Bare PtE, (ii) BIP-CoNPs/PtE, (iii) Anti/BIP-CoNPs/PtE and BSA/Anti/BIP-CoNPs/PtE. (**C**) Equivalent circuits used in fitting EIS data for the bare and modified electrodes for BSA/anti/BIP-CoNPs/PtE.

Appendix 15: Electrochemical characterisation of BIP-CoNPs immunosensor.

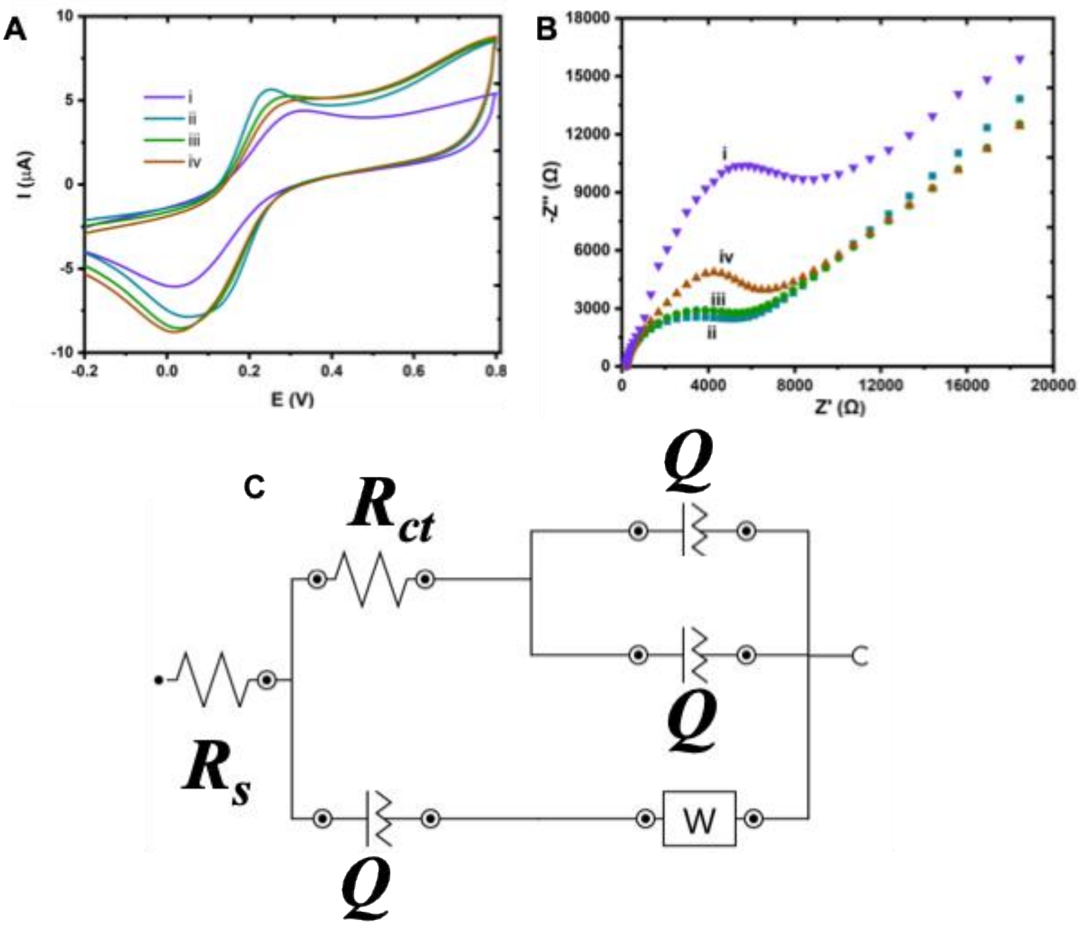

(**A**) Cyclic voltammograms and (**B**) Nyquist plots obtained for bare and modified electrodes in 5 mM $[Fe\ (CN)_6]^{-3/-4}$ solution prepared in 0.1 M phosphate buffer. (i) Bare PtE, (ii) BIP-AuNPs/PtE, (iii) Anti/BIP-AuNPs/PtE and BSA/Anti/Au-CoNPs/PtE. (**C**) Equivalent circuits used in fitting EIS data for the bare and modified electrodes for BSA/anti/CIP-AuNPs/PtE

Appendix 16: TEM images Used for Particle Size Distribution Analysis

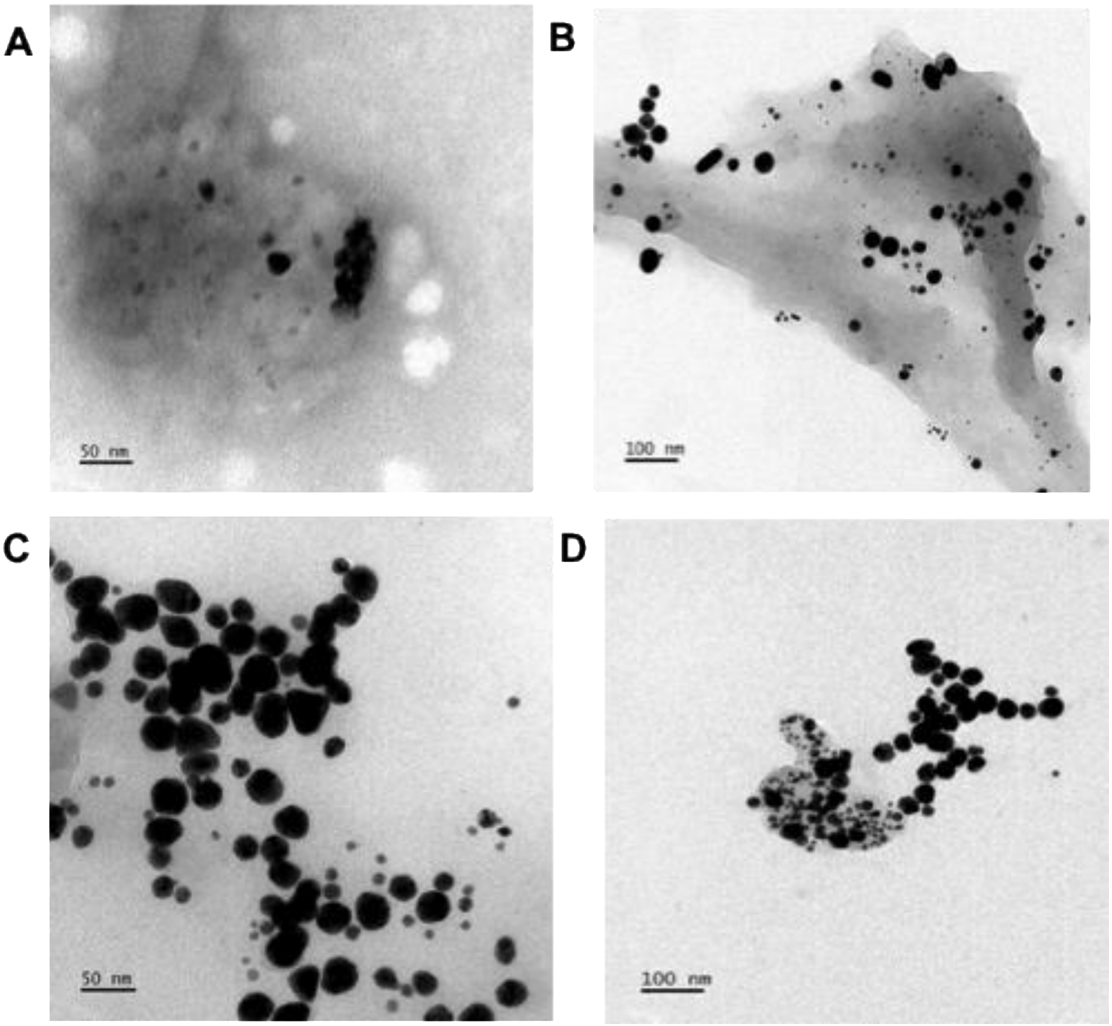

TEM images of the synthesised indole-pyrazole capped nanoparticles(**A**) BIP-CoNPs , (**B**) CIP-CoNPs (**C**) BIP-AuNPs and (**D**) CIP-AuNPs